

ARISTOTLE UNIVERSITY OF THESSALONIKI  
SCHOOL OF NATURAL SCIENCE - PHYSICS DEPARTMENT  
SECTION OF ASTRONOMY, ASTROPHYSICS AND MECHANICS

**Photometric observations and Data Reduction  
of Contact Binary Systems and of SS433  
Long Term Study of the Astronomical Seeing  
in Mount Xolomon Chalkidikis.**

Diploma Thesis  
By John S. Nestoras

Supervisors:  
John H. Seiradakis, Stayros I. Avgoloupis  
2007

*To Those who Seek the Unknown Truth . . .*

## Abstract

My Diploma thesis is divided into three different parts. The first one is the measurement of the true astronomical seeing in mount Xolomon. The work is based on a variation of the method that M.Sarazin proposed (ESO-DIMM), the H-DIMM. This method does not require the existence of a prism for the diversion of light but just a Hartmann mask (a mask with two holes) and an out of focus telescope. The measurement is done by measuring the relevant error in the CCD chip of the two images that was created by the out of focus telescope. Using this relevant error with the known equations from the DIMM theory, we can easily extract the seeing value. The seeing was measured for more than one year and the result was a median value of 0.82 arcsec. An excellent value if we take in mind the low altitude of the area the measurements took place (900m). Also a correlation with weather data was done to see how winds affect seeing. Based on these observations and within the diploma thesis, a new dedicated DIMM monitor was developed for the astronomy lab of the Aristotle University of Thessaloniki. New software was developed using Starlink routines and C-shell programming.

The second part is dedicated to the study of close binary systems. A new method of analysis of their O-C diagrams, proposed by T.Kalimeris, was applied to data collected for the system ER-Ori. This new method applies non-linear fitting to the O-C curve and extracts the  $P(E)$  function. The  $P(E)$  function is the orbital period vs. orbital cycle. It is very important to know this function for a binary system as it shows how the orbital period changes with time. The strongest point of the new method is the continuous character of the  $P(E)$  function. Afterwards with Fourier Transformations and wavelet analysis any trend in the  $P(E)$  function of the system is detected. This knowledge it can then be applied for the calculation of the mass transfer function or by further analysis of the residuals of the fitting process, it reveals the existence or not of a third body in the system. The method is so sensitive that even a body with the mass of earth can be detected at any star that can be photometrically observed regardless it's distance.

The third and final part is the study of behaviour in optical wavelengths of the prototype microquasar SS433. Differential photometry was done with the 1.2m telescope of NOA in V and R filters in 2004 and 2005 for a total of sixteen clear nights. The main goal of the research was to find any periodicities in the light curves that are longer than 30sec. This was done by means of Fourier and Wavelet analysis to the data. From the resulting periodograms we confirmed the nutational period of the binary system and found a chaotic behaviour in time scales of hours and smaller, probably because of the accretion disk of the system.

## Preface

This diploma thesis was possible because some people helped me, not only with their technical knowledge but also with their psychological and financial help. So i feel the need to thank them here from the depths of my heart, because they opened to me a whole new world to explore and play. And i'm saying play, because what i did for this diploma thesis, was more than pleasure, it was what i was dreamed from a little child.

First i would like to thank my mother that stood up to me like nobody else, saying nothing about my crazy ideas going out in the mountains and in cold to observe. Also i would like to thank my rest of my family, that they also helped me with whatever way they could.

Of course it would be an omission if i would not thank my professors J.H. Seiradakis and S. Avgoloupis. Without them, nothing would be posible. Also a big thanks to the late E.Harlauti who had the original idea on the work in SS433. I thank him because he gave me the chance to work on a big astronomical telescope and in a real research project. It is sure that without him and my professors my CV would be awfully smaller.

Finally i must thank N.Dimou, the techician of the Kryoneri astronomical station, who help me many times with problems i encoutered at the telescope. Also i would like to thank S.Kitsiona and O.Giannaki, that with their knowledge they were crucial to my work.

# Contents

<b>I</b>	<b>O-C CURVE ANALYSIS OF CONTACT BINARIES</b>	<b>1</b>
<b>1</b>	<b>About O-C Diagrams</b>	<b>2</b>
1.1	Eclipses And Times Of Minima . . . . .	2
1.2	O-C Differences and O-C Diagrams . . . . .	3
1.3	O-C Diagram Creation And Changes Of The Orbital Period . . . . .	5
1.4	Basic Principals Of O-C Diagrams . . . . .	9
1.4.1	Non-Linear Modulation of O-C Diagrams . . . . .	9
1.4.2	Formation of O-C Diagrams from Constant and Stable Rate Changes of Period. . . . .	9
1.4.3	Observational and Photometric Noise in O-C Diagrams . . . . .	10
1.5	Photometric Noise and Apparent Period Changes . . . . .	11
1.6	O-C Diagram Formation . . . . .	13
1.6.1	O-C Differences From The Light-Time Effect . . . . .	13
<b>2</b>	<b>Analysis Methods Of O-C Diagrams</b>	<b>16</b>
2.1	The Classical Analysis Model . . . . .	16
2.2	Why The Classic Model Is Wrong? . . . . .	17
2.3	The New Kalimeris Model of O-C Analysis . . . . .	20
2.3.1	Least Squares Polynomial Description of O-C Curves . . . . .	20
2.3.2	Noise Handling with Chebyshev Polynomials in Kalimeris Model . . . . .	23
2.4	Existence of a Third Body in Binary Systems . . . . .	23
<b>3</b>	<b>Photometry - Analysis Of Observational Data</b>	<b>25</b>
3.1	ER-Ori . . . . .	26
<b>4</b>	<b>Results and Conclusions</b>	<b>31</b>
4.1	Future Work . . . . .	31

---

<b>II</b>	<b>PHOTOMETRY FOURIER AND WAVELET ANALYSIS OF SS433</b>	<b>32</b>
<b>1</b>	<b>Introduction to Microquasars and SS433</b>	<b>33</b>
1.1	The SS433 Microquasar . . . . .	34
1.2	The Kinematic Model . . . . .	35
1.3	The Jet's of SS433 Microquasar . . . . .	38
1.4	Flaring Events . . . . .	39
<b>2</b>	<b>Observations And Data Analysis of SS433</b>	<b>41</b>
2.1	High Speed Photometry of SS433 . . . . .	41
2.1.1	Analysis of Observational Data . . . . .	41
2.2	Methods of Time-series Analysis . . . . .	43
2.2.1	The Fourier Algorithm . . . . .	43
2.2.2	Noise And Real Periodicities . . . . .	45
2.2.3	The Wavelet Algorithm . . . . .	45
2.3	Thoughts in The Appropriate Method of Analysis . . . . .	46
2.3.1	Deterministic and Stochastic Signals . . . . .	46
<b>3</b>	<b>Introduction of Observational Data</b>	<b>48</b>
3.1	Light Curves of SS433 . . . . .	48
3.1.1	2004-Data . . . . .	48
3.1.2	2005-Data . . . . .	52
3.2	Fourier Analysis . . . . .	57
3.2.1	2004-Data . . . . .	57
3.2.2	2005-Data . . . . .	64
3.3	Wavelet Analysis . . . . .	74
3.3.1	2004-Data . . . . .	74
3.3.2	2005-Data . . . . .	78
3.4	Phase Diagram for the Nutational Period Of SS433 . . . . .	84
<b>4</b>	<b>Results, Conclusions And discoveries</b>	<b>85</b>
4.1	Conclusions . . . . .	85
4.2	Possible Future Research . . . . .	86
<b>III</b>	<b>ASTRONOMICAL SEEING AND DIMM</b>	<b>87</b>
<b>1</b>	<b>Atmosphere And Astronomical Observing</b>	<b>88</b>
1.1	Air Mass - Extinction . . . . .	88
1.1.1	Laplace's extinction theorem . . . . .	89

---

1.2	Atmospheric refraction . . . . .	91
<b>2</b>	<b>Theory Of Astronomical Seeing</b>	<b>93</b>
2.1	In General About Seeing and Turbulent Flows . . . . .	93
2.1.1	Kolmogorov Model And the Fried Parameter . . . . .	93
2.1.2	Temporal Behaviour of Turbulence . . . . .	95
2.1.3	Impact of Turbulence (Seeing) to an Image . . . . .	96
<b>3</b>	<b>Methods to Calculate Astronomical Seeing - The DIMM</b>	<b>98</b>
3.1	DIMM - Differential Image Motion Monitor . . . . .	99
3.1.1	ESO-DIMM . . . . .	99
3.1.2	Hartmann-DIMM . . . . .	101
3.2	Air Mass And Wavelength Dependence . . . . .	102
3.3	Exposure Time Dependence . . . . .	102
<b>4</b>	<b>Development of a New H-DIMM Unit</b>	<b>104</b>
4.1	Why a new H-DIMM Unit? . . . . .	104
4.1.1	Required Characteristics. . . . .	104
4.1.2	The Seeing-GR Project. . . . .	104
4.2	Aquisition Software Development. . . . .	105
4.2.1	The Program's Interface . . . . .	105
4.2.2	Taking Measurements . . . . .	106
4.2.3	The Output Data . . . . .	107
4.2.4	Possible Error Messages . . . . .	108
4.3	Reduction Software Development. . . . .	108
<b>5</b>	<b>Scintillation Measurements with the H-DIMM</b>	<b>109</b>
5.1	Measurement Technique . . . . .	110
5.1.1	Correcting for Zenith-Distance . . . . .	111
5.2	Estimate Of The Isoplanatic Angle Through the Scintillation Index . . . . .	112
<b>6</b>	<b>Observations And Results On Mt.Holomon</b>	<b>114</b>
6.1	Seeing, Scintillation and Isoplanatic Angle Curves . . . . .	115
6.1.1	Confirmation of the No-Correlation of Seeing and Scintillation . . . . .	146
6.2	Conclusions . . . . .	147
6.2.1	Possible Future Work . . . . .	150

# Part I

## O-C CURVE ANALYSIS OF CONTACT BINARY SYSTEMS

# Chapter 1

## About O-C Diagrams

*“Observing Closer ...”*

### 1.1 Eclipses And Times Of Minima

In every double ecliptic system the times of minimum light that are formed from the eclipses they signal the crossing of one member of the system in front of the other. This fact can be used to measure the orbital period of the system. The period of any ecliptic system is considered to be the time between two consecutively crossings of the secondary member in front of the primary, namely the time between two consecutively primary times of minimum light. The period of ecliptic systems can be found in great accuracy because the time of minimum light is well defined. Even if we have a limited number of light curves, we can found the period with an error margin of one minute, whereas we have a large amount of curves that span in a few thousand orbital cycles, we can estimate the period with an accuracy of  $10^{-6}$ sec. Of course this level of accuracy can not be achieved with a direct measurement of the orbital period but only by measuring the total number of cycles and in conjunction with polynomial fitting.

**Ephemeris of apparent minimum light.** The knowledge of the orbital period of a system permits the construction of a simple equation :

$$C_E = T_0 + P \cdot E \quad (1.1)$$

Through this equation we can predict the moment  $C_E(\text{MinI})$  that the secondary member passes in front of the primary during the random orbital cycle  $E$ . If  $E$  takes a non integer value (but always with a decemical place of the form 0.5) then equation 1.1 will predict the times of crossing of the primary in front of the secondary member ( $\text{MinII}$ ).  $T_0$  is a constant and usually is the oldest recorded moment of a primary eclipse, is measured in Heliocentric Julian Days (Hel.JD).  $P$  of course is the orbital period of the system and is measured in mean solar days. Equation 1.1 is called an

ephemeris of minimum light of the double system. For example the ephemeris equation for ER-ORI is  $\text{MinI}=2443090.53+0.4223399431E$

**Real and Photometric Times of Minimum** The accurate record of the eclipses of a double system through the times of minimum light permits as to know the moment that the apparent disks of the members are aligned to the observer here in earth. Every such moment can be used as a start of measurement of the orbital phase  $\varphi$  of the secondary star ( $0 \leq \varphi \leq 2\pi$  or  $0 \leq \varphi \leq 1$  through normalization). By definition orbital phase is 0 during the eclipse of the primary and 0.5 during the eclipse of the secondary. In systems that their orbits are circular the orbital phase  $\varphi$  coincides with the real anomaly  $v$ . In such cases we can know exactly the location in the orbit of the stars so the photometric eclipse coincide with the real one, that is when the two centers of gravity of the stars are aligned. Usually the photometric eclipse occurs in a little different moment than that of the real eclipse for a various o reasons. One of these reasons is for example when the surface temperature distribution of the members does not appear to have any symmetry with the axis or the geometrical centre of the apparent disk of some member. Even in close binary systems that the geometrical and photometric irregularities are important the difference of the real and the photometric eclipse is not great. Relative measurements show that this value is not more than 1/100 of the orbital period. So for W Uma systems this value is in the range of on minute and a few seconds.

## 1.2 O-C Differences and O-C Diagrams

In a double system that consists of spherical stars with uniform radiant surfaces that they move in circular orbits of constant orbital period, the observed times of minima  $O_E$  coincide with the computed times  $C_E$  that predicts any linear ephemeris. Namely it is  $O_E - C_E = 0$ . Of course in real world this relation does not come true but only in approximation, weather it is because at the moment of the eclipse the photometric centres of the two stellar disks are not aligned with the dynamic centres or because the orbital period has changed in the meanwhile. A direct consequence of this is the creation of non-zero differences between observed ( $O_E$ ) and calculated ( $C_E$ ) times of minimum light. These differences are called O-C differences and can be calculated immediately as soon as the  $O_E$  moments are detected in the light curves. Simultaneous observations of one system in more than one spectral range leads to the creation of multicolour O-C differences.

**O-C Diagrams** By definition O-C differences can be measured only during the integer or half-integer values of the orbital cycles  $E$ . Therefore O-C differences consist a time series. The graphs of such time series are known as O-C diagrams. Some O-C diagrams of contact binary systems are shown in figure 1.1. Because the observations of a system it is impossible to be covered in an uninterrupted way in all of the orbital cycles, it becomes clear that for every eclipsing binary system, O-C differences composite time series with random data distribution. Most O-C diagrams

cover several thousand of orbital cycles in a farraginous manner, namely hereupon a time span of a few decades to one aeon of observational data. If we think that every light curve can feed at the most two times of minimum light (one  $O_E$  for the main eclipse and one  $O_{E+0.5}$  for the secondary eclipse) we can conclude that the formation of an O-C diagram that covers a few decades is on of the most demanding and long lasting procedures of observational astronomy.

In most of the O-C diagrams and especially in those that cover two or more decades, O-C differences don't appear in random but have a clear structure. This fact was linked with possible orbital period changes in the binary system since random photometric fluctuations does not presumably cause a systematic distribution of the O-C differences. From equation 1.1 this link is obvious. We will see that the complex formation of O-C diagrams does not let us to extract directly safe conclusions about the orbital period of binary systems.

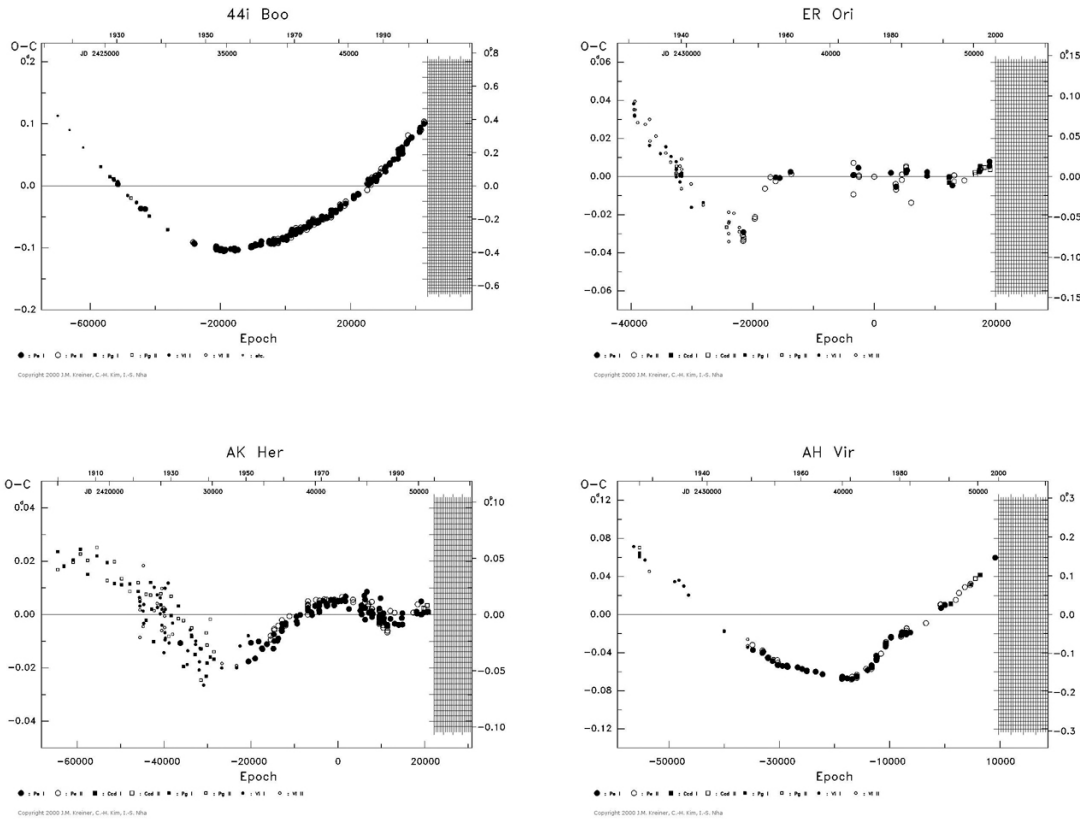


Figure 1.1: Samples of O-C diagrams : 44i Boo, ER-Ori, AK Her, AH Vir

**O-C Diagrams of W Uma Systems** The consideration of all available O-C diagrams of W Uma systems can lead us to a few important considerations :

1. Diagrams that cover two or three decades reveal the existence of well formed relations of the form :  $O - C = f(E)$  that in the margins of observational errors make O-C differences a clear function of time. The clarity of these functions of the W Uma systems is not affected even when the O-C diagram is consisted of multicolour differences or by differences that refer not only in primary eclipses but in secondary too.

2. In some systems O-C differences obtain values so great that can be compared to the orbital period. On such example is 44i Boo in figure 1.1. This means that the arrivals or delays of times of minimum are so great that the computed times are completely different from those observed.

From various studies it is confirmed that the O-C diagrams of most types of binary systems appear to have many similarities. Almost all appear to have changes of alternating character. In a small percentage less than 10% of the systems these changes are periodical. The time scale of these changes is from one to ten years. Also one of the first things that were realized is that O-C diagrams with the most complex behaviour belong to systems of the W uma and RS CVn type(Sahade & Wood 1978).

### 1.3 O-C Diagram Creation And Changes Of The Orbital Period

In order to understand the information that O-C diagrams carries it is necessary to examine the way they are created. The creation involves two procedures, the creation of an O-C difference during the random orbital cycle because of a dynamical or photometric cause and the effect of this difference in all the next orbital cycles. The formation of an O-C difference can be caused dew to photometric causes, to apparent changes (linked with dynamical phenomena) or to real changes of the orbital period.

First of all let's see how an O-C difference affects all the next cycles. Suppose we have an ecliptic system with an orbital period of  $P = P_e$  and an ephemeris of minimum light

$$C_e = T_0 + P_e \cdot E \quad (1.2)$$

We assume that the system has not yet completed his first orbital cycle ( $E = 0$ ). During the end of this first cycle and the begining of the second, an observer here in earth will record the main eclipse and the corresponding time of minimum light of the system at the moment  $O_1 = T_0 + P_e$  in correspondance with the prediction of equation 1.2 for  $E = 1$ . We assume now that because of a photometric event (eg. the apperance of a dark spot) or a dynamic one (eg. mass transfer) that occurs in the system during the cycle  $E = 1$ , the primary photometric minimum of the next cycle  $E = 2$  is detected by an amount of  $\delta T_2$  later than it was expected. In this case the photometric minimum of the main eclipse instead of being observed at :

$$C_2 = T_0 + 2 \cdot P_e \quad (1.3)$$

as equation 1.2 predicts, it is observed at

$$O_2 = (T_0 + 2 \cdot P_e) + \delta T_2 \quad (1.4)$$

The observer can then be guided to two different assumptions about the disagreement of observed and calculated time of minimum :

**a)** That a difference is created between the real and the calculated time the primary eclipse happens during the orbital cycle  $E = 2$  that equals :

$$(O - C)_2 \equiv O_2 - C_2 = (T_0 + 2 \cdot P_e + \delta T_2) - (T_0 + 2 \cdot P_e) = \delta T_2 \quad (1.5)$$

**b)** That the orbital period of the system changed during the cycle  $E = 1$  and became  $P_2 = P_e + \delta T_2$ . Obviously because the observer measures the orbital period reliant in a photometric phenomena (eclipses), the above time difference  $\delta T_2$  may not be linked with a real orbital period change, but with a photometric fluctuation such as the appearance of a dark spot in one of the two members of the binary system. Because we are interested for the effect of the difference  $\delta T_2$  in the next times of minimum light, we suppose that after the apparent or real period change from  $P_e$  to  $P_e + \delta T_2$  during the cycle  $E = 2$  no other change happens. Then the arrival of the next time of minimum for the cycle  $E = 3$  instead of the time :

$$C_3 = (T_0 + 3 \cdot P_e) \quad (1.6)$$

arrives at the time

$$O_3 = O_2 + P_2 = O_2 + (P_e + \delta T_2) = (T_0 + 2 \cdot P_e + \delta T_2) + (P_e + \delta T_2) = T_0 + 3 \cdot P_e + 2 \cdot \delta T_2 \quad (1.7)$$

and so the main eclipse will be observed with a delay of :

$$(O - C)_3 = 2 \cdot \delta T_2 \quad (1.8)$$

Equation 1.8 tells us that in two orbital cycles after the first event that caused the time displacement of the main eclipse by  $\delta T_2$  the delay in the observation of the main eclipse is doubled. Alike three cycles after the event the delay will be tripled. In general after the N-th cycle the observation of the primary minimum will be done at the moment :

$$O_N = T_0 + N \cdot P_e + (N - 1) \cdot \delta T_2 \quad (1.9)$$

instead of the  $C_E = T_0 + N \cdot P_e$  that would normally be expected. So the O-C difference that will be created during the N-th cycle equals :

$$(O - C)_N = (N - 1) \cdot \delta T_2 \quad (1.10)$$

This last equation proves that the initial delay spreads as a linear function of the orbital cycle. This fact gives to the O-C diagram the form of a straight line. Of course we must underline the fact that even the linear increase of O-C differences, the orbital period remains stable and it is the distance in time of two minimum of light  $(O_{E-})_{E-1}$  end equals with  $P_e + \delta T_2$  in all the next cycles after  $E = 2$ . If now the initial delay instead of happening in cycle  $E = 1$  occurs in the random cycle  $E_0$  then equation 1.10 becomes :

$$(O - C)_E = (E - E_0) \cdot \delta T \quad (1.11)$$

We suppose now that in after some cycles (eg,  $E = 5$ ) an new delay  $\delta T_5$  is further added to the time of arrival of the minimum light. Taking in mind equation 1.9 it is clear that the time of observation of the photometric minimum that is linked with the main eclipse of the cycle  $E = 5$  will be :

$$\begin{aligned} O_5 = O_4 + P_5 &= (T_0 + 4 \cdot P_e + 3 \cdot \delta T_2) + P_5 = (T_0 + 4 \cdot P_e + 3 \cdot \delta T_2) + (O_5 - O_4) \Rightarrow \\ O_5 &= (T_0 + 4 \cdot P_e + 3 \cdot \delta T_2) + (P_4 + \delta T_5) \end{aligned}$$

And because we assumed that  $P_4 = P_3 = P_2 = P_e + \delta T_2$  consequently we have :

$$\begin{aligned} O_5 &= (T_0 + 4 \cdot P_e + 3 \cdot \delta T_2) + (P_e + \delta T_2 + \delta T_5) \Rightarrow \\ O_5 &= (T_0 + 5 \cdot P_e) + 4 \cdot \delta T_2 + \delta T_5 \end{aligned} \quad (1.12)$$

The moment  $C_5$  that the photometric minimum should be observed if the orbital period of the system was constantly stable according to equation 1.2 is :

$$C_5 = T_0 + 5 \cdot P_e \quad (1.13)$$

From equations 1.12 and 1.13 we see that the difference  $(O - C)_5$  is :

$$(O - C)_5 = 4 \cdot \delta T_2 + \delta T_5 \quad (1.14)$$

For the observer back in earth this fact is translated to a new real or apparent increase of the orbital period from the value  $(P_e + \delta T_2)$  to the value  $(P_e + \delta T_2 + \delta T_5)$ . The propagation of the delay  $\delta T_5$  to the following cycles will be done in the same way as  $\delta T_2$  did. It will create a new straight line but with different angle. As it is obvious from figure 1.2 positive slope changes of an O-C diagram are linked with an increase in the orbital period, whereas negative slope changes are linked with a decrease in the period. Also in figure 1.2 is added one more delay ( $\delta T_9$ ) wich occurs in the ninth orbital cycle. It is clearly seen that when the period remains stable the form of the O-C diagram is a straight line.

From the above analysis we can conclude that the O-C difference that will be created at the N-th orbital cycle after the indroduction of  $\delta T_5$  will be :

$$(O - C)_N = (N - 1)\delta T_2 + (N - 3)\delta T_3 \quad (1.15)$$

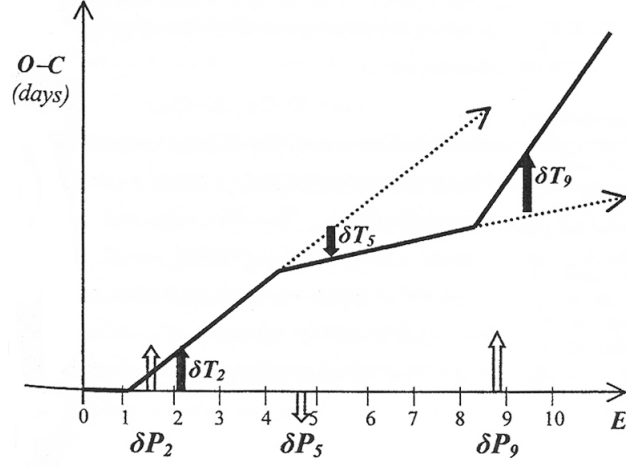


Figure 1.2: Hypothetical O-C diagram.

If we take a more general case when the changes in the arrival of the photometric minimum is made at random cycles we take the equation that gives us the O-C difference during the cycle  $E$  is :

$$(O - C)_E = (E - E_j)\delta T_j + (E - E_k)\delta T_k \quad (1.16)$$

Where the change  $\delta T_j$  happens during the cycle  $E_j$  and  $\delta T_k$  happens during  $E_k$ .

In general a binary system appears to have contiguous period changes at random orbital cycles. Then the equation that will give us the O-C difference in the cycle  $E$  will be the sum :

$$(O - C)_E = \sum_{k=0}^{N=E-E_0} (E - E_0 - k) \cdot \delta P_{k+1} \quad (1.17)$$

Equation 1.17 is the direct generalization of equation 1.16. It shows us that in any time interval  $[E_0, E]$  the O-C diagram of a binary ecliptic system forms from the sum of all the individual changes  $\delta P_k$  of the orbital period, that has been introduced in all the previous cycles of  $E$ . The effect of every  $\delta P_k$  in the current difference  $(O - C)_E$  is a linear increase with time. All in all we can conclude that the relation that gives us the function  $P(E)$  during the random orbital cycle  $E$  is :

$$P(E) = P_e + \sum_{E-E_0}^{k=0} \delta P_{k+1} \quad (1.18)$$

Functions like 1.18 of a binary system are called *functions of the orbital period* and are symbolized in general as  $P(E)$ .

## 1.4 Basic Principals Of O-C Diagrams

### 1.4.1 Non-Linear Modulation of O-C Diagrams

We saw in the previous section that every real or apparent change of the orbital period leads in linear increase or decrease of the O-C differences. Thus if we make the assumption that the period of a binary system shows instantaneous changes then the O-C diagram will be composed by successive straight lines that each of them will show a slope change equal to the period change.

One of the basic principals of O-C diagrams is their non-linear modulation from the real or apparent changes of the orbital period. This attribute means that even if equal period changes happens the corresponding slope changes will not be equal but every change will be smaller and smaller. Let's suppose that in some orbital cycle (eg.  $E_1$ ) the slope of the diagram is  $\varphi_1$  and because of a change  $\delta P$  during cycle  $E_2$  the slope becomes  $\varphi_2$ , then the diagram presents a turn by an angle of  $\delta\varphi = \varphi_2 - \varphi_1$ . So we have :

$$\delta P = \delta T_2 - \delta T_1 = [(O - C)_2 - (O - C)_1] - [(O - C)_1 - (O - C)_0]$$

and because every change propagates linear in the O-C diagram and because  $\delta P$  is the change per orbital cycle, we have :

$$\begin{aligned} \delta P &= (E_2 - E_1) \tan \varphi_2 - (E_1 - E_0) \tan \varphi_1 = \tan \varphi_2 - \tan \varphi_1 = \tan(\varphi_1 + \delta\varphi) - \tan \varphi_1 \Rightarrow \\ \delta P &= \frac{\tan \varphi_1 + \tan \delta\varphi}{1 - \tan \varphi_1 \cdot \tan \delta\varphi} - \tan \varphi_1 \end{aligned}$$

and by the elimination of index '1' we have :

$$\tan \delta\varphi = \frac{\delta P}{\tan^2 \varphi + \delta P \cdot \tan \varphi + 1} \quad (1.19)$$

Equation 1.19 gives the change in the slope of an O-C diagram when the orbital period changes by  $\delta P$  during the random cycle  $E$ . It proves that the effect of  $\delta P$  to the slope of the diagram depends in a non-linear way from the local slope ( $\tan \varphi$ ) that the diagram appears to have at the cycle  $E$ . This fact can be seen in figure 1.3. It is an O-C diagram from instant changes of the orbital period  $\delta P$  that happens during cycles  $E_i$ . It is clear that equal changes of period do not produce equal changes in the slope  $\delta\varphi_i$ .

In conclusion from equation 1.19 we can note that any changes in the period, are spotted more easily when they happen in a horizontal branch of the O-C diagram instead of a branch with a big angle.

### 1.4.2 Formation of O-C Diagrams from Constant and Stable Rate Changes of Period.

The next level of complexity after the sudden changes in an O-C diagram is when the period of a binary system changes constantly with a stable rate of  $\dot{P} = \delta P$ . By applying equation 1.17 we find

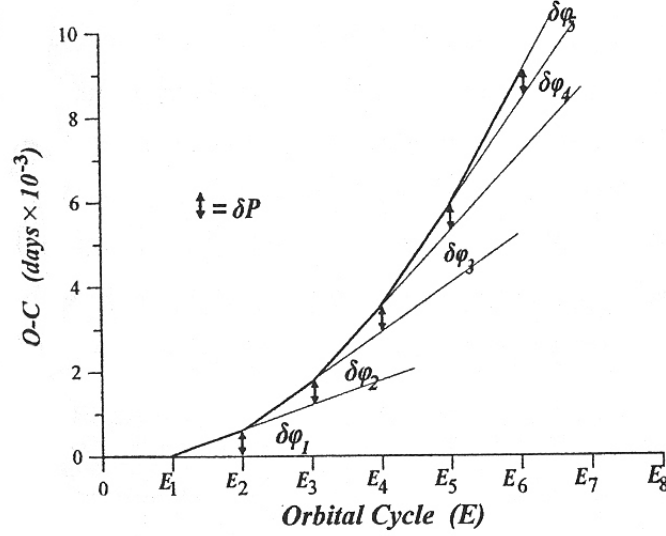


Figure 1.3: Non-Linear modulation of slope.

that during the random cycle  $E$ , O-C differences that an observer will record, will be given as a function of time by the equation :

$$(O - C)_E = \sum_{k=0}^{E-E_0-1} (E - E_0 - k) \cdot \delta P = \delta P \cdot \sum_{k=0}^{E-E_0-1} (E - E_0 - k) \Rightarrow$$

$$(O - C)_E = \frac{E \cdot (E + 1)}{2} \cdot \delta P = \frac{\delta P}{2} \cdot E^2 + \frac{\delta P}{2} \cdot E \quad (1.20)$$

Equation 1.20 proves that the O-C diagram has the form of a parabolic arc. This conclusion of course it applies and in reverse. Namely if an O-C diagram has the form of a parabolic arc with equation  $\alpha E^2 + \beta E + c$  then the change in the period will be  $\delta P_E = 2\alpha$ .

### 1.4.3 Observational and Photometric Noise in O-C Diagrams

From all of the above it is obvious that the knowledge of  $\delta T_E$  of an O-C diagram in every orbital cycle, can lead us to the calculation of the real or apparent changes in the period of a binary system. The problem is that the knowledge of the function  $\delta T_E = \delta T(E)$  requires the knowledge of the O-C differences for every cycle  $E$  with  $E_{min} \leq E \leq E_{max}$ . Obviously this is not possible because the observations can not cover in a continuum way all the orbital cycles. In actual the O-C differences are only sporadically known since big time ranges are not covered at all by observations. But even if the coverage of the diagram was continuum some procedure of smoothing should be applied to the data, in order to neutralize the effect of errors. These errors of course is called noise and it is separated in two categories, photometric and observational noise.

Observational noise is caused by :

a) The errors of determination in the exact time of minimum light of the main or secondary eclipse.

b) The interference by the earth's atmosphere, that causes the scatter of photometric observations.

c) The effects of the instruments involved at the observations, such as telescopes, cameras, filters etc. . .

The most important of the above is the first one. Usually observational noise is at a level of  $\pm 0.001$  of the orbital period. This means that in contact binaries this noise is about  $\pm 20$  to  $\pm 60$  sec.

In this point we must clear out an important thing. Whereas the accuracy of determination the photometric minimums is in the scale of one minute, the changes that can be found after analyzing an O-C diagram are extremely good and in the scale usually of  $10^{-6}d$  ( $0.1sec$ ). The cause for this is the linear increase of the O-C differences with time. This means that because the period of W Uma systems is very small ( $< 1d$ ), even a period change of  $0.1sec/E$  can be detected after at the most 40 orbital cycles. This happens when the O-C differences overcome the noise floor because of their linear increase.

Photometric noise on the other side is caused by phenomena in the surface of the stars, like anomalies in symmetries and variable distribution of the temperature. These anomalies have the effect of the separation of the moment of photometric eclipse from that of the real eclipse.

## 1.5 Photometric Noise and Apparent Period Changes

As it has been said the appearance of O-C differences in the diagram of a binary system be caused equally to real or apparent changes of the orbital period. Apparent variations can have either a dynamical or photometric origin. The first of these variations are caused by phenomena like the light-time effect or the metathesis of the periastron of the orbit. Photometric variations on the other hand are caused by phenomena like starspots, flares and in general various phenomena in the photosphere of the stars. The most important cause of course of photometric variations is starspots. Let's say a few things about them.

Let us assume that  $P$  is the orbital period of an eclipsing binary and that the light minimum at the primary eclipse during the orbital cycle  $E$  has been shifted by  $\delta\varphi$ . The epoch of this minimum will be displaced from the proper time  $T_E$  by  $\delta t = \delta\varphi \cdot P$  According to Geyer (1977), this  $\delta\varphi$  may reach values of about 0.005. For a binary with an orbital period of about  $1d$ , such a phase shift will give the impression that an orbital period change equal to  $\delta t = \delta\varphi \cdot P \approx 5 \cdot 10^{-3}d$  has occurred. Consider now a contact binary with a constant orbital period  $P_0$ , having synchronised components and an orbital inclination  $i = 90^\circ$ . The position of any spot on the surface of the  $j$ -component will be denoted by  $(\theta, \lambda)_j$  ( $j = 1, 2$ ), where  $\theta$  is the longitude and  $\lambda$  is the latitude. On each component,

the longitude  $\theta$  is measured with respect to the meridian which passes through the centre of the visible disk at the moment of inferior conjunction. This longitude  $\theta$  is considered positive when a spot is situated on the leading hemisphere. We further assume that the spots are circular (with an angular radius  $r_S$ ), and that the temperature difference with respect to the surrounding photosphere is  $\delta T$ . Such a spot can cause a phase shift of the light minimum only if the following restrictions hold at the time of conjunction:

**a)** No other spot with the same physical characteristics ( $r_S, \delta T$ ) exists within the positions  $(-\theta, \lambda)$  or  $(-\theta, -\lambda)$  of the stellar disk.

**b)** The longitude of the spot is within the interval  $90^\circ - r_S \leq \theta \leq 90^\circ + r_S$

If restriction (a) is not satisfied, then two identical spots exist symmetrically with respect to the reference meridian or to the center of the stellar disk. In such a case, one spot cancels out the effects of the other. If restriction (b) is not valid, then the starspot is not visible during the primary eclipse. Several studies have indicated that starspots on close binaries have angular diameters ranging from  $10^\circ$  to  $40^\circ$ , which means that they may cover from 5 to 25% of the whole photosphere of the active components. Although it is not clear whether such dark areas consist of a group of many small spots or of just one giant spot, the second option seems to prevail. In most cases, the active component seems to possess one or two giant spots. It is also argued that such spots can remain on the surface of the active component even for 10 years, or equivalently, over a thousand orbital revolutions. Hence, starspot characteristics are different from those of sunspots, since even at solar cycle maximum the sunspots rarely cover more than 1 to 2% of the solar photosphere, and their lifetimes never exceed 3 to 4 solar revolutions.

As for the W UMa type binaries, observations have shown that approximately 20% to 30% of all known contact binaries possess one or two giant spots with angular diameters  $10^\circ$  to  $35^\circ$  and  $\delta T \approx 500$  to  $1500K$ . Two remarks can be readily made :

**i)** Spots with the same angular diameters cause significantly greater phase shifts when they lie on the primary component.

**ii)** Spots on the secondary having  $r_S < 10^\circ$  cause negligible shifts of the light minimum of the primary eclipse.

The important conclusion (kalimeris et al. 2002) is that the effect of starspots at the members of a binary systems leads to the introduction of high frequency noise to the O-C diagrams. This noise is limited to a zone with a width of  $\pm\epsilon_{phot}$  on either side of the zero level of the diagram, when the period is stable, or on either side of the systematic orbital period variations that modulate the diagram. Instead of real period changes, a starspot as any other photometric variation, can not produce permanent changes in the slope of an O-C diagram. So any O-C diagram carries information

about period changes. These changes can be either real or apparent. If they are apparent then it can be either photometric or dynamical. From the above we conclude that if the changes are apparent then it can only be of dynamical nature. The next section is involved with the formation of O-C diagrams from dynamical phenomena.

## 1.6 O-C Diagram Formation

In binary systems, it is known that there is dynamic phenomena that even if they don't alter the period of the system, they lead to the introduction of O-C differences. These differences could then be linked with period changes that of course are not real but apparent. Such phenomena are the nutation of the line of apsid and the light-time effect.

In binary systems, it is known that there is dynamic phenomena that even if they don't alter the period of the system, they lead to the introduction of O-C differences. These differences could then be linked with period changes that of course are not real but apparent. Such phenomena are the nutation of the line of apsid and the light-time effect. In binary systems, it is known that there is dynamic phenomena that even if they don't alter the period of the system, they lead to the introduction of O-C differences. These differences could then be linked with period changes that of course are not real but apparent. Such phenomena are the nutation of the line of apsid and the light-time effect. Here only the light-time effect will be analyzed in depth.

### 1.6.1 O-C Differences From The Light-Time Effect

The existence of a third star in a binary system it does not only cause the line of apsid to rotate, but also a periodic variation of the distance of the center of mass ( $K_2$  from earth. As a consequence of that the time the light needs to reach earth is subject to small variations, that are detectable through the O-C differences. Because the center of mass of the binary system tracks an elliptical orbit in respect to that of the third star, it can be proven that the distance at a random moment  $t$  is given by the equation :

$$S = s_0 + v_{ob}(t - T_0) + \alpha'(1 - e' \cos \epsilon') \sin i' \cdot \sin(v' + \omega') \quad (1.21)$$

where  $s_0$  is the distance of  $K_2$  from earth during the initial moment  $T_0$ ,  $v_{ob}$  is the component of speed of the triple system at the direction of the observation.  $\alpha'$  is the length of the semi-axis of the orbit of the  $K_2$ ,  $e'$  is the eccentricity of the orbit of  $K_2$ ,  $i'$  is the inclination of the orbit of the third star,  $\omega'$  is the length of the periastron of the orbit and  $v', \epsilon'$  is the real and acentric anomaly of the third star during the moment  $t$ .

If for the length  $D'$  of the semi-axis of the relative orbit of the third star applies  $D' \gg D$ , then for  $\alpha'$  we have the two body problem :

$$\alpha' = \frac{m_3}{m_{1,2} + m_3} \cdot D' \quad (1.22)$$

By using the proper spread of the quantities  $1 - e' \cos \epsilon'$ ,  $\sin v'$ ,  $\cos v'$  in respect to the mean anomaly  $M'$  of the third body, we can have the time distance of the center of mass of the binary system from earth. This is given by the "light" equation :

$$\begin{aligned} \frac{S}{c} = v_{ob} + \frac{\alpha' \cdot \sin i'}{c} \left[ -\frac{3}{2} e' \sin \omega' + \left(1 - \frac{1}{2} e'^2\right) \sin \left(2\pi \frac{P}{P'} E + N'_0 + \omega'\right) - \right. \\ \left. -\frac{1}{8} e'^2 \sin \left(2\pi \frac{P}{P'} E + N'_0 - \omega'\right) + \frac{1}{2} e' \sin \left(4\pi \frac{P}{P'} E + 2N'_0 + \omega'\right) + \right. \\ \left. +\frac{3}{8} e'^2 \sin \left(6\pi \frac{P}{P'} E + 3N'_0 + \omega'\right) \right] \end{aligned} \quad (1.23)$$

where  $N'_0$  is :

$$N'_0 = \frac{2\pi}{P'} T_0 + c'$$

and  $c'$  is a constant that is chosen in such way that the value of the mean anomaly during the moment  $T_0$  equals with an observable value of  $M'_0$ . Through equation 1.23 it can be proved that the moment of observation of the photometric minimum of the main eclipse during the orbital cycle  $E$  is given by :

$$\begin{aligned} (O - C)_E = T_0 + P \cdot E + \frac{v_{ob}}{c} P \cdot E + \frac{\alpha' \cdot \sin i'}{c} \cdot \left(1 - \frac{1}{2} e'^2\right) \cdot \sin \left(2\pi \frac{P}{P'} \cdot E + N'_0 + \omega'\right) + \\ + \frac{1}{8} e'^2 \cdot \frac{\alpha \sin i'}{c} \cdot \sin \left(2\pi \frac{P}{P'} \cdot E + N'_0 - \omega'\right) + \\ + \frac{1}{2} e' \cdot \frac{\alpha' \sin i'}{c} \cdot \sin \left(4\pi \frac{P}{P'} \cdot E + 2N'_0 + \omega'\right) + \\ + \frac{3}{8} e'^2 \cdot \frac{\alpha' \sin i'}{c} \cdot \sin \left(6\pi \frac{P}{P'} \cdot E + 3N'_0 + \omega'\right) \end{aligned} \quad (1.24)$$

The sum of the last five terms of equation 1.24, gives the equation of the O-C differences as a function of the orbital cycle  $E$  :

$$\begin{aligned} (O - C)_E = \frac{v_{ob}}{c} P \cdot E + \frac{\alpha' \cdot \sin i'}{c} \cdot \left(1 - \frac{1}{2} e'^2\right) \cdot \sin \left(2\pi \frac{P}{P'} \cdot E + N'_0 + \omega'\right) + \\ + \frac{1}{8} e'^2 \cdot \frac{\alpha \sin i'}{c} \cdot \sin \left(2\pi \frac{P}{P'} \cdot E + N'_0 - \omega'\right) + \\ + \frac{1}{2} e' \cdot \frac{\alpha' \sin i'}{c} \cdot \sin \left(4\pi \frac{P}{P'} \cdot E + 2N'_0 + \omega'\right) + \\ + \frac{3}{8} e'^2 \cdot \frac{\alpha' \sin i'}{c} \cdot \sin \left(6\pi \frac{P}{P'} \cdot E + 3N'_0 + \omega'\right) \end{aligned} \quad (1.25)$$

In equation 1.25 excluding the first term that is the cause of the motion of the system trough the galaxy, the rest of the terms are functions of sine of the main angle  $2\pi PE/P'$  and of it's multiples. The first periodic term of equation 1.25 has the biggest width and of course is the strongest. So

equation 1.25 shows that the O-C diagram of a binary system that is accompanied by a third star, will have a sinusoidal form with a width of :

$$B \approx \frac{\alpha' \sin i'}{c} \cdot \left(1 - \frac{1}{2}e'^2\right) \tag{1.26}$$

Of course except of the main frequency  $P/P'$  there will be and it's harmonics  $2P/P'$ ,  $4P/P'$ ...

In figure 1.4 is the O-C diagram of 44i Boo, which is one the few systems that is an astrometric triple system. The apparent orbit is in the same figure, the theoretic form of the O-C diagram as expected from equation 1.25 is the continuum line and the points are the observed data. We must be

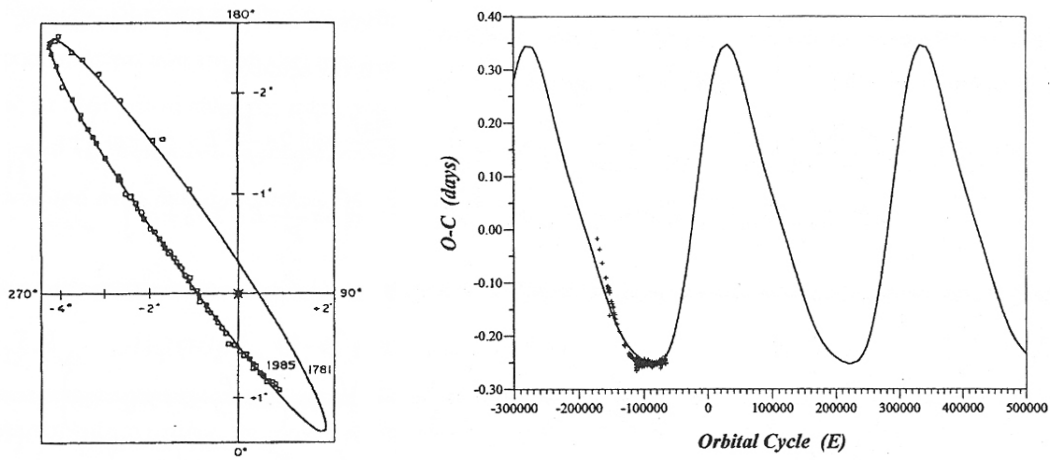


Figure 1.4: Apparent orbit and theoretical O-C diagram of 44i Boo.

very careful with any diagrams that have a sinusoidal form. This of course is not right, to explain all the periodic data from O-C diagrams of contact binaries with the light-time effect, it is required the existence of a third star with such masses that normally it could have been detected photometrically or with spectrums. So a periodic O-C diagram is probably related with internal physical processes that happen in the members of the system.

## Chapter 2

# Analysis Methods Of O-C Diagrams

*“Observing Closer Part II ...”*

### 2.1 The Classical Analysis Model

In previous paragraphs we have seen that the simpler formation of an O-C diagram, is from sudden changes of the orbital period. The produced O-C diagram is constituted from straight segments, that form an angle between them at the point where a sudden change is happened. The tangent of this angle is equal to the change in the orbital period. These simple facts they compose a technique that has been used the last four decades for the analysis and interpretation of O-C diagrams. According to this technique, in an O-C diagram that has the form of a straight line the orbital period is stable, the points of section of successive straight segments in the diagram they fix the points that the orbital period is changing.

This is the oldest method for analysing O-C diagrams of eclipsing binary systems, it is known as "step variations model". Apart from this simple method of analysis it exists another one method that it is called "constant rate variations model". For this model at the intervals that an O-C diagram has the form of a parabolic arc with an equation  $\alpha E^2 + \beta E + c$ , the orbital period changes with a constant rate of  $\dot{P} = 2\alpha$  and vice versa. The above two methods form what is known as the "classic model" for analysing O-C diagrams. According to this model, O-C diagrams present the following characteristics :

- Successive straight segments with sudden changes of their slope
- Parabolic arcs
- Sinusoidal changes
- Irregular changes

By applying this model to a binary system you can find the  $P(E)$  function that is to say, the period changes vs orbital cycle. To the establishment of the classic model helped the fact that we know a few physical mechanisms that lead to the formation of parabolic arcs in O-C diagrams, such as chemical or thermal evolution of the members of the binary system as well as the interaction of tides and stellar wind.

**Analysis and Description with the classic model** The basic element of the analysis with the classic model of an O-C diagram, is that the personal judgment of the investigator plays a big role. The steps to analyze with that method is :

First of all with an optical examination of the diagram it is decided if the timeseries will be described by a parabolic arc, by a straight line or by a sinusoidal line. In most cases it's not possible to describe all the diagram with a single line. This is because all O-C diagrams that have a duration longer than 10 – 20 years are complicated. The reason for this is that it is much more likely to document the various mechanisms that change the orbital period of the system in a big time interval. Consequently if one is limited in small time intervals, he can always find segments of the diagram that can be described by straight lines or parabolic arcs. This is true even in the most complicated diagrams. The final calculation of the  $P(E)$  function is done by simple adding the various segments (straight or parabolic). Of course the points of intersection of straight and parabolic arcs make the  $P(E)$  function inconsecutive.

## 2.2 Why The Classic Model Is Wrong?

It is very easy to see now why the classic method is wrong. There is three important points that the method is wrong and not consistent with the physical reality.

**A)** The description of a random time series with consecutive straight lines and parabolic arcs is wrong because it is in the arbitrary choice of the observer in how he will make the analysis. Different observers give different results

**B)** Classic model presumes arbitrary things about the physical mechanisms that give the observed period changes. It is not possible for a system that underlies a sudden period change to alter its physical constants in such a way that it can go from a stable state to another stable state immediately.

**Mathematical failure of the Classic Model** The most interesting fact in contact binary systems is their complex behaviour. This is translated into complex O-C diagrams that in most of the systems are chaotic, with no visible periodicity. An O-C diagram can be analyzed with many different ways by a means of combinations of straight lines and parabolic arcs. Every such analysis

of course leads to a dramatically different interpretation of period changes. This means that the classic method does not ensure the univocal determination of the  $P(E)$  function.

Another point that comes in direct conflict with the theory of the classic model, is the property of O-C diagrams to have radically different form when they are produced from different linear ephemeris equations, for the same binary system. It is very common for every observer to choose arbitrary the constants  $T_0$  and  $P_0$  that form the linear ephemeris. In practice all linear ephemeris are in equivalence with each other. This is shown in figure 2.1 of AB-And that is formed of three linear ephemeris with common  $T_0$  but with different period  $P_0$ . It is  $T_0 = 2425497.48$  J.D. and  $P_{e1} = 0.33188638$  d,  $P_{e2} = 0.33189305$  d and  $P_{e3} = 0.331889$  d. Because of the non-linear modulation of the O-C differences,

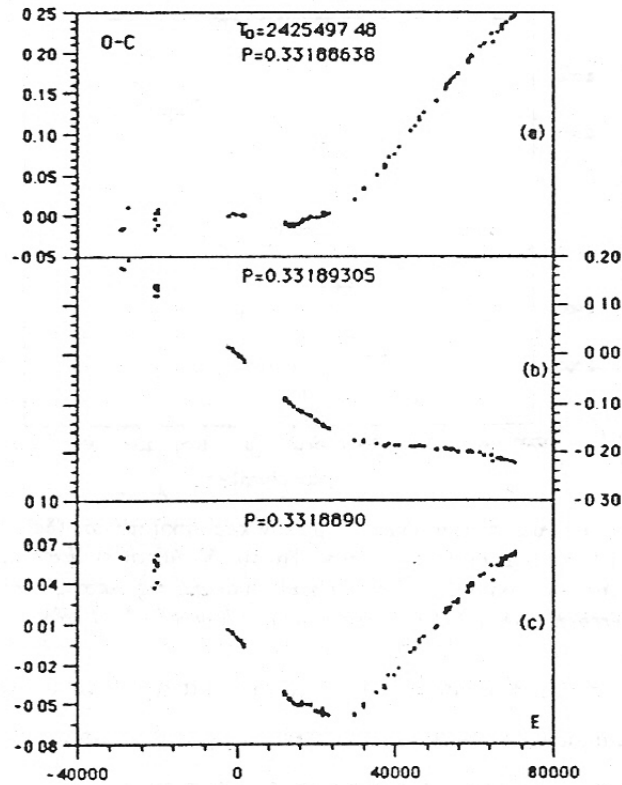


Figure 2.1: O-C Diagram of AB-And formed by three different linear ephemeris

it is clear that there is the possibility in one diagram an orbital period change to be easily detectable and in some other diagram not to. Because of all these we can understand now that in every O-C diagram that is computed with a different linear ephemeris, it will be described with a totally different way with the classic model, leading to different  $P(E)$  functions. Consequently by only this fact the classical analysis method is inappropriate for the description of random time series, like the time series that are observed in contact binary systems.

**Physical Failure of Classic Method** The classic method of analysis is based upon the hypothesis that the orbital period of binary systems changes in a non-continuous manner. The description with successive straight lines implies that in the corresponding time span the orbital period is completely steady, that are only interrupted by sudden changes in the order of 0.1 – 1 sec and then again a steady period. So the classic model says that the period of the system follows a step form. That's why it is also known as the step-variations model.

The real problem is that it is very difficult to find a physical mechanism to produce such a behaviour. And even if we could find such a mechanism there is no way to explain the speed in which the system dampens an orbital variation. It is widely known from any structure model about binary systems that there is no systems with such a behaviour. So all systems must follow a continuous variation of their parameters after a change in their orbital period<sup>1</sup>. Especially in contact binary systems the above point is much more important because of the close proximity of the members. All in all the theory of the classic analysis method comes in complete opposition with the physics of contact binaries (and any binary system). It can be proven that in systems that are in a state of tidal equilibrium, and that their members do not change their radius, under a conservative situation, that mass transfer can cause orbital changes that are given from the equation :

$$\frac{dP}{P} = 3 \frac{2\mu' - 1 dm}{\mu'(1 - \mu')M} = 3 \frac{1 - q^2 dm}{qM} \quad (2.1)$$

where  $\mu' = M_2/(M_1 + M_2)$ . So it is clear now that even after a sudden change in the orbital period the mass transfer continues to undergo with various rates for a period of time  $t_{K-H}$  therefore the orbital period will also have similar variations.

---

<sup>1</sup>Of course an orbital period change can be caused by many reasons, but mainly by a mass transfer from one member to the other, resulting to a point to an O-C diagram

## 2.3 The New Kalimeris Model of O-C Analysis

From all of what we said until now it is clear that there is the need of a new method of analysis and interpretation of O-C diagrams and the information that they contain. This new method must follow the physics limitations as well as the mathematical too. So A. Kalimeris proposed this new method in 90's. The method quickly became very popular and now is widely accepted as the best and correct method to follow for the O-C diagram analysis. It is very easy to understand why, it says what is obvious from mathematical and physical point. It adopts a non-linear fitting procedure in contrast to the linear one of the classic method.

### 2.3.1 Least Squares Polynomial Description of O-C Curves

It is widely known that the use of a function that fits with the best way time series data is the most appropriate solution for analysis because ensures the necessary removal of photometric and observational noise and at the same time complies with the physics of binary systems. There are many such methods of analysis, but originally Kalimeris choose the least square polynomial fitting with Chebyshev or Legendre polynomials, mainly because of its ability to have easy to understand results and have very good behaviour that has in difficult points of an O-C diagram<sup>2</sup> and of course of the way it handles errors.

The most important thing is something other. It is the independence of the method is used to fit the time series. The analysis model that Kalimeris proposed is independent and globally accepts methods like ARMA (Autoregressive moving model) or Fourier transforms to find the spectrum of the time series. Of course there is only one restriction. Any method of fitting that the person who does the analysis must comply with the physics of contact and in general binary systems. So from now on I will present you the version of Kalimeris model with a least square polynomial fitting procedure.

A polynomial description of a time series is given by the equation :

$$S_m(E) = c' \sum_{j=1}^m c_j \prod_j (E') \quad (2.2)$$

A common problem with such a fitting method is that many times it can not describe the whole set of data with just one polynomial. The way to deal with this is the piecewise approximation. The pieces of the diagram uses every time a different polynomial description of the form of 2.2.

In equation 2.2  $\prod_j (E')$  is the j-polynomial Chebyshev or Legendre and  $E'$  is the normalized orbital cycle that is defined as  $E' = E/c'$  where  $c'$  is a constant that is chosen freely in such a way to  $N/c' < 1$  where  $N = E_{max} - E_{min}$  and  $E_{max}, E_{min}$  is the maximum and minimum orbital cycle that an O-C diagram covers. The above transformation of time coordinates is necessary because

---

<sup>2</sup>points with very fast and steep change in their inclination

Chebyshev and Legendre polynomials are defined only for  $-1 \leq x \leq 1$ . The factors  $c_j$  are computed by least squares theory, so after the necessary calculations equation 2.2 can be written as :

$$\Delta T(E) \equiv S_m(E) = c' \sum_{j=1}^m c_j E'^j \quad (2.3)$$

Where  $\Delta T(E)$  from now on will be the best fitting of an O-C diagram as a function of orbital cycle  $E$ . The degree of the polynomial used can be selected by just looking a diagram of mean square error ( $\epsilon_{rms}$  figure 2.2). Here we must point some important things. There is no meaning of  $\epsilon_{rms}$  to become smaller of the noise floor of an O-C diagram, and second that there is a maximum value of  $m$  that the polynomial is becoming unstable and appears to have oscillations of increasing amplitude. This is clearly seen in figure 2.2. When such oscillations starts before  $\epsilon_{rms}$  equals the noise floor<sup>3</sup>, then the method of piecewise approximation is obligatory. If piecewise approximation is used then

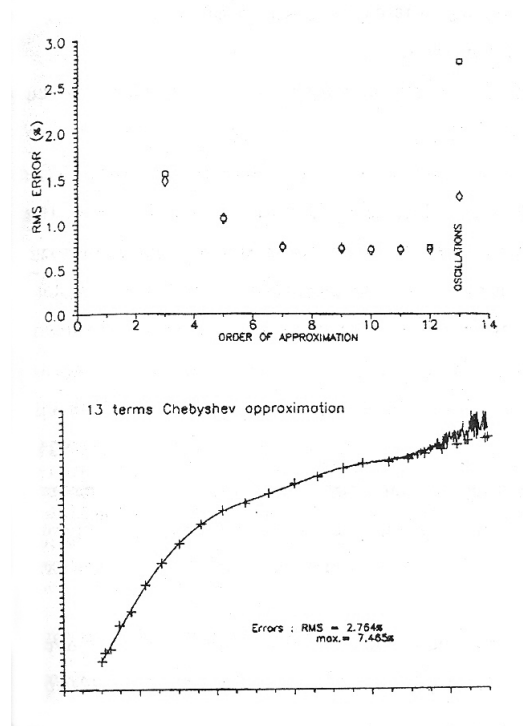


Figure 2.2: Behaviour of the mean square error ( $\epsilon_{rms}$ ) as a function of the order  $m$  of the Chebyshev polynomial

we must be very carefull not to fail the physics of binary systems. For this not to happen we must connect each piece of the diagram with a cubic spline. In each connection point we have some constrains :

$$\frac{d\Delta T_j(E)}{dE} = \frac{d\Delta T_{j+1}(E)}{dE} \quad (2.4)$$

<sup>3</sup>Photometric and observational noise see section 1.5 for details

and

$$\frac{d^2 \Delta T_j(E)}{dE^2} = \frac{d^2 \Delta T_{j+1}(E)}{dE^2} \quad (2.5)$$

These constrains 2.4, 2.5 as i already said are satisfied by a cubic spline connection.

**The Kalimeris Model of O-C Analysis** Since i described the implemetation of least square fitting with a Chebyshev or a Legendre polynomial to O-C time series data of contact binary systems, it is time to describe the main core (and intepented of the fitting procedure) of the Kalimeris model. The main thing we are searching during the analysis of O-C diagrams is the  $P(E)$  function. Having already found the  $\Delta T(E)$  function that gives the O-C differences in every orbital cycle  $E$  we have this obvious equation :

$$O(E) = C(E) + \Delta T(E) \quad (2.6)$$

using the above equation and knowing the definition of the observed value of the orbital period<sup>4</sup> we can conclude that the  $P(E)$  function during a random cycle  $E$  is given by :

$$P(E) = O(E) - O(E - 1) = [C(E) + \Delta T(E)] - [C(E - 1) - \Delta T(E - 1)] \Rightarrow$$

$$P(E) = \left\{ [T_0 + (E - E_{min})P_e] + \Delta T(E) \right\} - \left\{ [T_0 + (E - 1 - E_{min})P_e] + \Delta T(E - 1) \right\} \Rightarrow$$

$$P(E) = P_e + \Delta T(E) - \Delta T(E - 1) \quad (2.7)$$

Equation 2.7 is a general expresion that gives the observed value of the orbital period , intepented of the description method that is used for the analysis of an O-C diagram through a fitting procedure. Through equation 2.7 we can find the rate of change of the orbital period per orbital cycle. It would be :

$$\dot{P}(E) = \Delta T(E) - 2\Delta T(E - 1) + \Delta T(E - 2) \quad (2.8)$$

The above equation is also a general one, so in our specific situation that we use a least square method for the description of the time series, equation 2.8 will be :

$$\dot{P}(E) = \frac{dP}{dE} = \frac{1}{c'} \left[ \sum_{k=0}^{m-1} (k+1)c_k E'^k - \sum_{k=0}^{m-1} (k+1)c_{k+1} \left( \frac{E-1}{c'} \right)^k \right] \quad (2.9)$$

Thus with equations 2.7 and 2.8 we can calculate the variations of the orbital period of any binary system, of course inside the limits of observational and photometric noise.

---

<sup>4</sup>Orbital period is defined as the time between two minimum in the light curve of the same type. Meaning the time between two main or two secondary eclipses.

### 2.3.2 Noise Handling with Chebyshev Polynomials in Kalimeris Model

In the previous paragraph it was mentioned that the kalimeris model is intepented of the method used for fitting the time series data of an O-C diagram. But the method of least square fitting with a Chebyshev polynomial was prefered from others for very spesific reasons. These are that this spesific type of polynomials has a very nice way of handling the photometric noise<sup>5</sup>.

It can be proved that the least square fitting with a Chebyshev polynomial is equivelant with a partial development in Fourier series. Thus equation 2.2 can be writen :

$$S_m(x) = \frac{\alpha_0}{2} + \sum_{k=1}^m \alpha_k T_k(x) = \frac{\alpha_0}{2} + \sum_{k=1}^m \alpha_k \cos(k\theta) \quad (2.10)$$

Where  $S_m(x)$  is the least square fitting of the data. The above property of Chebyshev polynomials allows us the filtering of photometric noise, by cutting off the terms of the developed series that show a frequency larger or equal to  $v_s$ . Where  $v_s$  is the frequency of photometric noise and equals  $v_s = \frac{\Delta P}{P}$ .

## 2.4 Existence of a Third Body in Binary Systems

The existence of a third body in orbit around an eclipsing binary, introduces a harmonic term in the O-C diagram due to the light-time effect. Such an oscillation can be detected in two ways :

- Through the residuals formed between the observed differences O-C and the best fitted polynomial  $\Delta T(E)$ . In simple cases, these residuals have the form of a sinusoid curve. The amplitude and frequency of such terms are used for the determination of the mass function  $f(m)$ .
- Through a spectral analysis of the period function  $P(E)$ . The first method is in common use and is very efficient whenever linear or quadratic terms fit the observations.

However, scarcely an O-C diagram can be described as a whole so easily without loss of important information and inconsistencies relative to the underlying physical mechanisms. Generally, polynomials of high order have to be used in order to describe as much as possible of the fine features of an O-C diagram, light- time due to third body included. When the light-time effect cannot be described by least square polynomials, it manifests itself in the diagram of residuals However, a problem appears whenever a least squares polynomial approximates an existing light-time effect <sup>6</sup>. Then the  $\Delta T(E)$  polynomial is contaminated by the light-time effect which directly distorts the form of the  $P(E)$  function. This, means that  $P(E)$  can show fictitious changes due to an unresolved light-time, although this effect has nothing to do with real orbital period changes. In the following we examine the way the light-time effect affects the  $P(E)$  function.

<sup>5</sup>Photometric noise has a typical value of  $\varepsilon_{phot} \leq 0.01d$  for O-C diagrams of contact binay systems.

<sup>6</sup>Which easily happens when the observations cover a time span comparable to the orbital period of the third body, or when the orbital period of the eclipsing pair suffers relatively rapid and continuous changes like contact binaries do.

We suppose that an O-C curve contains a light-time effect, which in, general can be described by the Fourier series :

$$\sum_{j=0}^{\infty} \left[ \alpha_j \sin(f_j E) + b_j \cos(f_j E) \right] \quad (2.11)$$

Using 2.11 we can find the form of  $P(E)$ , apart from any polynomic terms, as:

$$P(E) = P_e \sum_{j=0}^{\infty} \left[ \alpha_j (1 - \cos f_j) - b_j \sin f_j \right] \sin(f_j E) + \sum_{j=0}^{\infty} \left[ b_j (1 - \cos f_j) - \alpha_j \sin f_j \right] \cos(f_j E) \quad (2.12)$$

Comparing equations 2.11 and 2.12 we can see that, as it was expected, every harmonic term in equation 2.11 generates one harmonic term in 2.12 of the same frequency  $f_j$ , but with different amplitude. The invariable character of the frequency means that any harmonic term of the O-C curve will be also present in the spectrum of the period function  $P(E)$ . In the simple case where the orbit of the third body is circular and coplanar to the orbit of the eclipsing variable, the light-time effect can be approximated by a single sine term, so that  $\Delta T(E)$  becomes (apart from any polynomic terms) :

$$\Delta T(E) = \alpha \sin(fE) = \alpha \sin\left(\frac{2\pi i}{T} E\right) \quad (2.13)$$

where it is supposed that the amplitude of the light-time effect is  $\alpha$  and the orbital period of the third body is  $T$ . Then, according to 2.12 the period function  $P(E)$  of the eclipsing pair will contain the periodic term :  $\alpha(1 - \cos f) \sin(fE) + \alpha \sin f \cos(fE)$ . Given a spectrum of  $P(E)$  that shows the amplitude of sin terms at different frequencies, we conclude that any light-time effect of amplitude  $\alpha$  and period  $T$  will produce a spectral line of amplitude  $\Delta P = \alpha(1 - \cos f)$  at a frequency  $f$ . Then, the apparent orbital dimension of the eclipsing variable motion around the center of mass of the triple system is :

$$\alpha \sin i = c \frac{\Delta P}{(1 - \cos f)} \quad (2.14)$$

Consequently, the mass function will be :

$$f(m) = \frac{(\alpha \sin i)^3}{T^2} = \frac{(M_3 \sin i)^3}{(M_1 + M_2 + M_3)^2} \quad (2.15)$$

and of course can be solved for the mass of the third body  $M_3$ .

As can be seen with a very small arithmetical analysis, third bodies of very small masses are sufficient to explain the spectral components of typical contact binaries of W Uma type. The small values of  $M_3$  are a consequence of the very small values of the  $f(m)$  function. In some cases, the requisite third body mass is so small at only 0.2 of Jupiter's masses that its detection is not possible by present means. So we must be very carefull with such an interpretation of our observational data.

## Chapter 3

# Photometry - Analysis Of Observational Data

In this section i analyze with the Kalimeris method data collected for the system ER Ori. I also present the light curve of this system. The light curve were produced with a Vixen VC200L 8inch, together with an SBIG ST-7 CCD camera. The characteristics of the camera as well as the scripts and software used to analyze the photometric data are presented in table 3.1.

The analysis was done in two main parts. The first one is the implementation of Kalimeris method to collected data and the second one is the reduction of the photometric data obtained with the above equipment. Observations of the stars mainly took place in Mount Xolomon from summer 2004 until winter 2006. Also some observations was done in Larissa.

For the purpose of this diploma thesis new scripts were developed, using the facilities of Starlink. For the data reduction flat dark and bias frames was used. With these scripts an accuracy of 0.01 mag was possible.

<b>Characteristic</b>	<b>Value</b>
A/D Converter	16 bits
A/D Gain	$2.6e^-/ADU$
Read Noise	$15e^-/RMS$
Pixel Digitization Rate	420000 pixel/sec
Pixel Size	9 x 9 microns
Dark Current	$1e^-/pixel/sec$ at 0°C
Pixel Array	765 x 510 pixels, 6.9 x 4.6 mm
Full Well Capacity	$100000e^-$

Table 3.1: SBIG ST7 CCD Camera Characteristics

### 3.1 ER-Ori

The star ER-Ori is a typical contact binary system. It has a period of  $\approx 0.42$  days and it is already been observed from the 30's decade. As a result we have enough observations to conclude some characteristics of its behaviour. At figure 3.1 it is shown the field of the star as it has been observed by me. Also in figure 3.2 it is the light curve of ER-Ori as it was observed by me with the above equipment. In x-axis is the time in JD (Julian date) and in y-axis is the instrumental magnitude (mag). It is a very nice and clean curve that shows that between the maximum and minimum it is  $\Delta mag \approx 0.7 mag$ . The linear ephemeris that was used for the calculation of the O-C values is :

$$\text{MinI} = \text{JD Hel } 2443090.5300 + 0.423399431E.$$

At figures 3.3, 3.4 and 3.5 it is shown the O-C diagram the non-linear fit and finally the diagram of the  $P(E)$  function. As it has already been said, in the case that it is not possible for one polynomial to describe the whole O-C diagram then we must have the fitting in pieces and combine them with a cubic spline. In the case of ER-Ori this was not necessary since only one polynomial described the diagram very well. The only point in the diagram that could possibly need such an analysis is in the space between orbital cycle  $-15000$  through cycle 0. By doing the piecewise analysis I found that there is no benefit from doing it, so I stayed with the simpler one.

So the procedure that I followed was first finding all the times of minima that I could. Some characteristics for these minima is shown at table 3.3. Then with the help of the fortran code that I wrote specifically for this purpose and by using the linear ephemeris given above, I found the O-C values for ER-Ori. Then by using the program gnuplot in linux I plotted and fitted the O-C curve with the polynomial 3.1. The algorithm used for this process was the Marquardt-Levenberg.



Figure 3.1: The Stellar Field of ER Ori (14.5x9.6 arcmin).

For the fitting calculations it was used an polynomial 11<sup>th</sup> order. This polynomial is :

$$\Delta(E) = aE^{11} + bE^{10} + cE^9 + dE^8 + eE^7 + wE^6 + zE^5 + fE^4 + kE^3 + pE^2 + hE + m \quad (3.1)$$

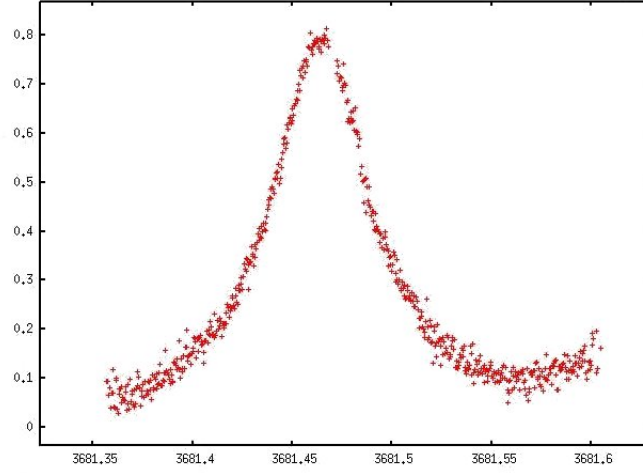


Figure 3.2: The light curve of ER-Ori

Spectral type	B (mag)	V (mag)	B-V (mag)	Ra	Dec
G1V	9.96	9.53	0.43	05h 11m 14s	-08d 33m 24s

Table 3.2: ER Ori Physical Characteristics

The next step was done throu equation 2.7 :

$$P(E) = P_e + \Delta T(E) - \Delta T(E - 1) \quad (3.2)$$

were  $P_e \approx 0.42$  and then i can take the  $P(E)$  function. The coefficients of the polynomial are :

$$a = 865.0813, b = 1417.2678, c = 169.0928, d = -690.0042, e = -191.3116, w = 136.3668, z = 32.9902, f = -13.4859, k = -1.2108, p = 0.5151, h = -0.0246, m = -0.0024$$

Finally the  $P(E)$  function will be :

$$P(E) = 0.42 + \Delta T(E) - \Delta T(E - 1) \quad (3.3)$$

The  $\Delta(E)$  function is the red line at figure 3.4 and as it is clear, it follows the O-C diagram very well. The final behaviour of ER-Ori is shown at figure 3.5. It is very clear that the smallest variations that is observed are at the order of 0.2 sec. The biggest variation in it period is only  $\approx 0.6$  sec. Is very clear now how sensitive the Kalimeris method is in the detection of variations in the period of the system, that with the methods used until now would be undetectable.

Visual	Photoelectric	Photographic	CCD	Total
46	45	5	11	107

Table 3.3: ER Ori Times of Minima Characteristics

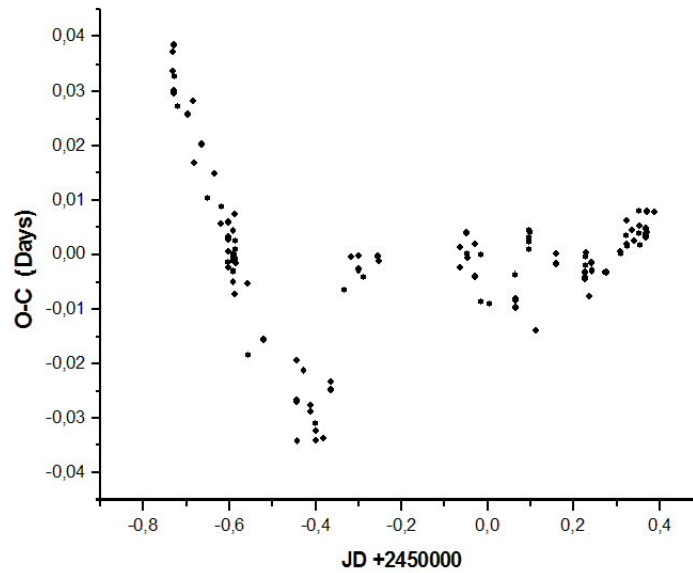


Figure 3.3: The O-C Diagram of ER Ori.

ER-Ori as it finally seems it has a periodic behaviour. In the time span that there is observations, it seems that the period of ER-Ori to modulated by two periodic terms. The first one causes the variations of 0.2 sec. The second one is responsible for the parabolic structure that the diagram has.

The variation of the 0.6 sec is possible caused by a third mechanism that could be not a periodic one. Of course to short this thing out more observations are needed for at least a few decades.

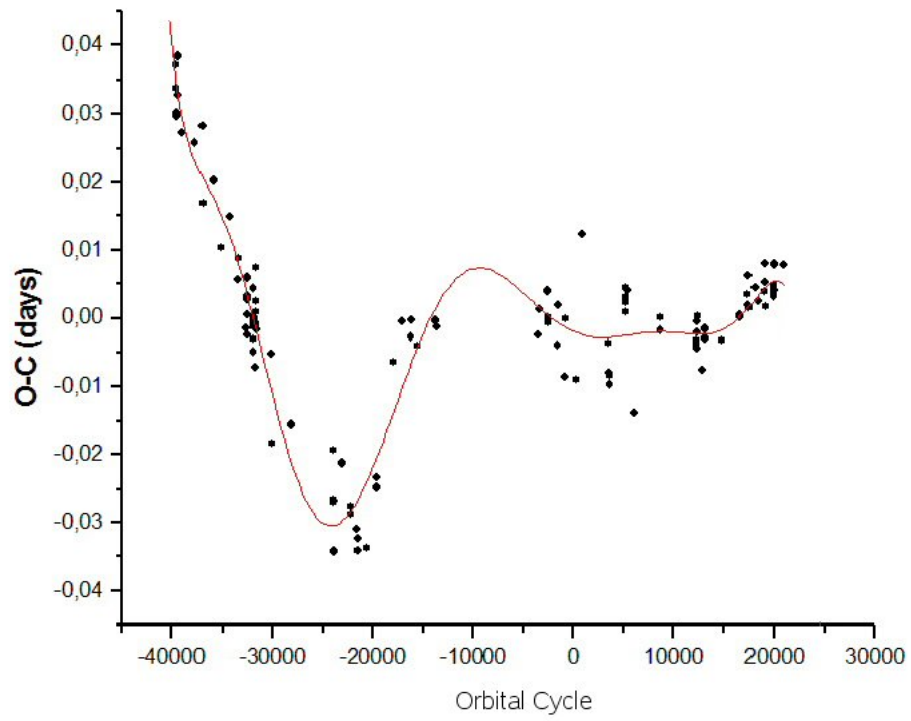


Figure 3.4: The O-C Diagram of ER Ori and the non-Linear Fitting.

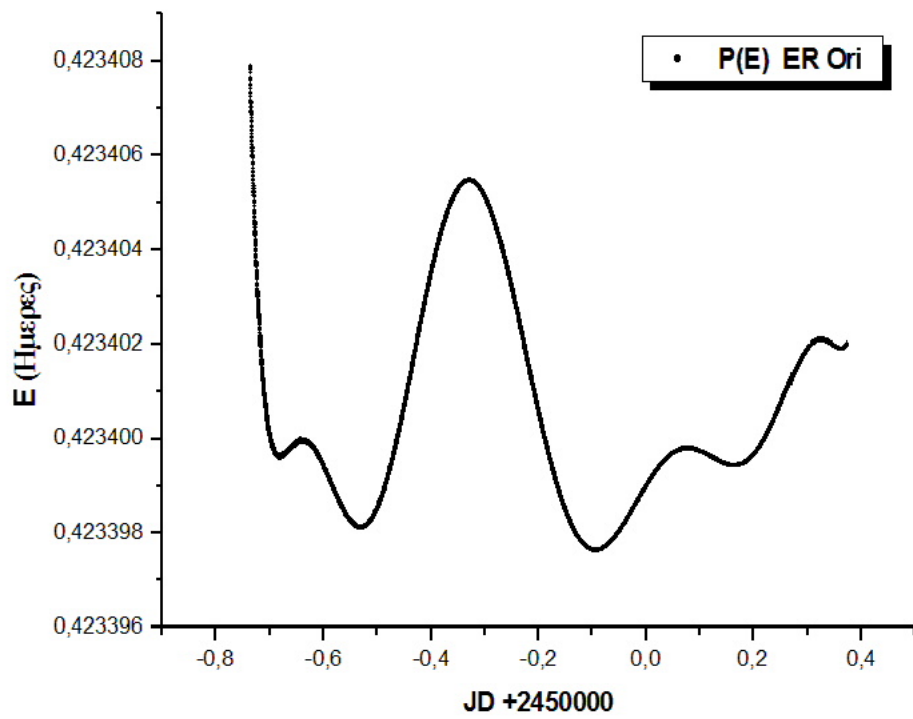


Figure 3.5: The  $P(E)$  Function of ER Ori.

# Chapter 4

## Results and Conclusions

### 4.1 Future Work

Future work possible with this new method, is the analysis of many more contact binary systems so we can have better statistics. This will allow us to find relations between the physical parameters of contact binary systems and to understand the physics of these systems. Until now the method of analysis was wrong, so many things that was supposed true about contact binaries, now possible they will be wrong and need revising.

With the Kalimeris method, from the moment that is selfconsistent and does follow all the physics of contact binaries, it is sure that it can lead us to the right structure theorys not only for contact binaries but for all double systems that O-C diagrams can be constructed. Moreover because of the high sensitivity of the method to subtle changes in the period of a double system, it can give us candidates for a third body with a mass compareable to earth.

So it is an excellent method to discover new planets in double systemms. The only point that needs our attention is that it can give us only candidates. So other methods should be used to verify the existence of another planet in a binary system.

## **Part II**

**Fourier and Wavelet Analysis of SS433 High Speed Photometry**

## Chapter 1

# Introduction to Microquasars and SS433

*“Chaos, Order and Hidden Meanings ...”*

What is a microquasar and why it has this name? Many people when they here the term microquasar they think of an extragalactic object called just quasar. They simply think that it's just a category of quasars, but the truth is far from this.

Actually microquasars are binary systems that lie well within our galaxy. They have an accretion disc that is warmed up by falling mass acquired by a hot companion star. So they have very common characteristics in their spectrum both quasars and microquasars, and that's why they have a common name. A microquasar is a small version of a quasar, but only in the observed characteristics and not in their real physical background. In figure 1.1 their differences are shown.

The main similarities but at the same time their main differences as well is their black hole. In quasars is very big in the order of a few thousand solar masses in comparison to microquasars that they have a black hole of only few solar masses. This fact has an immediate impact on the temperatures and the size of the jets they have, with quasars naturally have everything much bigger. With quasars we have jets that extend in million light years in comparison to microquasars that extend in only a few light years. In figure 1.2 there is a list of a few known microquasars in our galaxy.

It is clear that the name microquasar is properly selected to clarify the analogy with quasars and to point that the knowledge of the physics of microquasars can easily be applied to quasars. After all both type of objects have fundamentally the same physics of astrophysical jets.

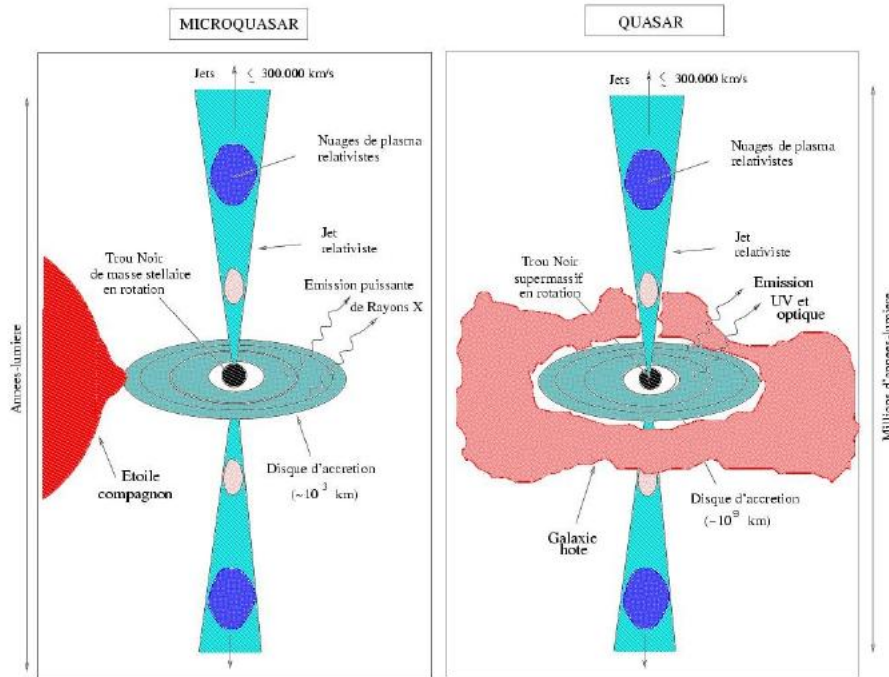


Figure 1.1: Differences of microquasars and quasars

## 1.1 The SS433 Microquasar

SS433 or else V1343 Aql is famous as the first relativistic jet source in the galaxy and is considered to be a prototype microquasar. It is essentially a binary system of a compact object, probably a black hole, and probably an A4 supergiant donor star. It demonstrates precessing jets and a supercritical accretion disc around the black hole. SS433 is also in the center of the supernova remnant (SNR) W50. It is a highly variable system and shows different types of periodicities:

**Precessional** ( $P_{prec} = 162.5^d$ ) which is observed by periodical Doppler shifts of H, He, I, Fe and other optical and X-ray emission lines also is clearly visible in optical and X-ray light curves. (A. M. Cherepashchuk et al., 2004)

**Orbital** ( $P_{orb} = 13.082^d$ ) which is observed in optical, radio and X-ray bands. The shape of the optical light curve strongly depends on the precessional phase but its period remains stable for over 30 years. (A. M. Cherepashchuk et al., 2004)

**Nutational** ( $P_{nut} = 6.28^d$ ) which is observed as a periodic deviation from the precessional Doppler motion of emission lines and can also be recovered from photometric data. Nutational radial velocity variations are delayed from the nutational photometric variations by 0.6 days. This delay corresponds to the travel time from the accretion disc centre to the region where the moving optical emission lines, downstream the relativistic jets are formed. This region is located at  $l \approx 10^{14} - 10^{15}$  cm away from the disc center. This periodicity remains stable for at least 16 years. (A. M. Cherepashchuk et al., 2004) The fact that makes the SS433 so specific is that its anti parallel

Object Name	RA (J2000.0)	Dec. (J2000.0)	Type
<b>LS I 61°303 (V615 Cas)</b>	02 <sup>h</sup> 40 <sup>m</sup> 31.7 <sup>s</sup>	+61° 13' 46"	HMXB
<b>XTE J0421+560 (CI Cam)</b>	04 <sup>h</sup> 19 <sup>m</sup> 42.2 <sup>s</sup>	+55° 59' 58"	HMXB
<b>XTE J1118+480 (KV UMa)</b>	11 <sup>h</sup> 18 <sup>m</sup> 10.9 <sup>s</sup>	+48° 02' 13"	LMXB
Circinus X-1 (BR Cir)	15 <sup>h</sup> 20 <sup>m</sup> 40.9 <sup>s</sup>	-57° 10' 01"	LMXB
XTE J1550-564 (V381 Nor)	15 <sup>h</sup> 50 <sup>m</sup> 58.7 <sup>s</sup>	-56° 28' 36"	LMXB
<i>Scorpius X-1 (V818 Sco)</i>	16 <sup>h</sup> 19 <sup>m</sup> 55.1 <sup>s</sup>	-15° 31' 15"	LMXB
GRS J1655-40 (V1033 Sco)	16 <sup>h</sup> 54 <sup>m</sup> 00.1 <sup>s</sup>	-39° 50' 45"	LMXB
GX 339-4 (V821 Ara)	17 <sup>h</sup> 02 <sup>m</sup> 49.5 <sup>s</sup>	-48° 47' 23"	LMXB
XTE J1748-288	17 <sup>h</sup> 48 <sup>m</sup> 05.1 <sup>s</sup>	-28° 28' 26"	LMXB
1E1740.7-2942 (Great Annihilator)	17 <sup>h</sup> 44 <sup>m</sup> 02.7 <sup>s</sup>	-29° 43' 25"	LMXB
GRS 1758-258	18 <sup>h</sup> 01 <sup>m</sup> 12.3 <sup>s</sup>	-25° 44' 36"	LMXB
V* V4641 Sgr (XTE J1819-254)	18 <sup>h</sup> 19 <sup>m</sup> 21.6 <sup>s</sup>	-25° 24' 25"	LMXB
<i>LS 5039</i>	18 <sup>h</sup> 26 <sup>m</sup> 15.0 <sup>s</sup>	-14° 50' 54"	HMXB
<b>SS 433 (V1343 Aql)</b>	19 <sup>h</sup> 11 <sup>m</sup> 49.6 <sup>s</sup>	+04° 58' 58"	HMXB
<b>GRS 1915+105 (V1487 Aql)</b>	19 <sup>h</sup> 15 <sup>m</sup> 11.5 <sup>s</sup>	+10° 56' 44"	LMXB
<b>Cygnus X-1 (V1357 Cyg)</b>	19 <sup>h</sup> 58 <sup>m</sup> 21.7 <sup>s</sup>	+35° 12' 06"	HMXB
<b>Cygnus X-3 (V1521 Cyg)</b>	20 <sup>h</sup> 32 <sup>m</sup> 26.6 <sup>s</sup>	+40° 57' 09"	HMXB

Figure 1.2: A Small list of Known Microquasars

beams originate from the source position at relativistic velocities. The reason that this object was very popular in the beginning of 1980 was based on the belief that from the study of the astrophysical jets of a galactic object it would be possible to have a complete comprehension and application of the acquired knowledge to the extragalactic astrophysical jets.

## 1.2 The Kinematic Model

Before we reach and specify the details concerning the study of the compact radio structure of SS433, it is necessary to explain the simple pattern of the suggested model, which describe the complete kinetic properties of the source. This kinematic model represent the most useful tool firstly to comprehend and secondly to precisely figure the motion of the emitted jets. As a result the measurable (observable) quantities such as the precession period, the magnitude and others can be precisely estimated. Not only the optical but also the infrared spectrum of SS433 show two sets of strong shifted emission lines due to the Doppler effect. These systems appear to have random changes in their wavelength. The maximum measurable radial velocity is at the order of a magnitude of  $+50.000Km/sec$  and  $30.000Km/sec$ .

In the model which we deal with, is considered the assumption that the two Doppler shifted lines concern the anti-parallel orientated beams of particles. The observed periodic change in radial velocity is explained by taking into account the revolution around the ejection axis. Due to the fact that these beams are anti-parallel, the first one moves far away from the observer (red shifted spectral lines) while the other approach the observer (blue shifted spectral lines). This model was proposed by Fabian and Rees (1979) and by Milgrom (1979). In addition, for achieving accordance

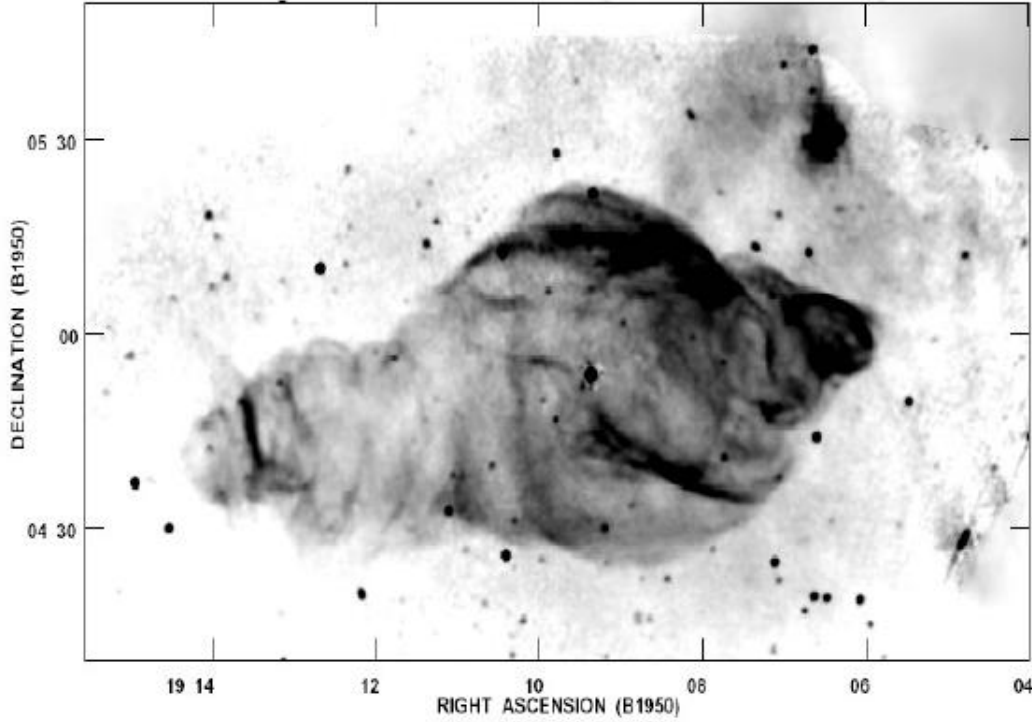


Figure 1.3: The supernova remnant W50 and SS433

with measurable radial velocity we have to accept that these beams have almost a relativistic velocity of about  $0.26c$ . In its simplest form, this model is completely described by seven parameters. These parameters are :

- **i** The angle between the observation direction and the axis of the cone due to the precession motion. It is defined that.
- $\theta$  The mean angular width of the cone which is bounded by the particle beams.
- $\psi$  The position of the angle of the cone axis as it is projected on the sky plane.
- **s** The parameter which determines the direction of the beams precession. We use  $s = 1$  for right-handed rotation and  $s = -1$  for left-handed rotation.
- **u** The velocity of the particles into the beams. We use the relativistic expression.
- **P** The precession period.
- $t_0$  The time in which the phase of the precession  $\psi(t)$  is zero.

At this time, we will present a more detailed analysis, in which our final purpose is the presentation of a three dimensional model of the jets motion. We consider the axis  $z'$ , around of which



$$u_z = S_{jet} \bar{u} [\sin i \cos \Psi - \cos i \sin \Psi \cos \Omega(t_0 - t_{ref})] \quad (1.2)$$

In order the description to be possible of normal motions, it will be necessary the axis  $y$  and  $z$  to be rotated at an angle of  $\chi$ , in order for the new  $y$  axis be directed northwards, while the new  $z$  axis to be directed eastward as it appears in scheme B. At this scheme the new  $z$  axis is renamed  $\Delta\alpha$  and the new  $y$  axis is renamed  $\Delta\delta$ . Both the precise definition of the jets position and the other geometrical parameters are depicted at scheme B. From the projection of the vector  $u$  at the axis  $\Delta\alpha$  and  $\Delta\delta$  we take :

$$\begin{aligned} u_\alpha &= (\sin x)u_y + (\cos x)u_z \\ u_\delta &= (\cos x)u_y + (\sin x)u_z \end{aligned} \quad (1.3)$$

We consider  $t_{eject}$  as the time in which a specific couple of the SS433 jet parts is ejected from the central object. The observable normal motions of these jet parts in a ulterior time  $t_0$  are described by the following expressions :

$$\mu_\alpha = \frac{u_\alpha(t_0 - t_{eject}) / \cos \delta}{d(1 - u_x/c)} \quad (1.4)$$

and

$$\mu_\delta = \frac{u_\delta(t_0 - t_{eject})}{d(1 - u_x/c)} \quad (1.5)$$

$c$  is the velocity of light,  $d$  is the distance of the object, while the factor which is appeared at the denominators, compensate the finite time period of the observable radiations voyage, as it crosses the source. Due to this effect (this is a special relativity consequence) the nearest side of a twin jet, is appeared as it was at a time after  $t_0$  while the distant as it was at a time earlier than  $t_0$ . The time period of a specific observation  $t$ , is correlated with  $t_0$  according to the light voyage time between SS433 and the observer.

Studying the above equations, we see the presence of the following parameters  $S_{jet}$ ,  $S_{rot}$ ,  $\Psi$ ,  $i$ ,  $\chi$ ,  $P$ ,  $t_{ref}$ ,  $u/d$ ,  $u$ , which are the same for all stages of the object, in a model of constant velocity. It is important to say that, these equations describe the motion of every particle which be ejected by from a source, and provide accurate results even in relativistic velocities. Therefore these equations, can be used not only in case of SS433, but also at quasar's jet and also in radio galaxies.

### 1.3 The Jet's of SS433 Microquasar

It still remains fairly uncertain the mechanism that describes the accelerarating and well defined jets. In general the hypothesis that either rotation or adding mass through the accretion disc in a compact star, could be possible provide the big amount of energy that is required. Any model that is trying to explain the jet's is restricted by these well observed parameters :

- The jet's must have a stable velocity of  $0.26c$ . This velocity must be aquired in a time of 100 sec.

- Well difend jets tha have an angular width of less than  $4^\circ$ .
- The jet's are two-sided and anti-parallel and they have a precession with a period of almost 162 days.

## 1.4 Flaring Events

SS433 as it is said above it is observed since the 80's. Already in 1989 it was observed five flaring events from Vermeulen. A hypothesis was made, that the spectrum of SS433 was a combination of a quiet one and the spectrus of the flares evolving indepenately.

Before an actual event of a flare it is observed a small dip in the flux density in radiowaves as well as in other bands. This dip probably some kind of matter that is optically thick that is ejected from SS433 during a flaring event. One other reason for the flux dip could be matter optically thick ejected in a shell form near the binary system obscuring the quiescent radio emission as well as the flux in the optical band. Such a dip and flare probably explains the data acquired in August 2005 for this diploma thesis. I will talk again about the observed flare later on. Flares in SS433 have a

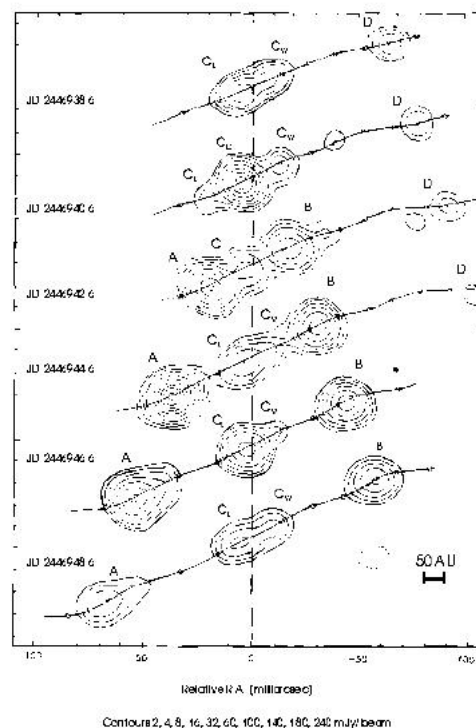


Figure 1.5: Flaring Events of SS433

typical life span of five days, they don't have any particular dependence with frequency but there is a trend to last longer in lower frequencies. One very important thing is that there is two kind of flares in SS433 that can be observed.

Each they have a different way of evolution thus probably they have a different physical creation mechanism, or they have a different place in SS433 that they create. This fact was observed by Vermeulen in 1989 with VLBI. An increase in flux in the region of the core of SS433 was observed followed by repeated flares originating in the jet's of the object. This exactly is shown in figure 1.5.

All this observations of course reinforce the belief about the chaotic character of SS433. This chaos is confirmed by my observations as well, that follows.

## Chapter 2

# Observations And Data Analysis of SS433

### 2.1 High Speed Photometry of SS433

We observed SS433 in  $V$  and  $R$  filters in 2004 and 2005. In 2004 the observations were made in  $V$  for the period of 26 through 31 August and in 2005 in  $R$  from 01 to 10 August. The exposure times were 5 and 10sec. We used the 516x516 CCD camera  $SI - 502$  mounted on the 1.2m telescope of NOA, located at Kryonerion, Mt. Killini, Greece at an altitude of 1000m. The telescope is shown at figure 2.1.

#### 2.1.1 Analysis of Observational Data

For the analysis of the observed data a consistent method was needed that would give us results free of noise as possible. The method used has three main parts.

**Optimal Differential Photometry of SS433** In this first step i had the choice of either using all-sky photometry or just plain differential photometry.

The data were reduced using standard Starlink scripts. In the reduction process we used bias dark and flat-field corrections. Differential photometry was obtained with the automated optimal photometry package AUTOPHOTOM, for SS433 and with comparison the star

- *GSC 00471-01564* ( $RA : 19h11m47.6s$   $Dec : +05d00m36.1s$ )

Then fluxes were extracted with their corresponding errors. In order to be sure that any periodicities found were not produced by changes in the comparison star, additional photometry of the comparison was performed with two other random stars in the field. These stars were :

- *C1* ( $RA : 19h11m49.9s$   $Dec : +05d00m05.5s$ )

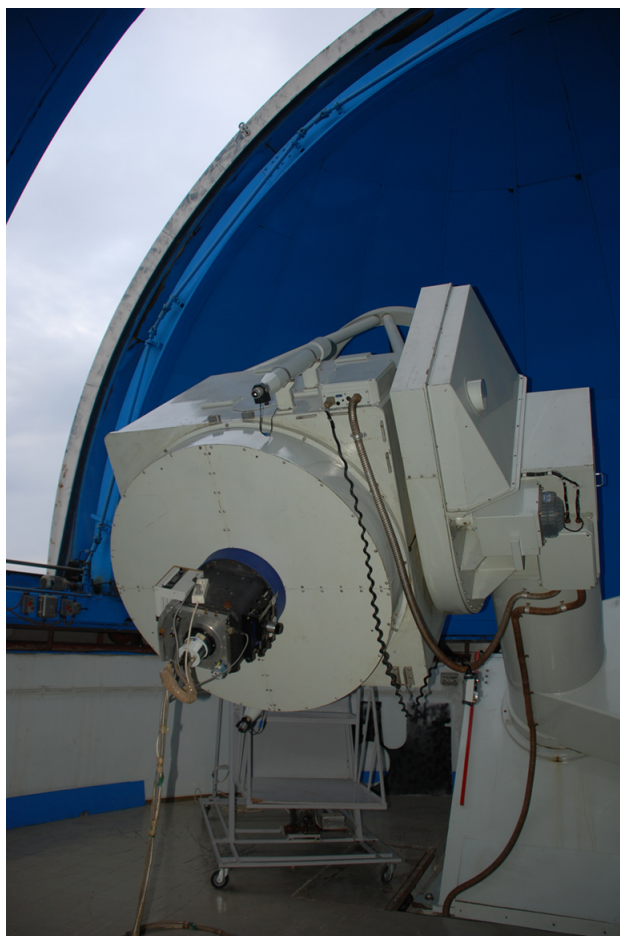


Figure 2.1: The 1.2m Telescope at Kryoneri Corinth

- *C2 (RA : 19h11m47.7s Dec : +05d00m04.0s)*

In all light curves presented here photometry of the two comparison stars (C1 and C2) is included in each diagram for every night. For artistic reasons a constant was subtracted from their fluxes of the comparison stars. The upper curve depicts C1 and the lower one C2.

**Fourier Analysis of the Light Curves** We used the Lomb - Scargle method to compute the power spectra of all the data with the PERIOD package. To avoid any mistakes in the interpretation of the periods the corresponding window function was also used.

**Wavelet Analysis of the Light Curves** In this step, the data was analyzed with the Wavelet method. The software used, was from H. Letho and for his help i thank him very much.

Below i will analyze a little more about the fourier and wavelet algorithm.

## 2.2 Methods of Time-series Analysis

Time series analysis is the application of mathematical and statistical tests to time varying data, both to quantify the variation itself and to learn something about the behavior of the system. Ultimately, the goal of time-series analysis is to gain some physical understanding of the system under observation: what makes the system time-variable? what makes the system similar to or different from other systems? is the system predictable? and can we place reliable limits on the behavior of the system? Clearly, simple forms of time-series analysis were known in ancient times, since many ancient civilizations made accurate predictions of various cyclical celestial phenomena.

The birth of modern time-series analysis dates to the early 19th century, with Joseph Fourier's description of the Fourier series, and later, the Fourier transform. (Carl Friedrich Gauss first derived the Fast Fourier Transform around 1805, before Fourier published his work, but Gauss did not publish his results.) The greatest advances in time-series analysis coincided with the development of computing machines and the digital computer in the mid-20th century. The digital computer made possible the statistical analysis of large amounts of data in much less time than would be possible by human calculators.

Along with this came the development of more efficient algorithms for time-series analysis (like the rediscovery of Gauss Fast Fourier Transform by Danielson and Lanczos in the 1940s), and the development of new ideas such as wavelet analysis and chaos theory. Today, time-series analysis is regularly applied to a wide variety of problems in the real world, from radio and telecommunications engineering to financial forecasting.

The practical problems in the analysis of time series concern :

- The detection of a signal against noise.
- The estimation of the parameters characterizing the signal, and
- The presentation of the results.

But let's describe better the methods used in this diploma.

### 2.2.1 The Fourier Algorithm

Fourier analysis is the technique of using an infinite number of sine and cosine functions with different periods, amplitudes, and phases to represent a given set of numerical data or analytic function. In so doing, you can estimate the period (or periods) of variability by determining which of these functions are statistically significant. The amplitudes (and phases) of these components are determined with a Fourier transform.

If we have a set of time-varying data, given by  $x(t)$ , then the Fourier transform,  $F(\nu)$ , is given by the integral :

$$F(\nu) = \int_{-\infty}^{+\infty} x(t)e^{-i2\pi\nu t} dt \quad (2.1)$$

where  $\nu$  is the frequency, defined as  $\nu = 1/P$ , *i*.

If a set of data,  $\chi(t)$ , contains a coherent signal at some frequency,  $\nu'$ , then the value of the Fourier transform,  $F(\nu)$ , should reach a local maximum at  $\nu'$ . If the data contain several signals with different frequencies, then  $F(\nu)$  should have local maxima at each, with the global maximum at the frequency having the largest amplitude. The Fourier transform is an extremely powerful yet elegant technique that is used in many areas of mathematical analysis and the physical sciences. However, as one might expect, its power is finite, limited by the amount and quality of data that are transformed. The data place several limits on the usefulness of the transform, including the maximum and minimum periods testable, the accuracy of the period determination, and the minimum statistically significant amplitude that can be found.

As an example, consider the following case: you have a data set spanning 5000 days, with an even sampling rate of 10 data points per day (or one data point every 2.4 hours). The maximum period detectable in this case is 5000 days, since the data should cover one complete cycle. However, this detection would be very unreliable since without additional data you have no idea whether the variation detected was truly periodic or simply a short-term fluctuation that merely looks like a 5000-day period. A more reliable limit is 2500 days, since you could detect two complete cycles at that period within the data set. The span of the data set also determines the resolution of the Fourier transform, which is the precision to which the frequency (or period) may be determined. The sampling theorem defines the set of frequencies that may be measured by a given data set, and the separation between two adjacent frequencies defines the resolution of the transform. The resolution is defined by :

$$d\nu = 1/N\Delta \quad (2.2)$$

where  $N$  is the total number of samples (50000), and  $\Delta$  is the space between the samples (0.1 day). In terms of frequency, the resolution is simply the inverse of the span of the data; if the data span 5000 days, the frequency resolution is  $1/5000d^1$ . The data set with the longer span clearly provides a much more precise determination of the period than the shorter data set. This makes clear the need for long sets of data, particularly when studying long period variables. at maximum and minimum once each cycle. This is known as the Nyquist frequency. The Nyquist frequency is important not only because it defines the highest frequency (and shortest period) detectable with a given dataset, but also because it defines the maximum sampling rate you need in order to fully describe variations up to the maximum frequency.

In certain circumstances, it is possible to detect frequencies higher than the sampling rate. The transform will suffer from aliasing, in which several different peaks appear in the transform, along with the real one. The alias peaks are separated from the true frequency by integer multiples of the sampling frequency, such that the transform will look like a picket fence when plotted. In the case of regular sampling, the alias peaks will have equal statistical significance to the real peak, and it is therefore impossible to tell which peak in the power spectrum is the correct one. In the case of uneven sampling, you will still have aliasing, but the strengths of the alias peaks will generally be

lower than that of the dominant one.

### 2.2.2 Noise And Real Periodicities

One major consideration in Fourier analysis is noise both the intrinsic noise of photometric observations, and measurement errors of the data. Noise is always present in a given signal regardless of the quality of measuring devices. From a physical standpoint, the precision of photometry is limited by Poisson statistics the more photons arrive at the detector, the more precisely one is able to measure the signal. The noise level (defined as the square root of the number of photons) decreases but never vanishes as the number of photons increases. From an observational standpoint, measurements of a given signal will always contain some error. For example, visual observations are rarely accurate to more than 0.1 magnitude for an individual observer, while systematic differences between observers can amount to 0.2 to 0.3 magnitude or more. CCD and photoelectric measurements typically have smaller (but still significant) errors caused by sky background and instrumental effects. Fourier analysis of a given set of data assumes that everything contained within a given data set is a signal. Thus noise will appear in the Fourier spectrum at some level defined by the strength of the true periodic modulations relative to the background noise. Measurement of this noise level is an important part of Fourier analysis, as it allows you to determine the reliability of your results.

A final caveat to those using Fourier analysis to detect periods is that discrete methods for analyzing unevenly sampled data will produce spectral artifacts of the sampling of the data, in addition to any signal contained within the data. For example, data taken over a series of nights (with daylight gaps between) will have aliases caused by the 1 cycle/day sampling windows. These alias frequencies are centered on any real signals in the data, offset from the central frequency by integer multiples of 1 cycle/day. The reason for this is that the data sampling produces a window function in the Fourier transform, which is convolved with the Fourier peak of the real signal. The result is the picket fence of frequencies in the Fourier spectrum. In general, one deals with aliasing in the spectrum by assuming the strongest peak observed is the correct frequency, but someone should always use caution when interpreting the Fourier spectra of gappy data.

### 2.2.3 The Wavelet Algorithm

Wavelet analysis and the wavelet transform are relatively recent developments in time-series analysis. The development of the wavelet transform came from the need to analyze signals that were transient and/or non-sinusoidal in nature. The wavelet transform of a set of time-series data,  $x(t)$ , is given by :

$$W(\omega, \tau; x(t)) = \omega^{1/2} \int x(t) f^* (\omega, (t - \tau)) dt \quad (2.3)$$

where  $\omega$  is a test frequency,  $\tau$  is a lag time or a position within the light curve, and the function,  $f$ , is called the mother wavelet, a function which determines how the signal should vary with time, frequency, and position within the light curve. (The  $*$  indicates the complex conjugate of the

function,  $f$ , is used.) The wavelet transform is extremely flexible because the mother wavelet can be nearly any function at all. This means, for example, one can include both a specific waveform (e.g., sinusoid) to search for a periodicity, and a time-varying weighting function (like a sliding window) to study the time-dependence of the signal. In this way, one could study both the frequency spectrum of a given signal, as well as the evolution of that spectrum as a function of time.

However, like more traditional Fourier analysis techniques, the wavelet transform also has limitations. The major limitation, as with Fourier analysis, is that the data set must be long enough and well-sampled enough to adequately measure the periods of interest. If the data only span 1000 days, it would be meaningless to test periods longer than 500 days. Additionally, when the wavelet contains a window function, the data should span a length of time such that the window is meaningful. For example, if the data span 1000 days, the period of interest is 200 days, and the wavelet window covers five cycles, the wavelet analysis will not give meaningful information about the time evolution of the signal nearly all of the data will lie within the window for any chosen value of  $\tau$ .

## 2.3 Thoughts in The Appropriate Method of Analysis

Signals can be classified broadly into deterministic and stochastic signals. A deterministic signal, e.g. a periodic signal, can be predicted for arbitrary spaces of time. For a stochastic signal, no such prediction can be made beyond a certain time interval, called the correlation length  $l_{corr}$ . For any finite time series the classification into these two categories is ambiguous so that methods suitable for both stochastic and periodic signals could be applied to any time series with some success.

Usually processes in the source of the signal (e.g. the nucleus of an active galaxy) and/or observational errors introduce a random component into the series, called noise. The analysis of such series usually aims at removing the noise and fitting a model to the remaining component of the series. Suitable models can be obtained by shifting a known series by some time lag,  $l$ , or by repeating fragments of it with some frequency,  $\nu$ . Accordingly, we are speaking of an analysis in the time and frequency domain. In these domains the correlation length  $l_{corr}$  and oscillation frequency  $\nu_o$ , respectively, have particularly simple meanings. It is transparent that the stochastic signals are analysed more comfortably in the time domain (Wavelet analysis) and periodic signals in the frequency domain (Fourier analysis).

### 2.3.1 Deterministic and Stochastic Signals

As noted above, periodic signals are best analysed in the frequency domain while stochastic signals are usually more profitably analysed in the time domain. The analysis in the time domain often involves the comparison of two different signals while in the frequency domain analyses usually concern only one signal. The expectation value of the covariance function of uncorrelated signals is zero. The expected value of the autocorrelation function of white noise also is zero everywhere except for 1 at zero lag. The expected ACF of a stochastic signal of correlation length  $l$  vanishes

outside a range  $\pm l$  about the lags. The ACF of a deterministic function does not vanish at infinity. In particular the ACF of a function with period  $P$  has the same value,  $P$ . Signals of intermediate or mixed type with an ACF which has several maxima spaced evenly by  $l$  and a correlation length  $L \gg l$  is called a quasiperiodic oscillation. Its power is significantly above the noise in the  $1/l \pm 1/L$  range of frequencies and its correlation length  $L$  is called the coherence length.

As it can be seen from the light curves for SS433, the time series that produces is clearly stochastic. This leads us to the conclusion that the best way to analyze this set of data is the wavelet algorithm.

## Chapter 3

# Introduction of Observational Data

### 3.1 Light Curves of SS433

#### 3.1.1 2004-Data

Here it is presented the light curves of the observations made in 2004.

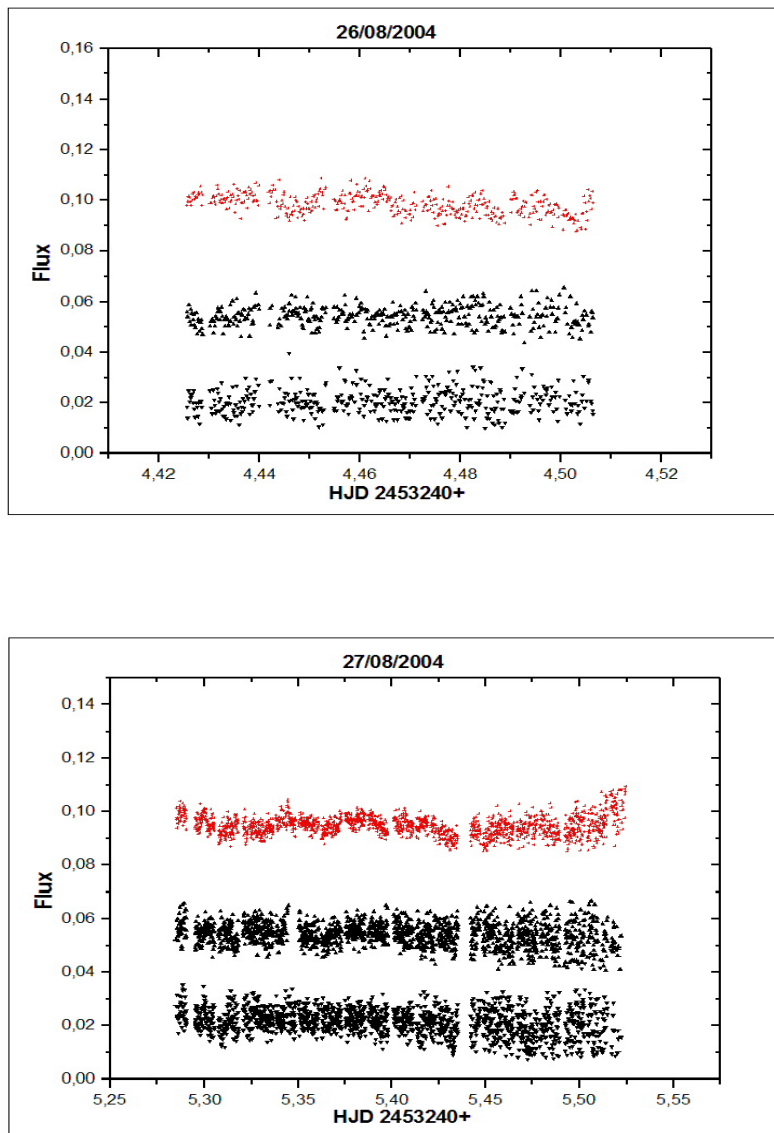


Figure 3.1: Light Curves of 26 and 27 August 2004

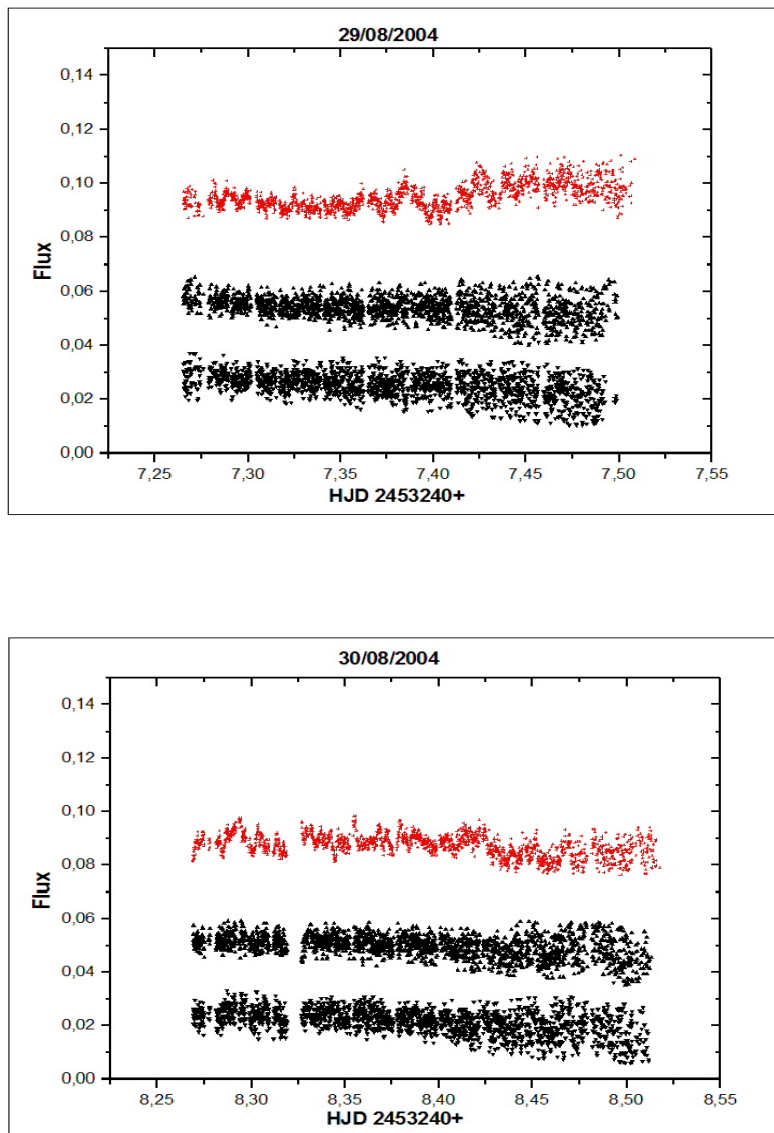


Figure 3.2: Light Curves of 29 and 30 August 2004

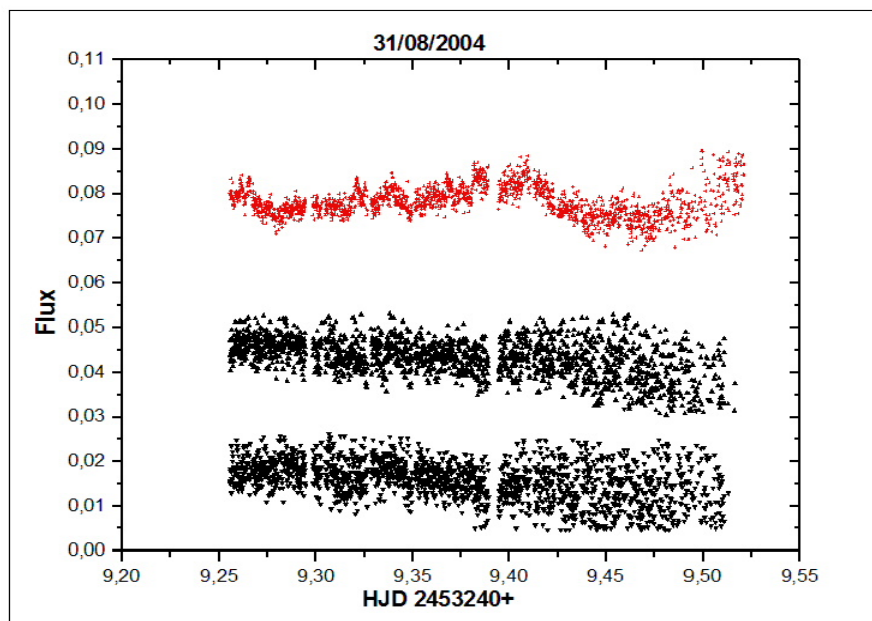


Figure 3.3: Light Curves of 31 August 2004

## 3.1.2 2005-Data

Here it is presented the light curves of the observations made in 2005.

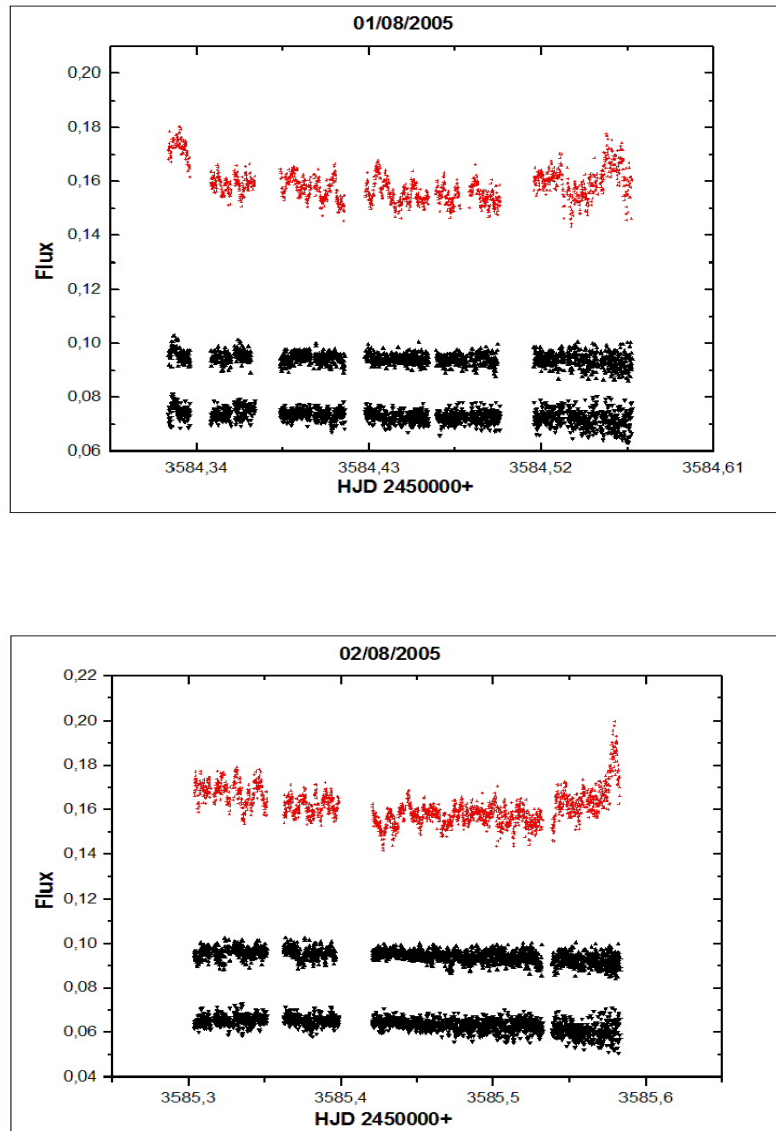


Figure 3.4: Light Curves of 01 and 02 August 2005

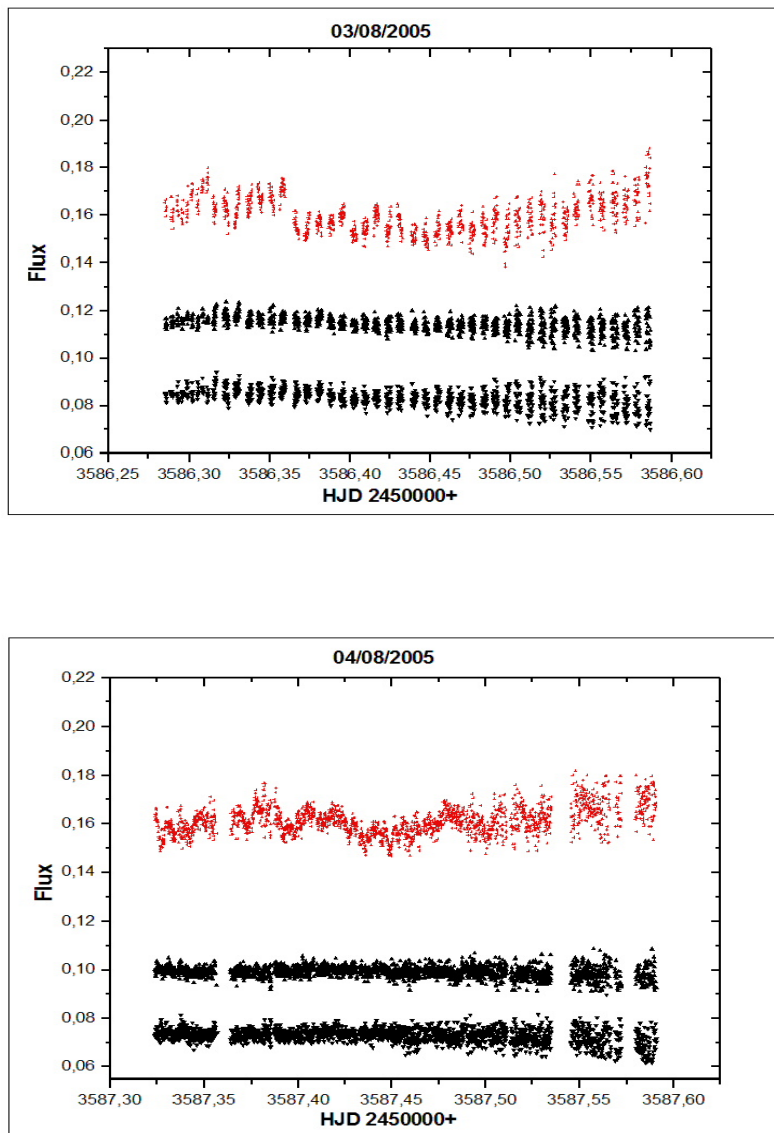


Figure 3.5: Light Curves of 03 and 04 August 2005

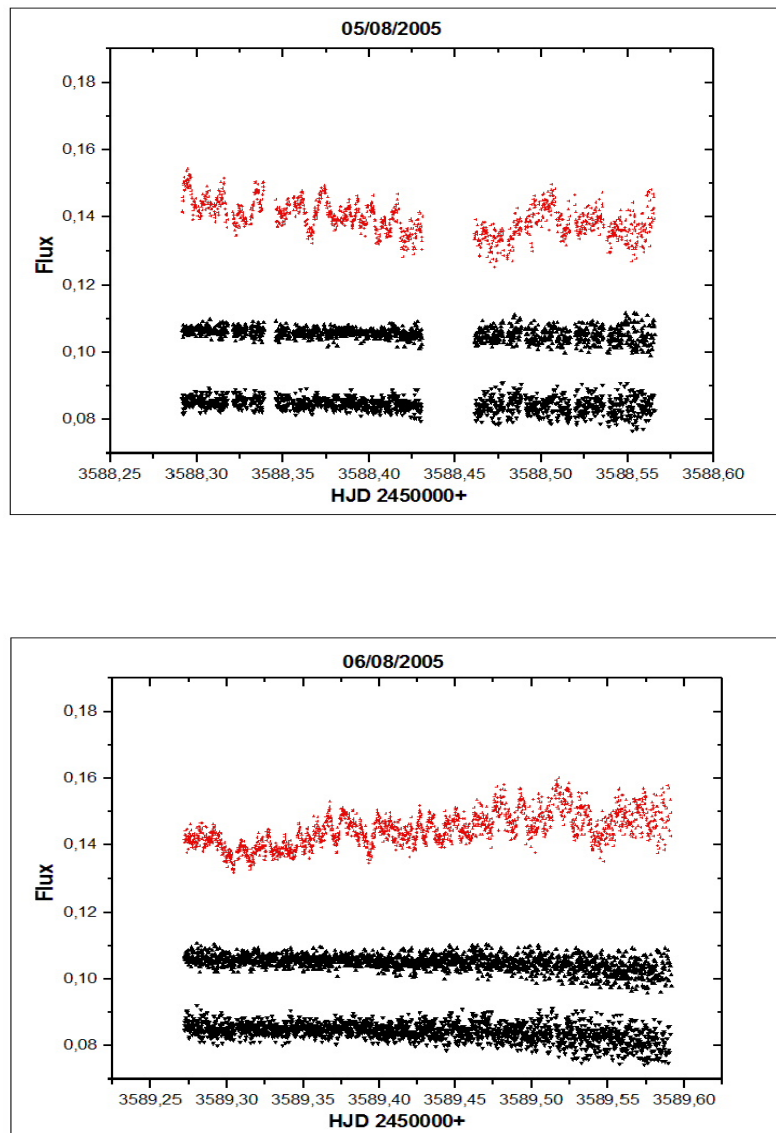


Figure 3.6: Light Curves of 05 and 06 August 2005

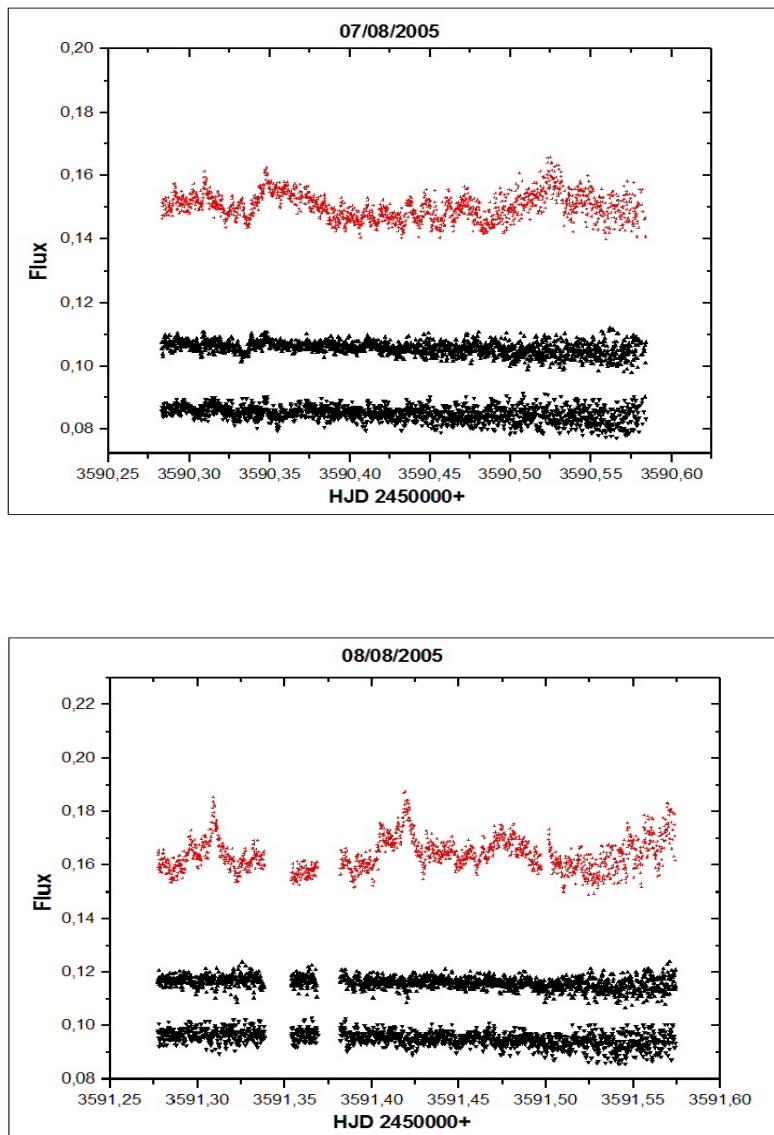


Figure 3.7: Light Curves of 07 and 08 August 2005

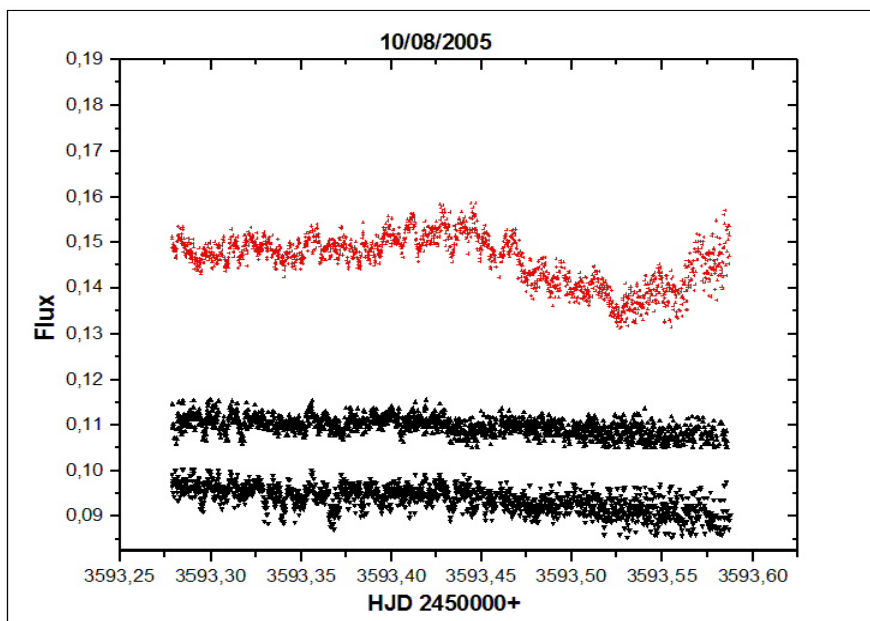


Figure 3.8: Light Curves of 10 August 2005

## **3.2 Fourier Analysis**

### **3.2.1 2004-Data**

Here it is presented the fourier analysis of the light curves, for the 2004 data.

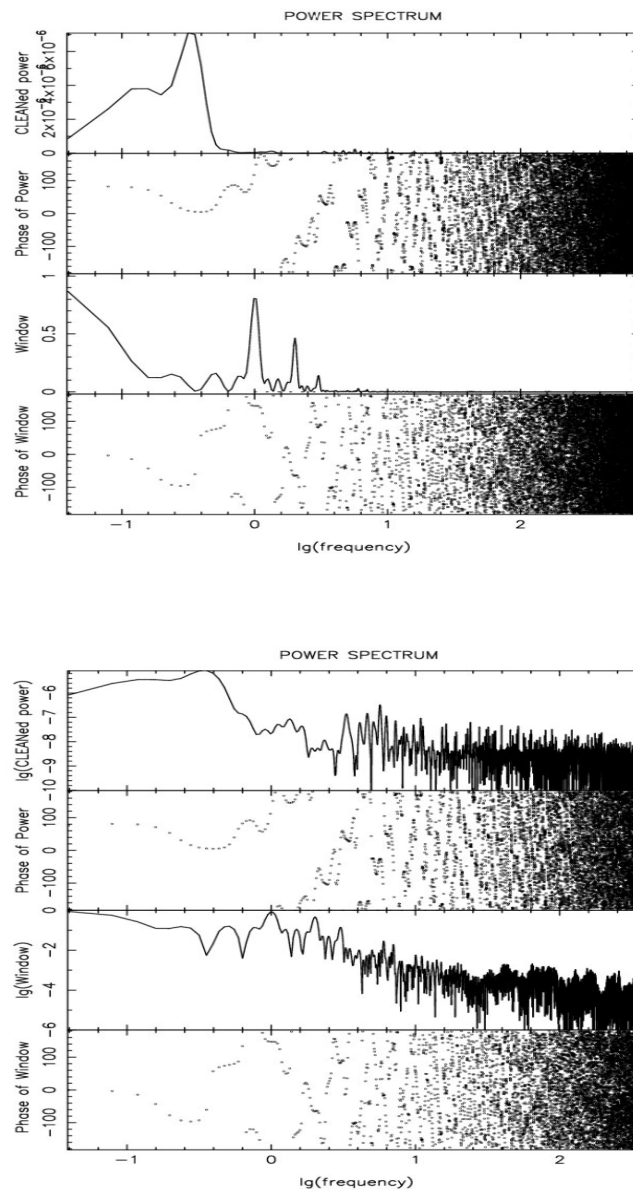


Figure 3.9: Fourier Analysis of the year 2004 Data

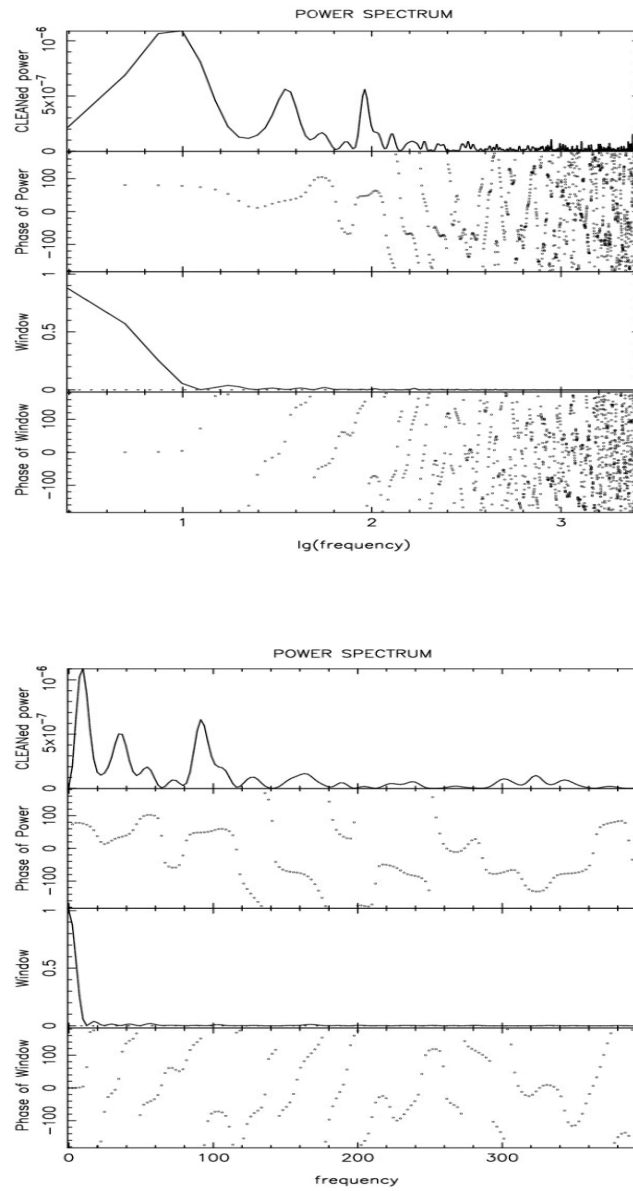


Figure 3.10: Fourier Analysis of 26 August 2004

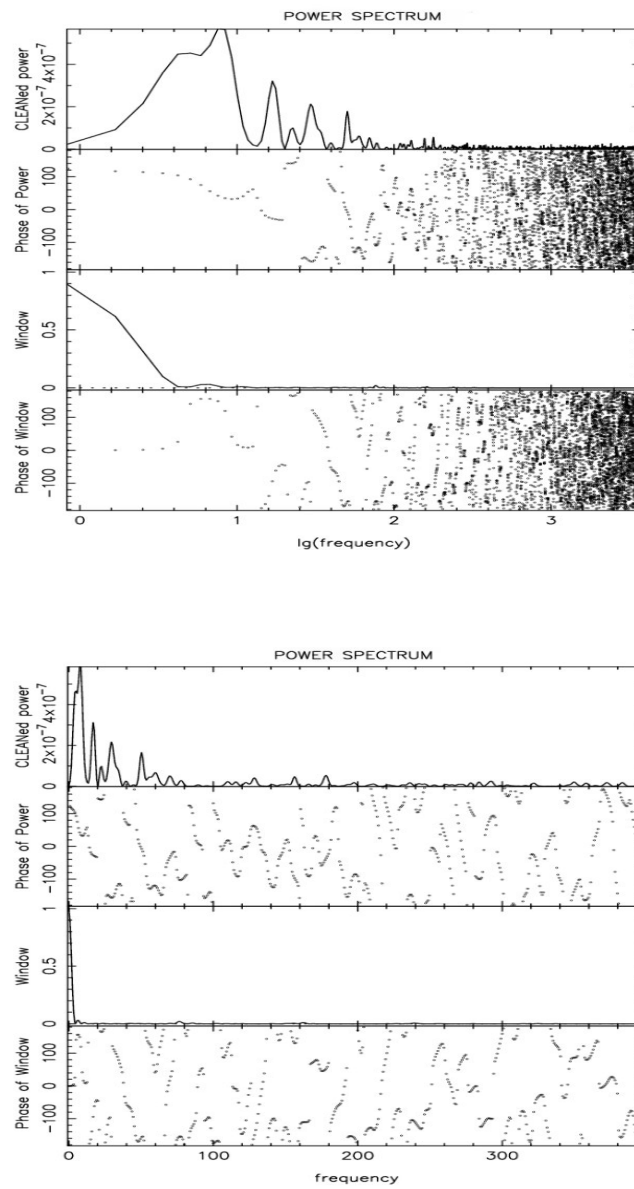


Figure 3.11: Fourier Analysis of 27 August 2004

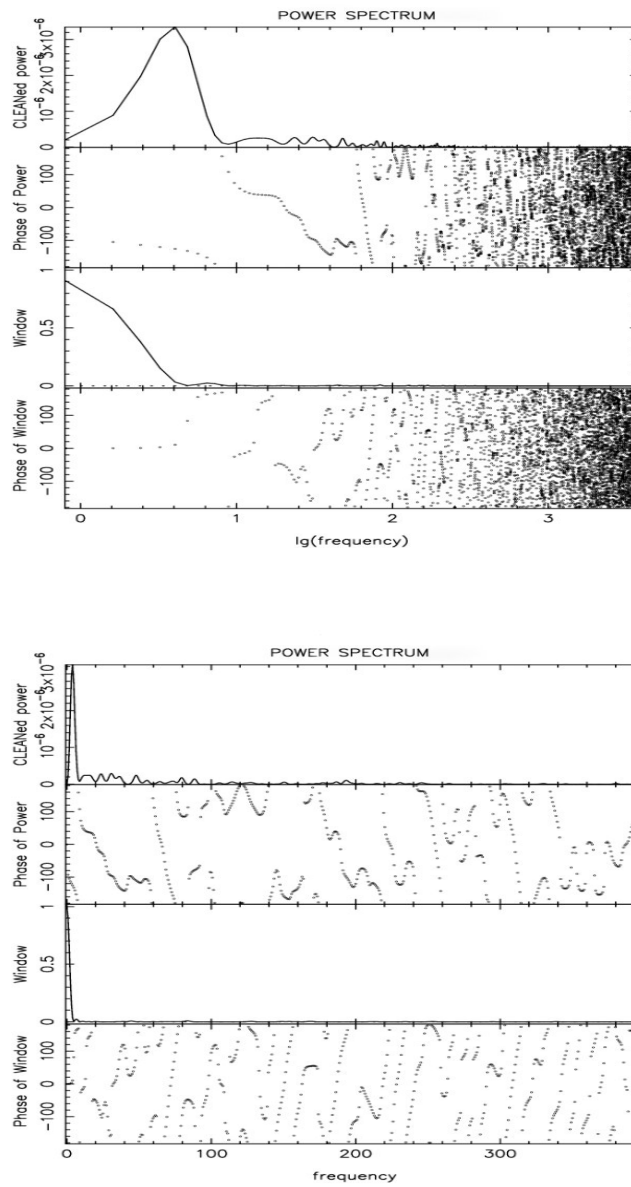


Figure 3.12: Fourier Analysis of 29 August 2004

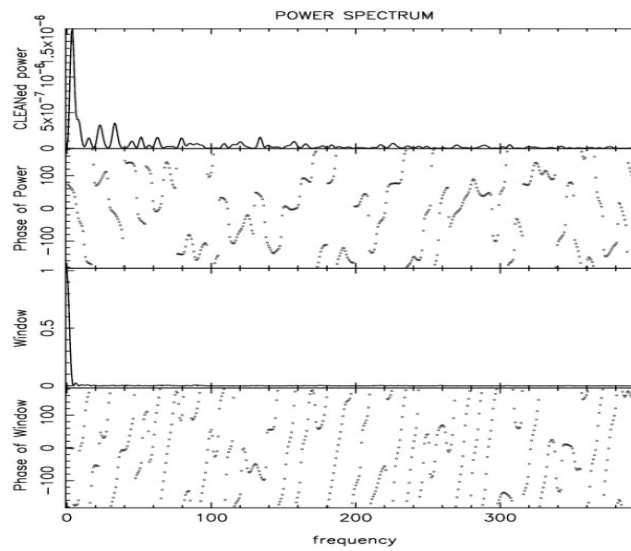
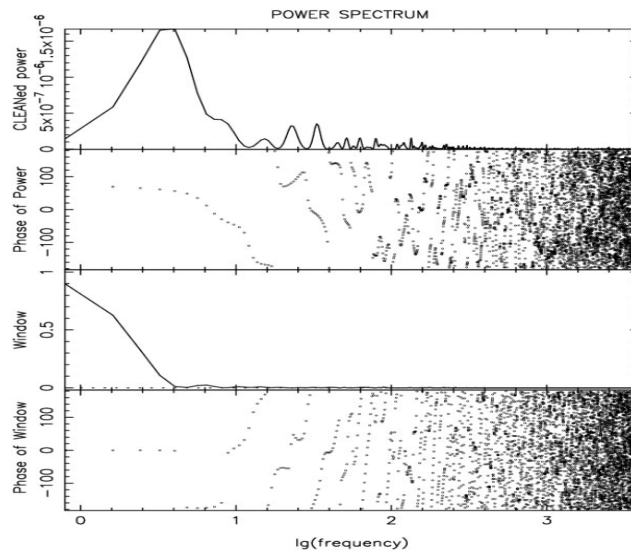


Figure 3.13: Fourier Analysis of 30 August 2004

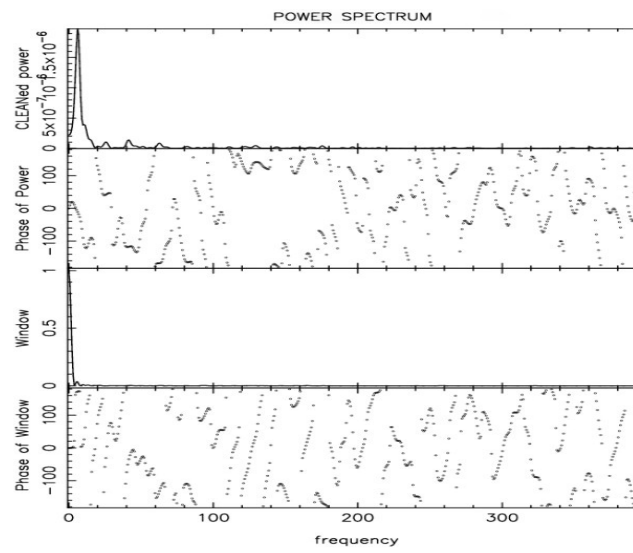
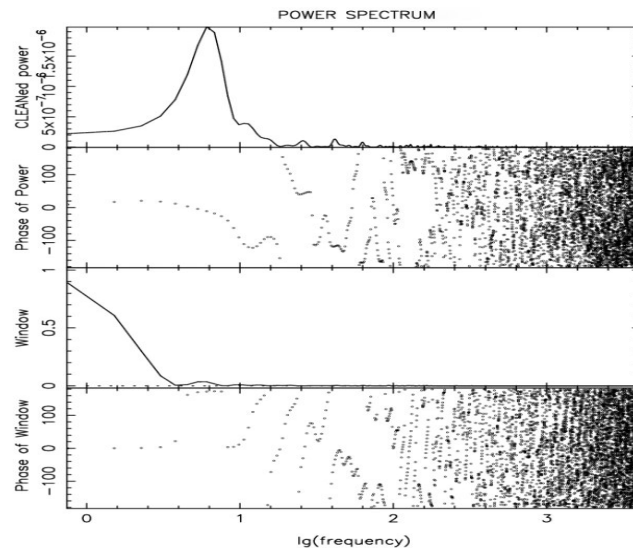


Figure 3.14: Fourier Analysis of 31 August 2004

## 3.2.2 2005-Data

Here it is presented the fourier analysis of the light curves for the 2005 data

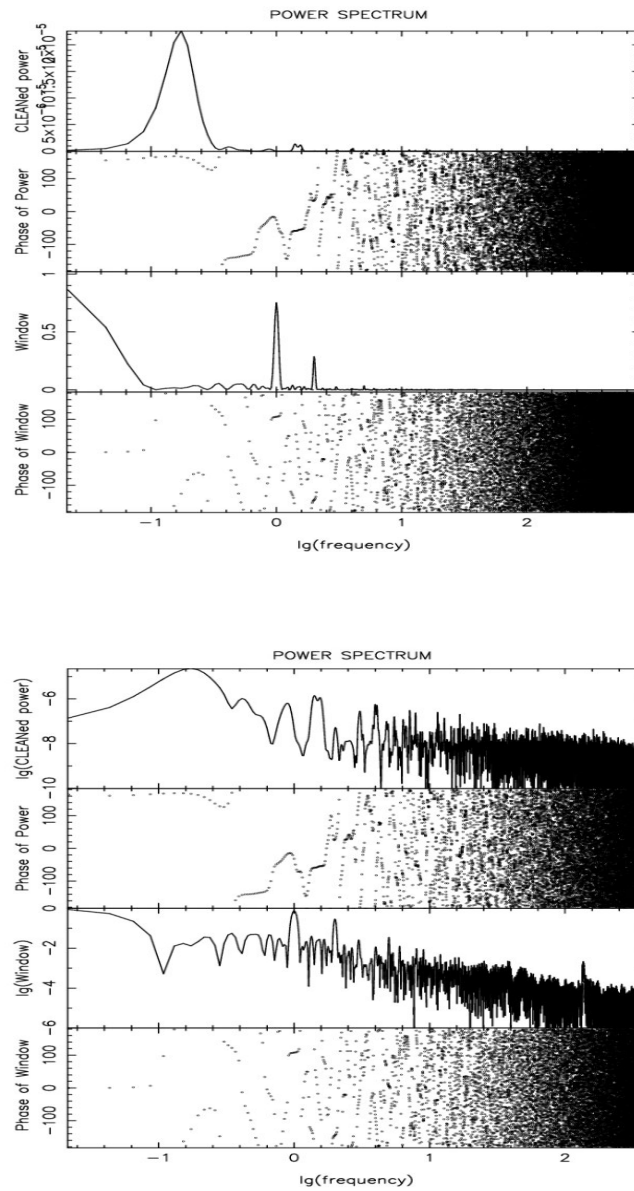


Figure 3.15: Fourier Analysis of the year 2005 Data

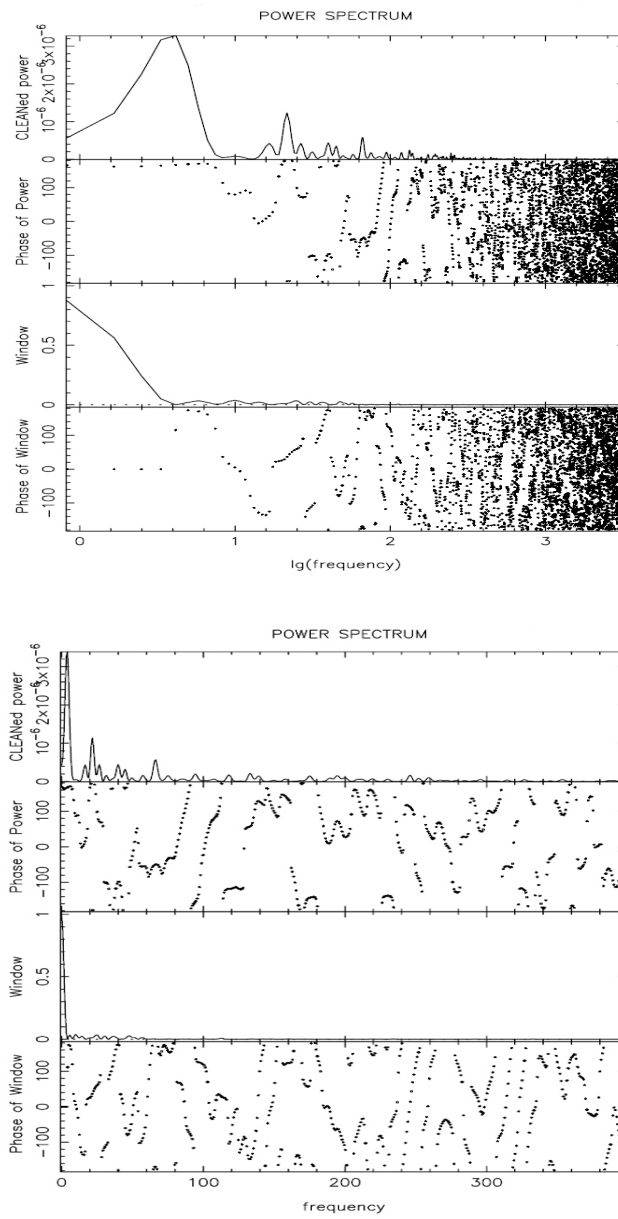


Figure 3.16: Fourier Analysis of 01 August 2005

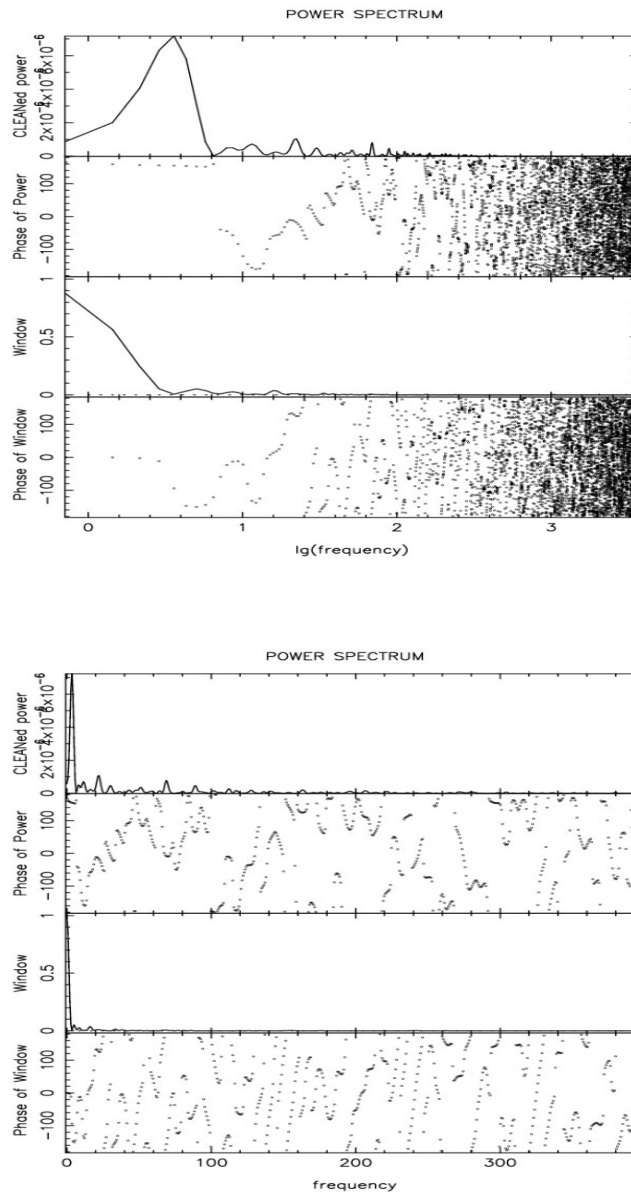


Figure 3.17: Fourier Analysis of 02 August 2005

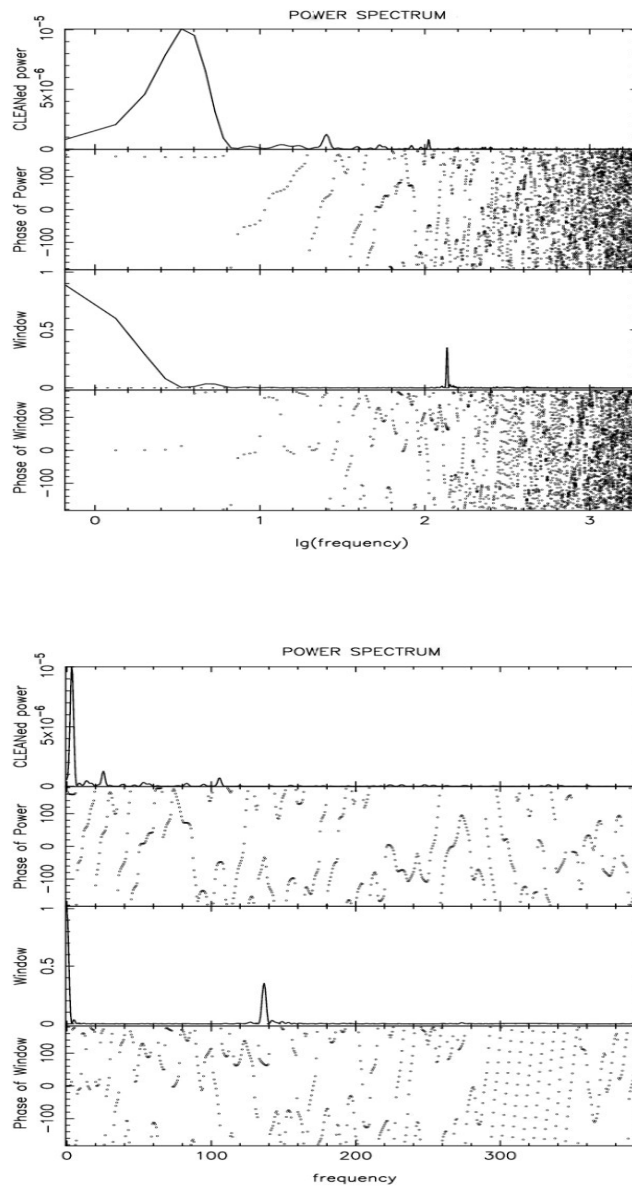


Figure 3.18: Fourier Analysis of 03 August 2005

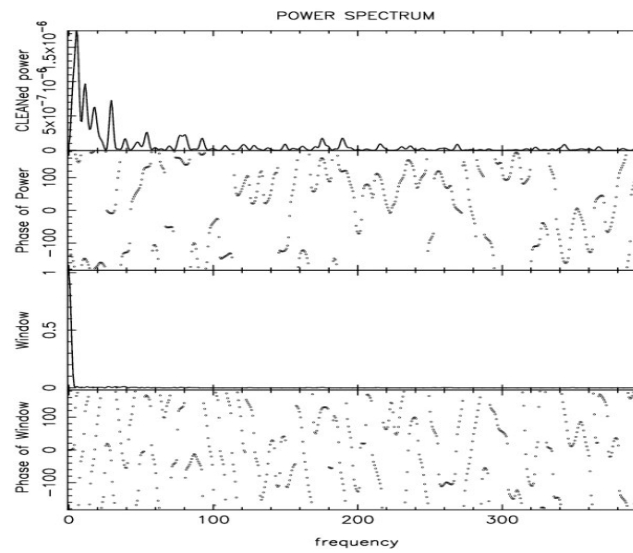
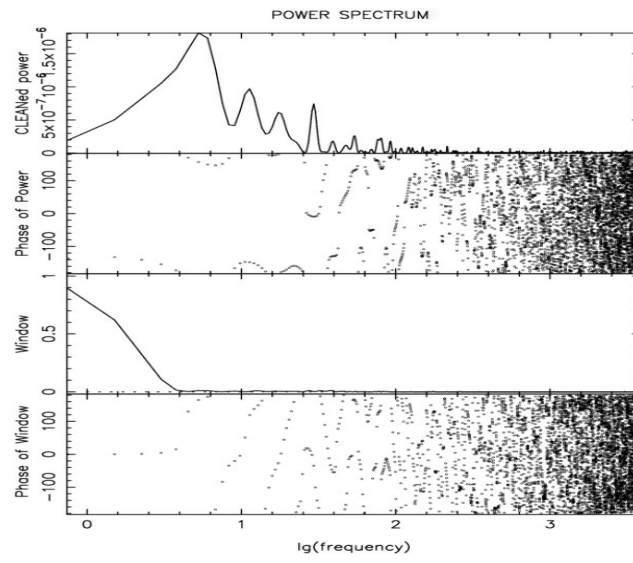


Figure 3.19: Fourier Analysis of 04 August 2005

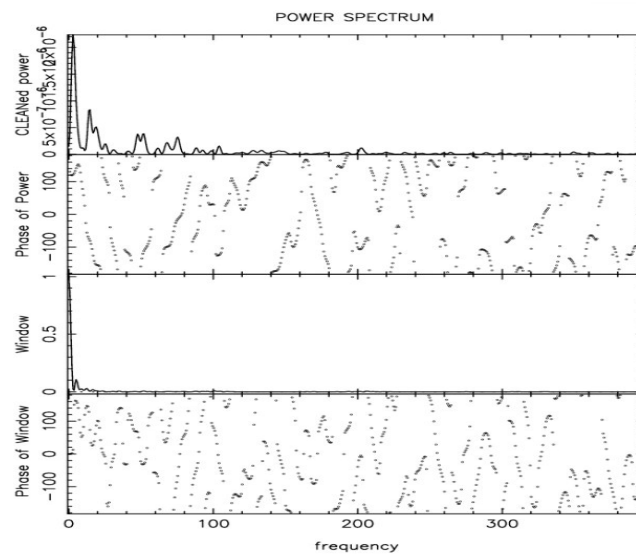
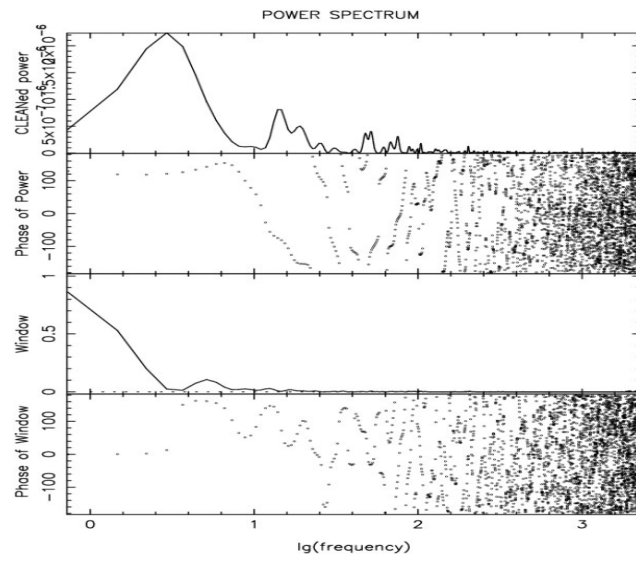


Figure 3.20: Fourier Analysis of 05 August 2005

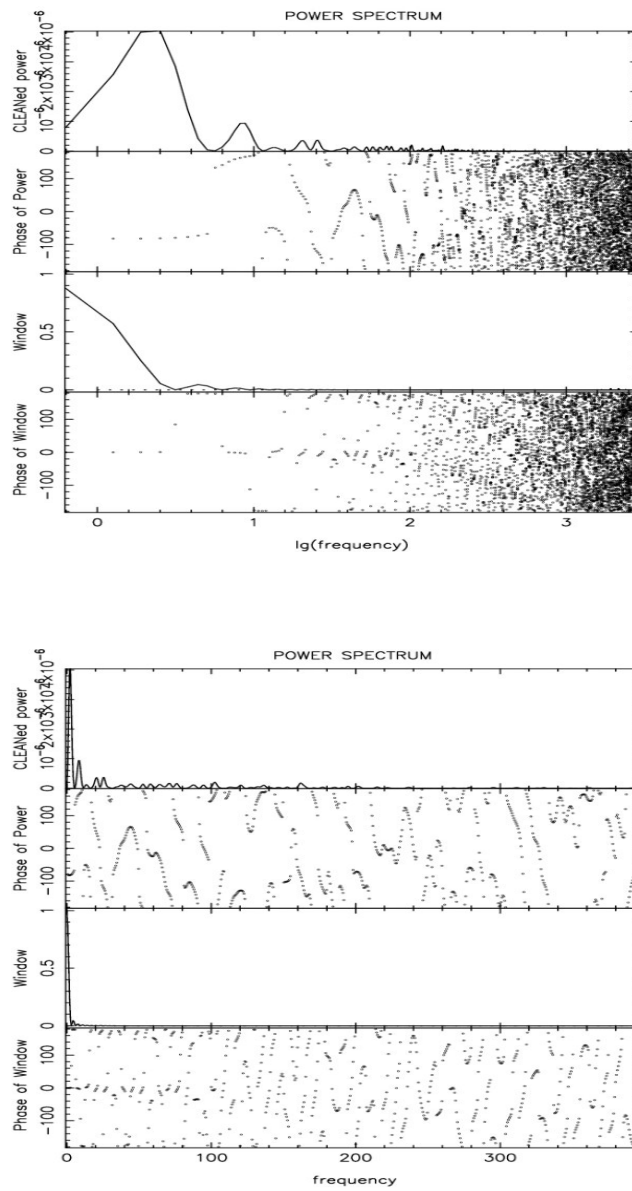


Figure 3.21: Fourier Analysis of 06 August 2005

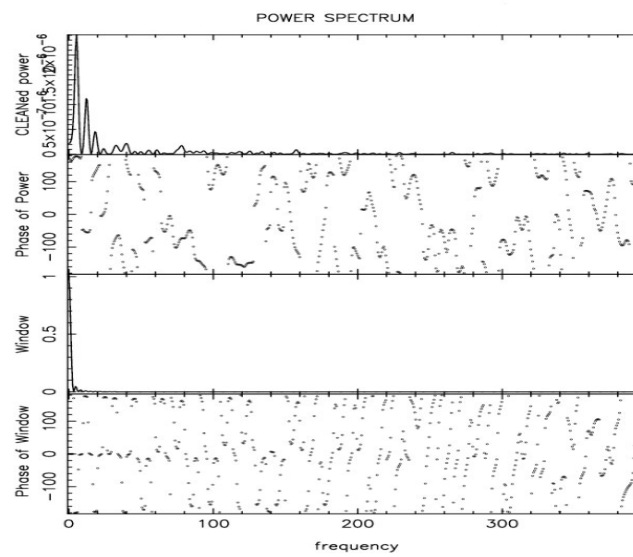
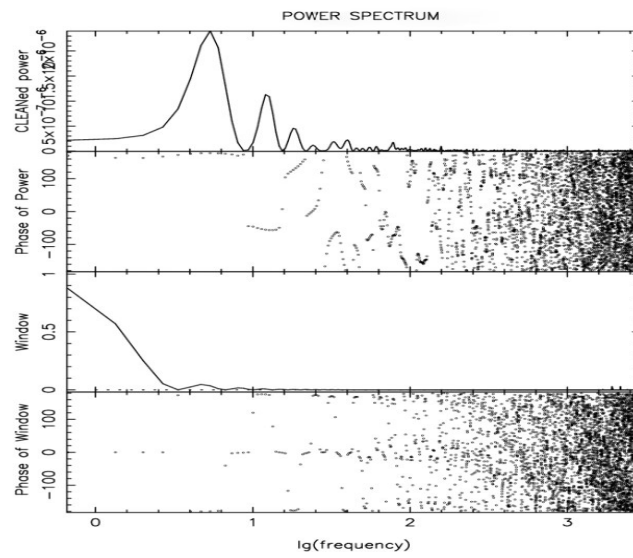


Figure 3.22: Fourier Analysis of 07 August 2005

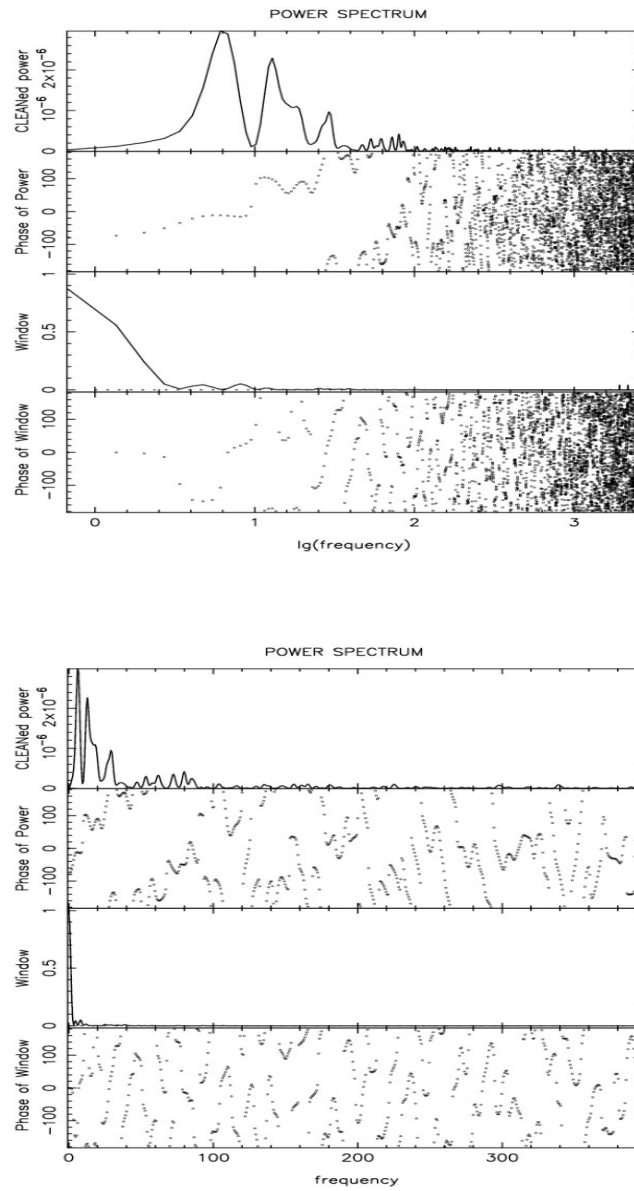


Figure 3.23: Fourier Analysis of 08 August 2005

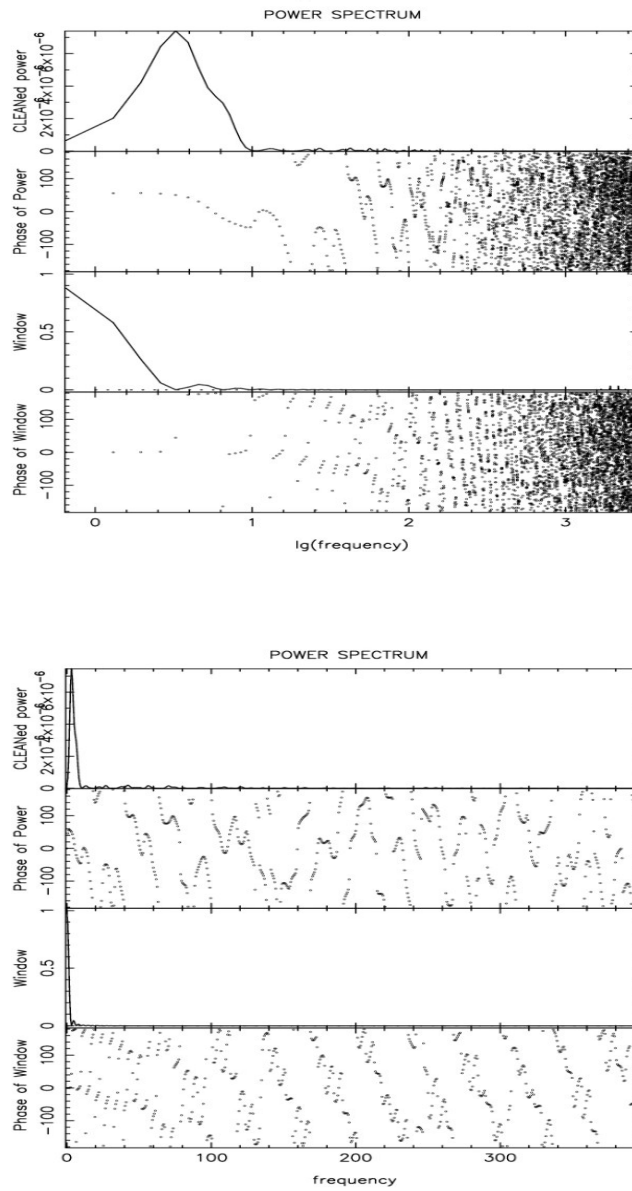


Figure 3.24: Fourier Analysis of 10 August 2005

### **3.3 Wavelet Analysis**

#### **3.3.1 2004-Data**

Here it is presented the wavelet analysis of the light curves, for the 2004 data.

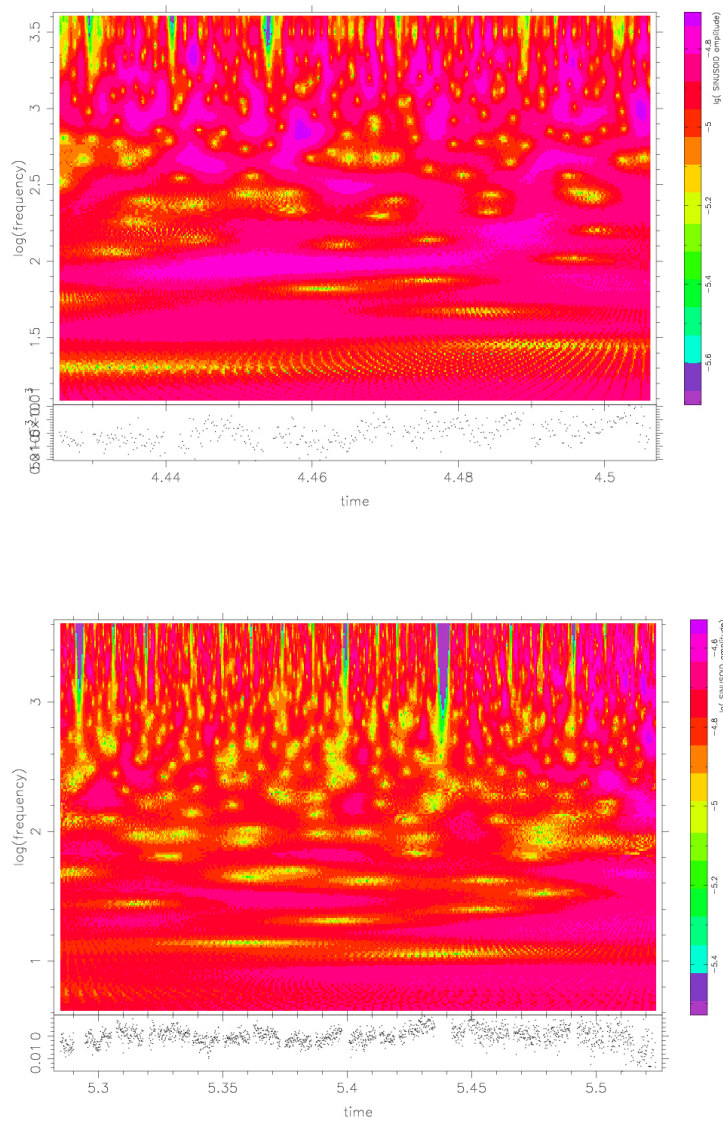


Figure 3.25: Wavelet Analysis of 26 and 27 August 2004

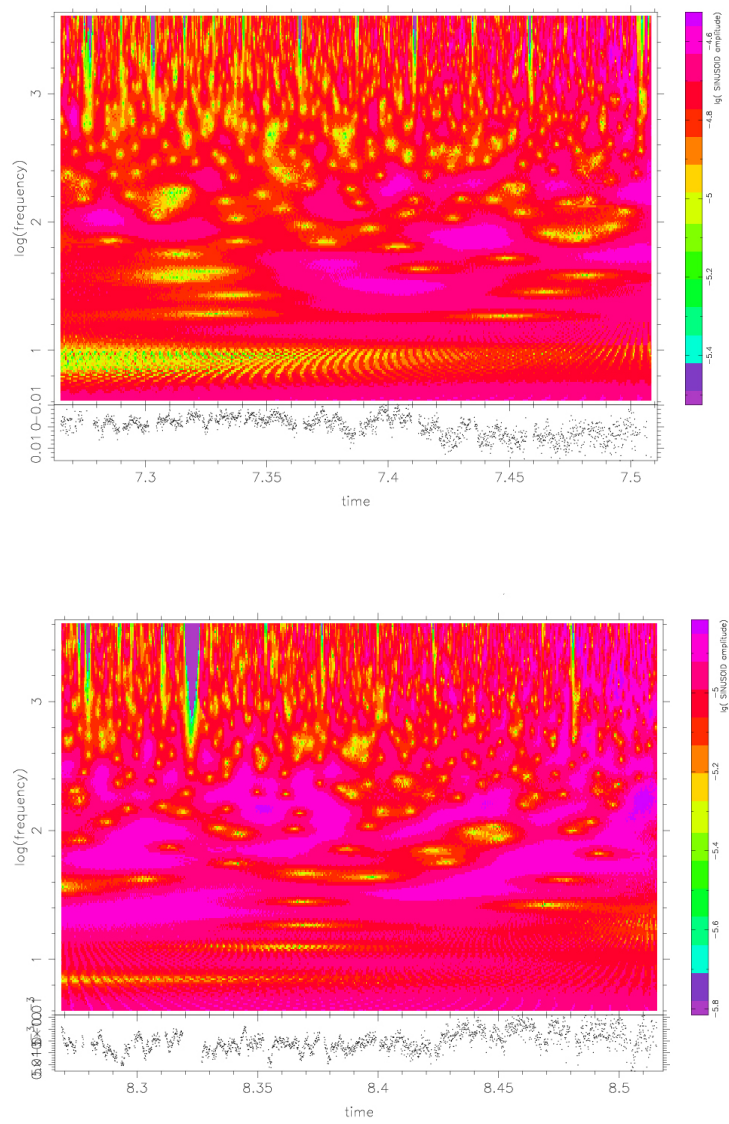


Figure 3.26: Wavelet Analysis of 29 and 30 August 2004

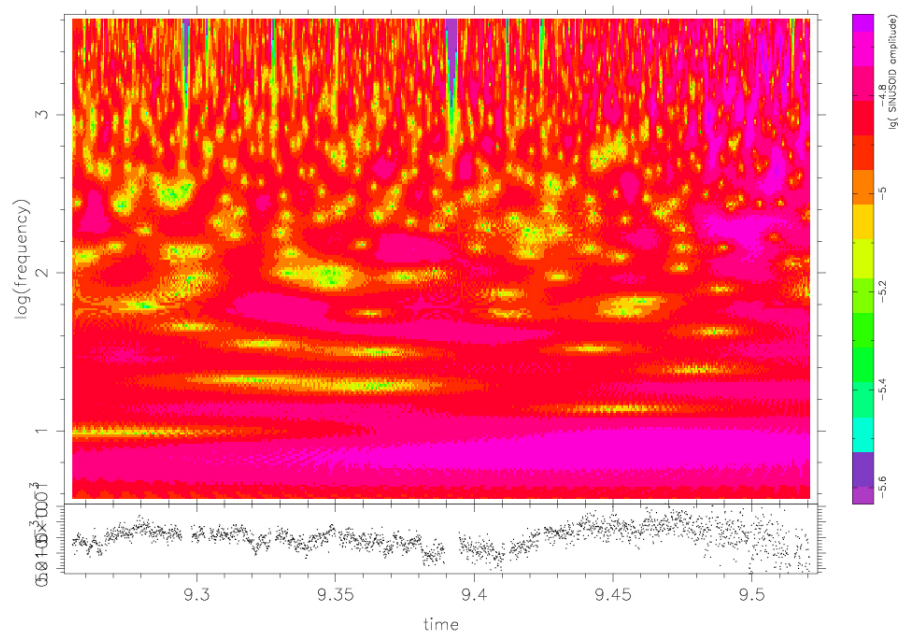


Figure 3.27: Wavelet Analysis of 31 August 2004

#### 3.3.2 2005-Data

Here it is presented the wavelet analysis of the light curves, for the 2005 data.

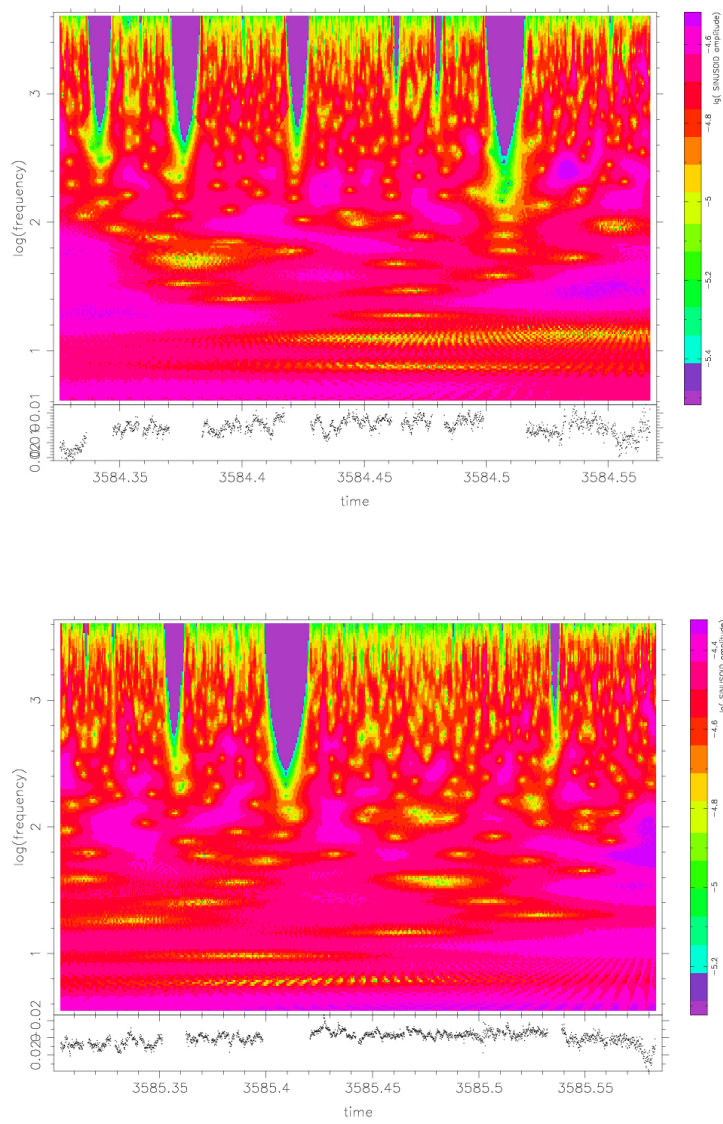


Figure 3.28: Wavelet Analysis of 01 and 02 August 2005

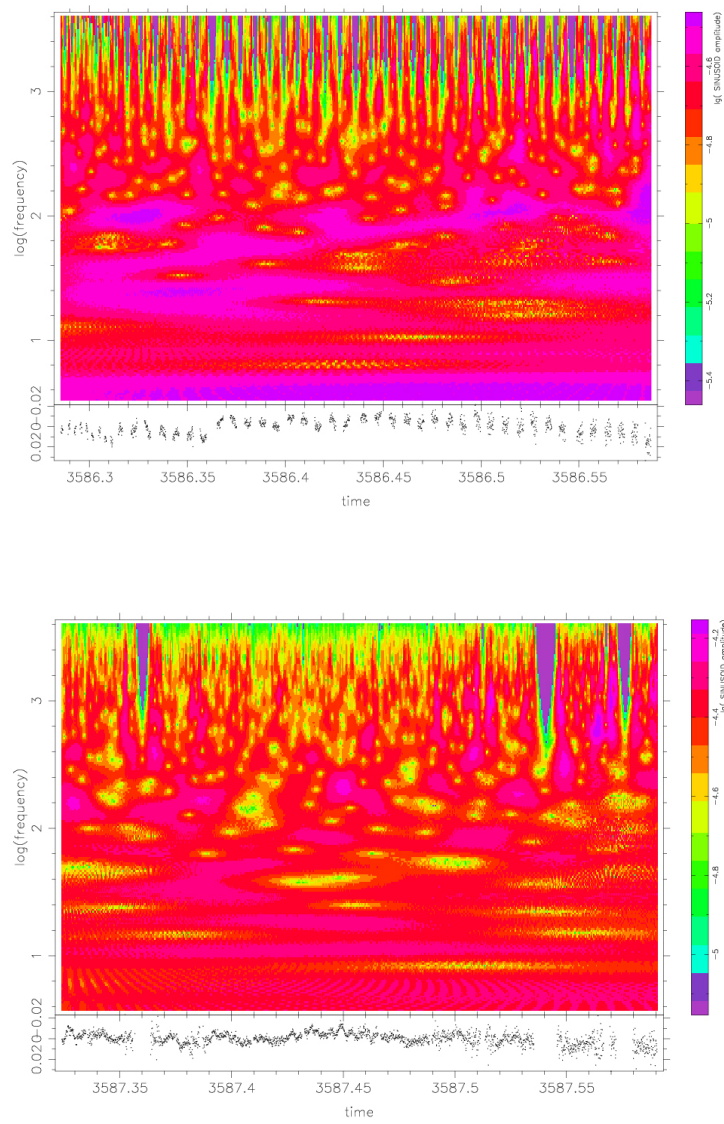


Figure 3.29: Wavelet Analysis of 03 and 04 August 2005

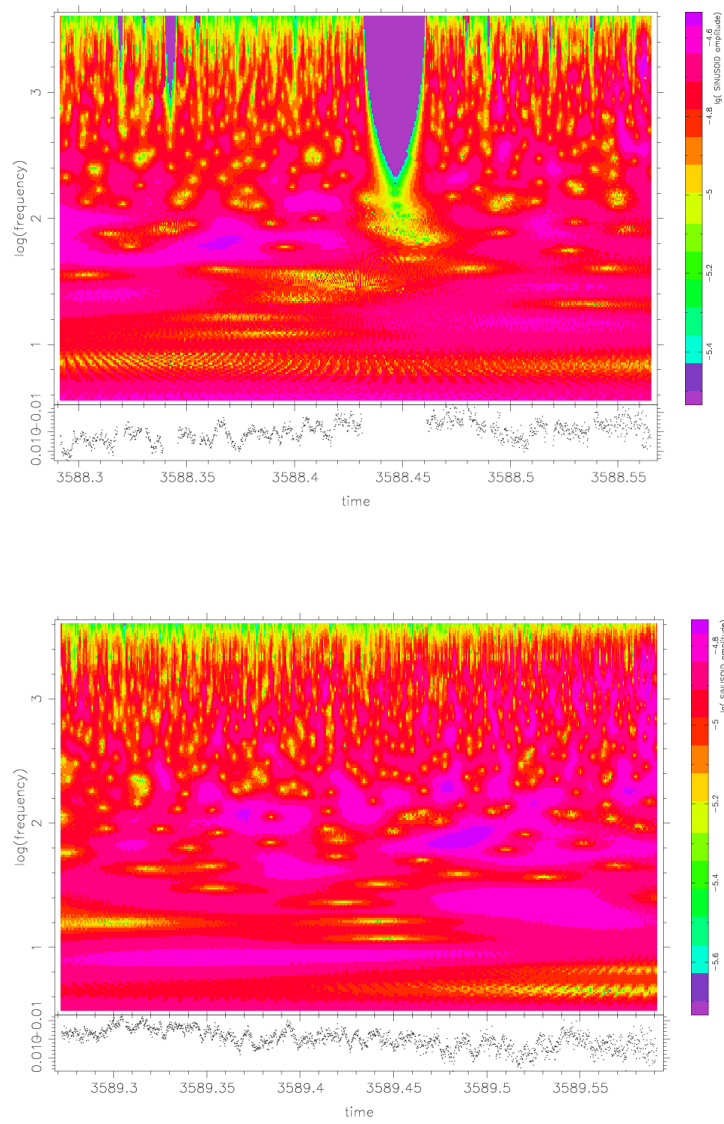


Figure 3.30: Wavelet Analysis of 05 and 06 August 2005

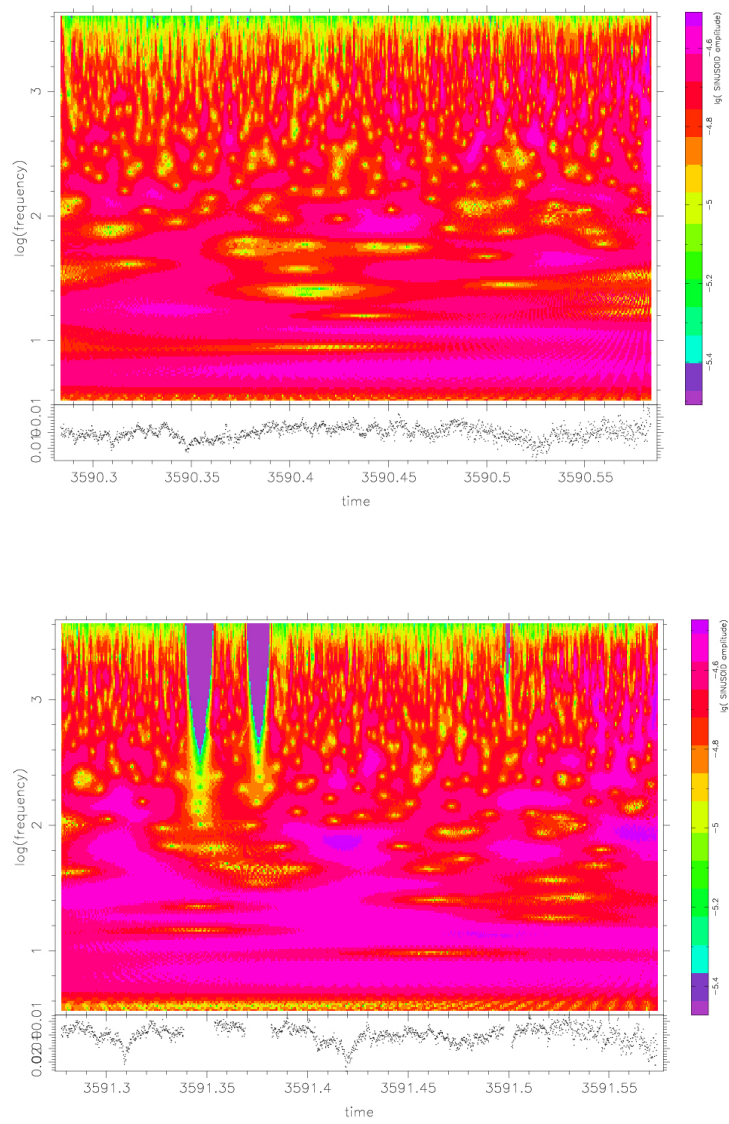


Figure 3.31: Wavelet Analysis of 07 and 08 August 2005

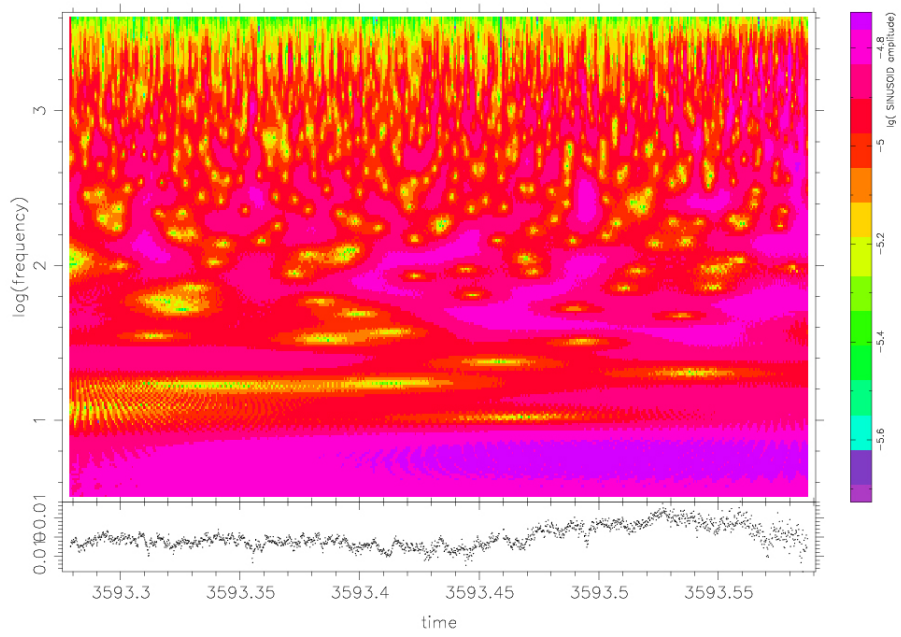


Figure 3.32: Wavelet Analysis of 10 August 2005

### 3.4 Phase Diagram for the Nutational Period Of SS433

The folding was done in the 2005 data. The diagram at figure 3.33 was produced with the linear ephemeris  $Max\Delta V = 2450000.94 + 5.2^d E$ . Folding is very important for the confirmation of a periodicity. Here after folding, a half sine function appears indicating that the physical mechanism producing this kind of a periodicity follows a sinusoidal law. This fact is strong evidence that the signal we have detected is the nutational period of the system. The intermediate variations are probably caused by the chaotic nature of the system in relatively small time scales.

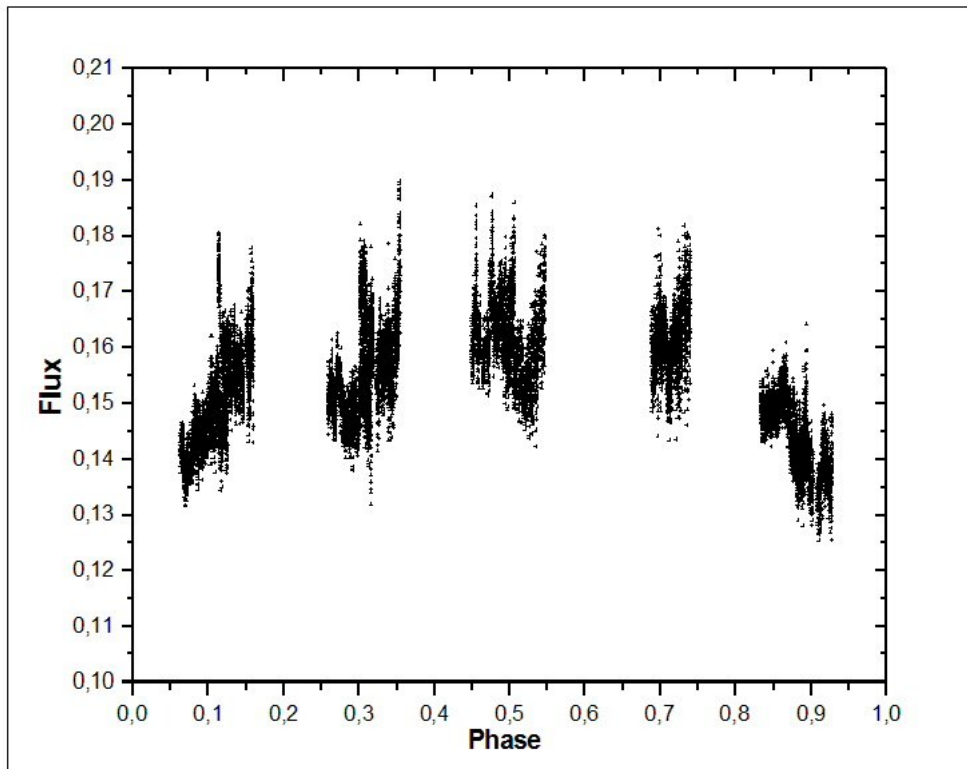


Figure 3.33: Phase Diagram for the Nutational period of the system.

To produce this diagram new fortran code was used to find the corresponding values given a linear ephemeris. Also the code had the capability to interact with the user, in order to fine tune the period of the system.

## Chapter 4

# Results, Conclusions And discoveries

### 4.1 Conclusions

High speed photometry was undertaken on SS433 in 2004 and 2005, with interesting results. It is obvious from the above light curves that SS433 is a highly variable system in time scales between a few minutes and a few hours. In almost all nights a QPO (Quasi Periodic Oscillation) pattern is observed with periods of over 1100s, much bigger than a usual QPO whose period ranges from 60s to 1000s. This probably means that these variations are not actually due to a QPO behaviour, but to random perturbations in the accretion disk. The fact that there is no periodicity stable enough to appear in two or more consecutive nights, could be explained by assuming that every periodicity is unique and short lived.

The important fact is that there is always a periodicity in a scale of tens of minutes showing that there is a physical mechanism capable for producing such a unique temporal behaviour. Further investigation is needed to find out if there is any coherence between the periodicities found here. If any relationship is found then the characterisation as random should be withdrawn.

Another known characteristic of SS433 is that it has distinct active and passive states. During the active (flaring) states the signature of regular orbital and precessional variabilities in the light curves is destroyed. This fact is confirmed from our data if we compare the 2004 with the 2005 observations. Between 26 to 31 August 2004 our data is in agreement with the published linear ephemeris for the orbital period:  $\text{MinI(HJD)} = 2450023.62 + 13\text{d}.08211\text{E}$  (V.P Goranskij et al., 1998), but in 2005, after 04/08, the flux instead of continuing to decrease, it increases until the 08/08, after which it decreases again.

This behaviour could be attributed to a flaring event that occurred in SS433, obscuring the orbital period of 13d,08. It has been shown by Revnivtsev M. (et al., 2004) that simultaneous observations show a clear correlation between the light curves pattern in X-rays and in the optical, with the X-rays being delayed by about 80 sec in respect to the optical. This confirms the fact that any variations discovered here are produced by various physical phenomena in the accretion disk

and not in the donor star. The 80 sec delay is attributed to the light time difference between the compact star and the edge of the accretion disk. Any correlation between these variabilities must take in mind the inclination of the disk in respect to earth.

That was the conclusions of the photometry and the fourier analysis. The results of the Wavelet analysis was far more interesting and revealing. In almost all the diagrams there is a relatively steady periodicity with a value of  $\approx 9$  min. This fact was not even detected with the fourier analysis, showing the strength of wavelet analysis in these kind of time-series. Now we can assume with relatively security that the periodicity of  $\approx 9$  min is caused by a feature in the accretion disk that is stable enough to exist for at least the observing period. The most interesting fact is that this phenomenon is observed both in the data of 2004 and 2005. This is a very important thing since whatever physical mechanism is creating this periodicity has a life of at least one year. This means that there is a strong possibility that the  $\approx 9$  min periodicity is caused by a fundamental characteristic of SS433.

More investigation is needed of course to find out how stable enough is this phenomenon and if it is actual have a span in the scale of years. Of course more observations should be done to find if there are any other characteristics and their properties.

## 4.2 Possible Future Research

A future evolution of the presented work can be done with more observations of longer duration. This duration should be longer than 13 days, in order to detect the orbital period periodicity with a much smaller error margin.

Also if it is possibly, even higher speed photometry should be done so we can investigate the behaviour of SS433 in even smaller time scales. The final thing to say, is that any future research in SS433 should be based upon wavelet analysis and not fourier. This is because of the type of time series that SS433 produces.

## **Part III**

**SEEING AND DIFFERENTIAL IMAGE MOTION MONITOR**

# Chapter 1

## Atmosphere And Astronomical Observing

Our atmosphere. It protects us, nourishes us, and gives us life. However, it also acts as a distorting filter when we view the sky. Below we will see the various effects of the atmosphere that introduces to the incoming star light. But first let's see an important characteristic of the atmosphere, the air mass.

### 1.1 Air Mass - Extinction

An effect which must be corrected when calibrating instrumental magnitudes, is the atmospheric extinction or the dimming of starlight. The longer the path length the starlight traverses through the atmosphere the more it is dimmed. Thus, a star close to the horizon will be dimmed more than one close to the zenith, and the observed brightness of a given star will change throughout a night, as its zenith distance varies. The path length through the atmosphere is known as the air mass. Consider an observation through the blanket of the atmosphere around the curved surface of the Earth. At any particular wavelength,  $\lambda$ , we can relate  $m_0(\lambda)$ , the magnitude of the observed object outside the atmosphere, to  $m(\lambda)$ , the magnitude of the observed object at the surface of the earth, by:

$$m(\lambda) = m_0(\lambda) + \kappa(\lambda)X(z) \tag{1.1}$$

where  $X(z)$  is the air mass,  $\kappa(\lambda)$  is the extinction coefficient at wavelength  $\lambda$  and  $z$  is the zenith distance (the angular distance of the object from the zenith at the time of observation).  $X$  is defined as the number of times the quantity of air seen along the line of sight is greater than the quantity of air in the direction of the zenith and will vary as the observed line of sight moves away from the zenith, that is, as  $z$  increases. Note that the air mass is a normalised quantity and the air mass at the zenith is one. For small zenith angles  $X = \sec z$  is a reasonable approximation, but as  $z$  increases, refraction effects, curvature of the atmosphere and variations of air density with height

can become important. Hardie gives a more refined relationship:

$$X = \sec z - 0.0018167(\sec z - 1) - 0.002875(\sec z - 1)^2 - 0.0008083(\sec z - 1)^3 \quad (1.2)$$

and Young and Irvine propose :

$$X = \sec z (1 - 0.0012(\sec^2 z - 1)) \quad (1.3)$$

Both these equations imply the use of  $z_t$ , the true zenith angle, that is, the zenith angle to the observed object in the absence of the atmosphere as opposed to the apparent zenith angle  $z_a$  affected by refraction effects. The atmospheric extinction coefficient,  $\kappa(\lambda)$ , can be determined by observing the same object (through an appropriate filter) at several times during the night at varying zenith angles. When the observed magnitudes of the object are plotted against computed air mass (see Figure 1.1), they should lie on a straight line with a slope equal to  $\kappa(\lambda)$ . It is important to note that the extinction is dependent upon wavelength, being greater for blue light than red.

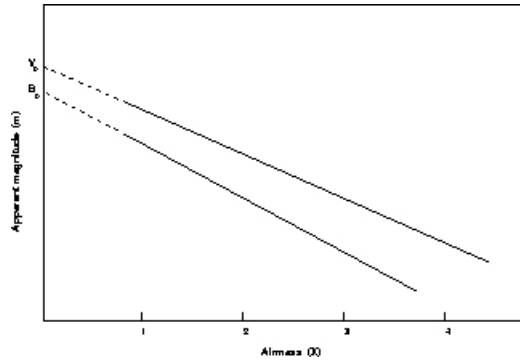


Figure 1.1: Calculation of extinction coefficient.

### 1.1.1 Laplace's extinction theorem

Toward the end of his monumental work on Celestial Mechanics, Laplace has a long chapter dealing with atmospheric refraction. In the course of it, he derives a remarkable result, which seems to have been forgotten by most people today :*the extinction of the atmosphere is related to its refraction*. This conclusion is called Laplace's extinction theorem. Exactly it says that the logarithm of the intensity of light, of any star, is proportional to its refraction, divided by the cosine of its apparent altitude. We must immediately notice that the proportionality constant is negative, because the stars become dimmer as they approach the horizon, and their refractions increase. Furthermore, one should strictly say the relation is a linear one, rather than a simple proportionality. So we have the equation :

$$M \propto \frac{r}{\sin z} \quad (1.4)$$

where  $M$  is the air mass  $r$  is the refraction and  $z$  is the zenith angle. Let's see how this equation is derived.

The differential of airmass is  $dM$  it is just proportional to the differential of path length  $ds$  in figure 1.2, multiplied by the local density,  $\rho$  Let's regard the differential of refraction from a

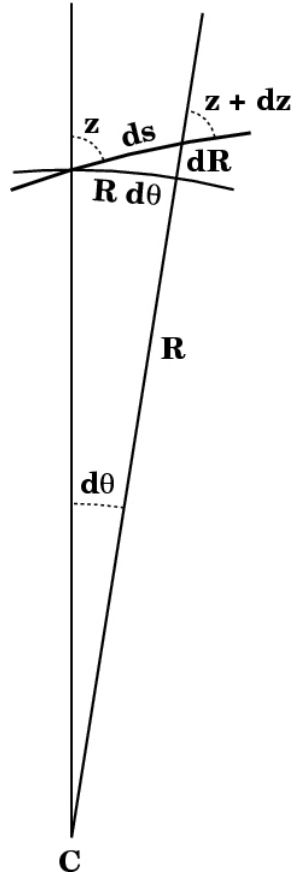


Figure 1.2: Calculation of Laplace's theorem

different point of view:  $dr$  must be equal to the ray curvature multiplied by the element of path length  $ds$ . The curvature in turn, is proportional to the component of the atmospheric density gradient  $d\rho/dh$  normal to the path of the ray. As the atmospheric model is horizontally stratified, its density gradient is a vector directed vertically i.e., toward the zenith. The component of this gradient normal to the ray is just proportional to  $\sin z$ . So we have :

$$dr \propto \frac{d\rho}{dh} \sin z ds \tag{1.5}$$

Now we need to assume that the density gradient is proportional to the density itself. Very near the horizon, the diminution of light depends, like the refraction, upon the constitution of the atmosphere. We may, without fear of any sensible error, use the hypothesis of a uniform temperature. So we

assume an exponential atmosphere, in which  $d\rho/dh \propto \rho$ , and have :

$$dr \propto \rho \sin z ds \quad (1.6)$$

But also we have  $dM \propto \rho ds$ . If we eliminate the product  $\rho ds$  on the right side of the last proportionality for  $dr$  by replacing it with  $dM$ , we see that :

$$dM \propto \frac{dr}{\sin z} \quad (1.7)$$

Then integration will give Laplace's result,  $M \propto r/\sin z$ , provided that we can factor some mean value of  $\sin z$  out of the integrand when we integrate this differential relation. In fact, this is not a bad approximation, because  $\sin z$  is nearly constant through the atmosphere near the zenith (where  $z$  is nearly constant along the line of sight) and  $\sin z$  is itself nearly constant near the horizon, because the sine function flattens out near unity when  $z$  is near  $90^\circ$ .

Notice that Laplace's result is trivially true for the flat-Earth approximation, where  $M = \sec z$  and  $r \propto \tan z$ . Also, in a long duct, where the ray simply follows the curve of the Earth, and  $\sin z$  is unity, the refraction in the duct is obviously proportional to the path length there.

## 1.2 Atmospheric refraction

The direction of light as it passes through the atmosphere is also changed because of refraction since the index of refraction changes through the atmosphere. The amount of change is characterized by Snell's law:

$$\mu_1 \sin \theta_1 = \mu_2 \sin \theta_2 \quad (1.8)$$

Let  $z_0$  be the true zenith distance,  $z$  be the observed zenith distance,  $z_n$  be the observed zenith distance at layer  $n$  in the atmosphere,  $\mu$  be the index of refraction at the surface, and  $\mu_n$  be the index of refraction at layer  $n$ . At the top of the atmosphere it is :

$$\mu_N = \frac{\sin z_0}{\sin z_N} \quad (1.9)$$

At each infinitesimal layer we have :

$$\frac{\sin z_n}{\sin z_{n-1}} = \frac{\mu_{n-1}}{\mu_n} \quad (1.10)$$

as so on for each layer down to the lowest layer it will be :

$$\frac{\sin z_1}{\sin z} = \frac{\mu}{\mu_1} \quad (1.11)$$

By multiplying equations 1.10 and 1.11 we get:

$$\sin z_0 = \mu \cdot \sin z \quad (1.12)$$

from which we can see that the refraction depends only by the index of refraction near the earth's surface. We define astronomical refraction  $r$ , to be the angular amount that the object is displaced by the refraction of the Earth's atmosphere :

$$\sin(z + r) = \mu \sin z \quad (1.13)$$

in cases where  $r$  is small (pretty much always) it is :

$$r = (\mu - 1) \tan z \equiv R \tan z \quad (1.14)$$

where we have defined  $R$ , known as the "constant of refraction". A typical value of the index of refraction is  $\mu \sim 1.00029$ , which gives  $R = 60\text{arcsec}$  (red light). The direction of refraction is that a star apparently moves towards the zenith. Consequently in most cases, star moves in both RA and DEC:

$$r_\alpha = r \sin q$$

$$r_\delta = r \cos q$$

where  $q$  is the parallactic angle, the angle between N and the zenith :

$$\sin q = \cos \phi \frac{\sin h}{\sin z} \quad (1.15)$$

Note that the expression for  $r$  is only accurate for small zenith distances ( $z < 45$ ). At larger  $z$ , we can't use the approximation of a plane parallel atmosphere. Observers have empirically found that :

$$r = A \tan z + B \tan^3 z \quad (1.16)$$

where  $A = (\mu - 1) + B$  and  $B \sim -0.07''$ . But these vary with time, so for precise measurements,  $A$  and  $B$  must be calculated each night of observations. Of course, the index of refraction varies with wavelength, so consequently does the astronomical refraction, this gives rise to the phenomenon of *atmospheric dispersion*, or *differential refraction*. Because of the variation of index of refraction with wavelength, every object actually appears as a little spectrum with the blue end towards the zenith. The spread in object position is proportional to  $\tan z$ . Note the importance of this effect for spectroscopy, and the consequent importance of the relation between a slit orientation and the parallactic angle.

## Chapter 2

# Theory Of Astronomical Seeing

*“Seeing Clearer. . .”*

Generally, a perfect astronomical optical system will make a perfect (diffraction-limited) image for an incoming plane wavefront of light. The Earth’s atmosphere is turbulent and variations in the index of refraction cause the plane wavefront from distant objects to be distorted. This distortion introduces amplitude variations, positional shifts and also image degradation. This causes two astronomical effects :

- *Scintillation*. Which is amplitude variations, which typically vary over scales of cm: generally very small for larger apertures
- *Seeing*. Positional changes and image quality changes. The effect of seeing depends on aperture size: for small apertures, one sees a diffraction pattern moving around, while for large apertures, one sees a set of diffraction patterns (speckles) moving around on scale of  $\sim 1$  arcsec. These observations imply local wavefront curvatures flat on scales of small apertures, and instantaneous slopes that vary for about an arcsec. The time variation scales are several milliseconds and up. The effect of seeing can be derived from theories of atmospheric turbulence, worked out originally by Kolmogorov, Tatarski, Fried. Here, I’ll quote some pertinent results, without derivation.

## 2.1 In General About Seeing and Turbulent Flows

### 2.1.1 Kolmogorov Model And the Fried Parameter

A description of the nature of the wavefront perturbations introduced by the atmosphere is provided by the *Kolmogorov model* based partly on the studies of turbulence by the Russian mathematician Andrei Kolmogorov. This model is supported by a variety of experimental measurements and is widely used in simulations of astronomical imaging. The model assumes that the wavefront perturbations are brought about by variations in the refractive index of the atmosphere. These refractive

index variations lead directly to phase fluctuations described by  $\phi_a(\mathbf{r})$ , but any amplitude fluctuations are only brought about as a second-order effect while the perturbed wavefronts propagate from the perturbing atmospheric layer to the telescope. For all reasonable models of the Earth's atmosphere at optical and infra-red wavelengths the instantaneous imaging performance is dominated by the phase fluctuations  $\phi_a(\mathbf{r})$ . The amplitude fluctuations described by  $\chi_a(\mathbf{r})$  have negligible effect on the structure of the images seen in the focus of a large telescope.

A turbulent field can be described statistically by a structure function:

$$D_N(x) = \langle |N(r+x) - N(r)|^2 \rangle \quad (2.1)$$

where  $x$  is separation of points,  $N$  is any variable (e.g. temperature, index of refraction, etc) and  $r$  is position. Kolmogorov turbulence gives :

$$D_n(x) = C_n^2 \frac{x^2}{3} \quad (2.2)$$

where  $C_n$  is the refractive index structure constant. From this, one can derive the phase structure function at the telescope aperture :

$$D_\phi(x) = 6.88 \left( \frac{x}{r_0} \right)^{5/3} \quad (2.3)$$

where the coherence length  $r_0$  (also known as the Fried parameter) is :

$$r_0 = 0.185 \lambda^{6/5} \cos^{3/5} z \left[ \int (C_n^2 dh) \right]^{-3/5} \quad (2.4)$$

where  $z$  is zenith angle,  $\lambda$  is wavelength. Using optics theory, one can convert  $D_\phi$  into an image shape. Physically,  $r_0$  is inversely proportional to the image size from seeing :

$$d \sim 0.98 \frac{\lambda}{r_0} \quad (2.5)$$

as compared with the image size from diffraction-limited images :

$$d \sim 1.22 \frac{\lambda}{D} \quad (2.6)$$

Seeing dominates when  $r_0 < D$ , a larger  $r_0$  means better seeing. Seeing is more important than diffraction at shorter wavelengths (and for larger apertures), diffraction is more important at longer wavelengths (and for smaller apertures), the effects of diffraction and seeing cross over in the IR for most astronomical-sized telescopes ( $\sim 5$  microns for 4m), the crossover falls at a shorter wavelength for smaller telescope or better seeing. The meaning of  $r_0$  is in  $\int (C_n^2 dh)$  as you might expect, this varies from site to site and also in time. At most sites, there seems to be three regimes : "surface layer" (wind-surface interactions and manmade seeing), "planetary boundary layer" (influenced by diurnal heating), and "free atmosphere" (high wind shears, 10 km is tropopause). A typical

astronomical site has  $r_0 \sim 10$  cm at 5000Å. We also have to consider the coherence of the same turbulence pattern over the sky : coherence angle called the isoplanatic angle, and region over which the turbulence pattern is the same, is called the isoplanatic patch. So it is :

$$\theta \sim 0.314 \frac{r_0}{H} \quad (2.7)$$

where  $H$  is the average distance of the seeing layer :

$$H = \sec z \left[ \frac{\int (C_n^2 h^{5/3} dh)}{\int (C_n^2 dh)} \right]^{3/5} \quad (2.8)$$

At a typical astronomical site where we have  $r_0 = 10$ cm in the optical it will be  $H \sim 5000$ m and  $\theta \sim 1.3$ arcsec. In the infrared where it's  $r_0 \sim 70$ cm it will be  $H \sim 5000$ m and  $\theta \sim 9$ arcsec.

In reality, phase fluctuations in the atmosphere are only expected to follow the structure function shown in equation 2.3 over a finite range of length scales. The turbulent energy is injected at large scales by wind shear. The bulk of the wind shear is expected in discrete layers of the atmosphere, and the largest turbulent structures are expected to fit within one of these atmospheric layers. The length scale at which the structure function for Kolmogorov turbulence breaks down at large scales is called the outer scale of turbulence ( $L_0$ ). Several attempts have been made at measuring the size of this outer scale using a variety of different methods but there has been substantial variation in the measured values. The Von Karman model (Ishimaru, 1978) is expected to describe the form of the power spectrum for phase fluctuations on length scales larger than the outer scale. If the outer scale is larger than the telescope diameter, then most of the properties of short exposure astronomical images will not depend significantly on the precise size of the outer scale (although the amplitude of image motion is still weakly dependent on the outer scale size).

At small scales ( $< 1$ cm) the turbulent energy in the atmosphere is dissipated through the viscosity of the air (Roddier, 1981). The length scale at which this becomes significant is called the inner scale of turbulence ( $l_0$ ). The steepness of the Kolmogorov turbulence spectrum means that any reduction in the power at such small length scales has relatively little effect on the imaging performance of optical and infra-red telescopes.

### 2.1.2 Temporal Behaviour of Turbulence

A model for the time-dependence of the phase fluctuations can be derived from the spatial fluctuations under the assumption of “frozen turbulence”, that is to say that the turbulent cells are blown past the observer faster than the cells themselves evolve. Observational evidence for the validity of this hypothesis has been obtained by Caccia, Azouit & Vernin (1987), although only for cells of air with characteristic sizes of a few cm. Under this assumption, the temporal phase structure function will have the form

$$D_{t,\varphi}(t) \equiv \langle [\varphi(t') - \varphi(t' + t)]^2 \rangle = \left(\frac{t}{t_0}\right)^{5/3} \quad (2.9)$$

where  $\varphi(t)$  is the phase perturbation at a given point on the wavefront at time  $t$ . This equation serves to define a 'coherence time'  $t_0$  (Buscher 1988) which is related to  $r_0$  and the windspeed  $V$  by the equation :

$$t_0 = 0.314 \frac{r_0}{V} \quad (2.10)$$

It should be noted that no single definition of the coherence time has been adopted by the optical community. Colavita, Shao & Staelin (1987) define a coherence time  $T_0$  such that  $T_0 = 0.81r_0/V$ . As in the spatial case, equation 2.10 is valid only for  $l_0 \ll Vt \ll L_0$ . Where  $l_0$  and  $L_0$  is the inner and outer scale of turbulence respectively. Also the velocity  $V$  is given by the equation :

$$V = \left[ \frac{\int_0^\infty C_n^2(h) \cdot V(h)^{5/3} dh}{\int_0^\infty C_n^2(h) dh} \right]^{3/5} \quad (2.11)$$

Where  $C_n^2(h)$  is the vertical profiles of the turbulence and  $h$  the height from the ground.

Finally, we can define the relationship between the temporal power spectrum  $W_{f,\varphi}$  and the temporal structure function of the phase perturbations via a Fourier transform :

$$D_{t,\varphi}(t) = 2 \int_{-\infty}^{\infty} W_{f,\varphi}(f) df - 2 \int_{-\infty}^{\infty} W_{f,\varphi}(f) e^{2\pi i f t} df \quad (2.12)$$

This gives for the structure function of equation 2.9 a power spectrum :

$$W_{f,\varphi} = 5.6 \cdot 10^{-3} t_0^{-5/3} |f|^{-8/3} \quad (2.13)$$

In the above discussions it has been assumed that there is a single layer of turbulence being blown past the observer. In fact there is a large body of experimental evidence showing that there are many layers of turbulence at difference heights contributing to the seeing, each a few metres thick each moving with a different speed and direction, and each with its own outer scale. The properties of the seeing affecting a star observed at ground level will be an average of the properties of these layers, weighted by the strength of the refractive-index fluctuations in each layer. Thus, for example,  $V$  in equation 2.10 will be an 'average windspeed', rather than the speed of any particular layer. Here something must be mentioned about the effects of dome seeing. The steep temperature gradients formed by the mixing of warm air in the dome (produced by instruments and machinery) and colder air outside can produce very strong refractive index effects. Any turbulent cells inside the dome will be driven primarily by convection and so will not conform to the 'frozen turbulence' assumption. It is also likely that these will not be described by Kolmogorov statistics, i.e. the turbulence is not 'fully developed'. As you can understand coherence time  $t_0$  is very important for adaptive optics systems, since it is the minimum time that corrections must be done.

### 2.1.3 Impact of Turbulence (Seeing) to an Image

The "quality" of an image can be described in many different ways. The overall shape of the distribution of light from a point source is specified by the point spread function. Diffraction gives a basic

limit to the quality of the PSF, but any aberrations or image motion add to structure/broadening of the PSF. Another way of describing the quality of an image is to specify its modulation transfer function (MTF). The MTF and PSF are a Fourier transform pair. Turbulence theory gives:

$$MTF(\nu) = \exp \left[ -3.44 \left( \frac{\lambda \cdot \nu}{r_o} \right)^{5/3} \right] \quad (2.14)$$

where  $\nu$  is the spatial frequency. Note that a gaussian goes as  $\nu^2$ , so this is close to a gaussian. The shape of seeing-limited images is roughly Gaussian in core but has more extended wings. This is relevant because the seeing is often described by fitting a Gaussian to a stellar profile. A potentially better empirical fitting function is a Moffat function :

$$I = p_1 \left( 1 + (x - p_2)^2/p_4^2 + (y - p_3)^2/p_5^2 \right)^{-p_6} \quad (2.15)$$

A final way of characterizing the image quality, more commonly used in adaptive optics applications, is the Strehl ratio. The Strehl ratio is the ratio between the peak amplitude of the PSF and the peak amplitude expected in the presence of diffraction only.

## Chapter 3

# Methods to Calculate Astronomical Seeing - The DIMM

*“Differential Imaging Makes Magic ...”*

Probably the most common way of describing the seeing is by specifying the full width half maximum (FWHM) of the image, which may be estimated either by direct inspection or by fitting a function (usually a Gaussian), note the correspondence of FWHM to  $\sigma$  of a gaussian:  $FWHM = 2.355\sigma$ . This fact is shown in figure 3.1 We can measure FWHM in a astronomical image very easy with

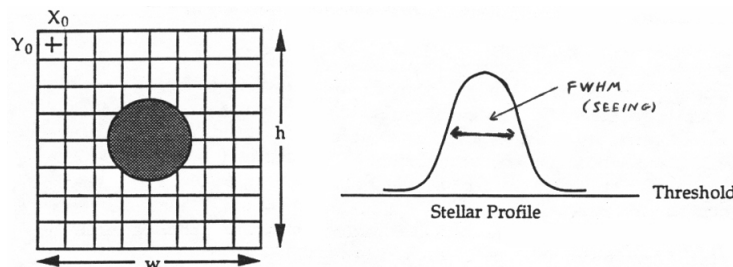


Figure 3.1: The Full Width Half Maximum (FWHM)

many programs that have that feature. The problem is that such a measurement will not be accurate for various reasons :

- Guiding problems
- Focus problems

All these reasons cause the FWHM to be overestimated. Thus we need a method to overcome all these problems. Such a method is the DIMM method that will be analyzed in the next paragraph.

### 3.1 DIMM - Differential Image Motion Monitor

The DIMM method consists of measuring wavefront slope differences over two small pupils some distance apart. Because it is a differential method, the technique is inherently insensitive to tracking errors. It had already been used as early as 1960 to provide qualitative seeing estimates. The theory of differential measurements is now well understood. It shows that the differential motion exceeds the absolute motion as soon as the distance between the two apertures equals a few times their diameter. Hence a compact instrument can be built and still provide good sensitivity. One needs to select the starlight having passed through two circular apertures in the entrance pupil plane (Hartmann holes) so as to obtain dual star images whose relative motion in the image plane represent local wavefront tilts. This is shown in figure 3.2. The theory is reviewed below, ESO and Hartmann seeing monitors are described.

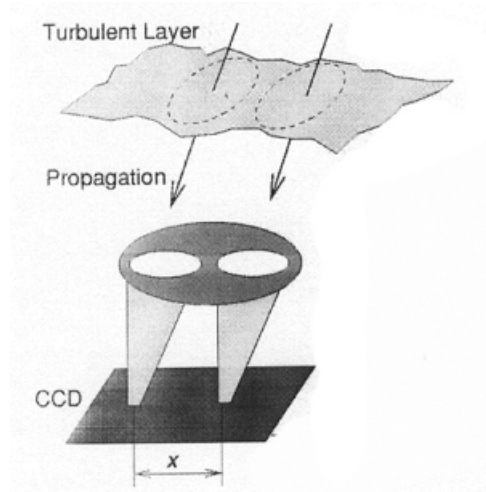


Figure 3.2: Visualisation Of The DIMM Method

#### 3.1.1 ESO-DIMM

The ESO-DIMM method in order to produce the two images in the focal plane, uses a prism in one of the Hartmann hole to deverse light. Below is the theory of the ESO-DIMM.

The wavefront corrugation  $z(x, y)$  is proportional to the wavefront phase error  $\phi(x, y)$  :

$$z(x, y) = \frac{\lambda}{2\pi} \phi(x, y) \quad (3.1)$$

Since light rays are normal to the wavefront surface, the component  $\alpha$  of the angle-of-arrival fluctuation in the  $x$  direction is given by :

$$\alpha(x, y) = -\frac{\partial}{\partial x} z(x, y) = \frac{\lambda}{2\pi} \frac{\partial}{\partial x} \phi(x, y) \quad (3.2)$$

Hence, the covariance of the angle-of-arrival fluctuation is :

$$B_\alpha(\xi, \eta) = \langle \alpha(x, y), \alpha(x + \xi, y + \eta) \rangle \quad (3.3)$$

is related to the covariance  $B_\phi(\xi, \eta)$  of the phase fluctuation by :

$$B_\alpha(\xi, \eta) = -\frac{\lambda^2}{4\pi^2} \frac{\partial^2}{\partial \xi^2} B_\phi(\xi, \eta) \quad (3.4)$$

and introducing the phase structure function :

$$D_\phi(\xi, \eta) = 2[B_\phi(0, 0) - B_\phi(\xi, \eta)] \quad (3.5)$$

and so it becomes :

$$B_\alpha(\xi, \eta) = \frac{\lambda^2}{8\pi^2} \frac{\partial^2}{\partial \xi^2} D_\phi(\xi, \eta) \quad (3.6)$$

For Kolmogorov turbulence at the near-field approximation, the phase structure function is given by the widely used expression (2.3) :

$$D_\phi(\xi, \eta) = 6.88 \left( \frac{r}{r_o} \right)^{5/3} \quad (3.7)$$

where  $r = \sqrt{\xi^2 + \eta^2}$  and  $r_o$  is Fried's seeing parameter. Putting 3.7 into 3.6 gives :

$$B_\alpha(\xi, \eta) = 0.145 \lambda^2 r_o^{-5/3} \left[ (\xi^2 + \eta^2)^{-1/6} - \frac{1}{3} \xi^2 (\xi^2 + \eta^2)^{-7/6} \right] \quad (3.8)$$

For  $\eta = 0$  we get the longitudinal covariance (in the direction of the tilt) as a function of the separation  $\xi = d$  :

$$B_\alpha(d, 0) = 0.097 \left( \frac{\lambda}{r_o} \right)^{5/3} \left( \frac{\lambda}{d} \right)^{1/3} \quad (3.9)$$

For  $\xi = 0$ , we get the lateral or transverse covariance (in a direction perpendicular to the tilt) as a function of the separation  $\eta = d$  :

$$B_\alpha(0, d) = 0.145 \left( \frac{\lambda}{r_o} \right)^{5/3} \left( \frac{\lambda}{d} \right)^{1/3} \quad (3.10)$$

The transverse covariance is exactly 1.5 times larger than the longitudinal covariance and both decrease as the  $-1/3$  power of the separation. This was well confirmed experimentally by Borgnino et al. (1978). These expressions are valid only within the inertial range of the Kolmogorov spectrum. The divergence at the origin is clearly not physical. In practice, the value at the origin is limited by aperture averaging and is given by the expression for the variance of image motion derived by Fried (1965, 1975), and Tatarski (1971), (within a factor of two since we consider motion in one direction only) :

$$B_\alpha(0, 0) = 0.179 \left( \frac{\lambda}{r_o} \right)^{5/3} \left( \frac{\lambda}{D} \right)^{1/3} \quad (3.11)$$

where  $D$  is the diameter of the apertures through which tilts are measured. Because of the slow decrease of the covariance as the  $-1/3$  power of the distance in 3.9 and 3.10, aperture averaging does not noticeably modify the covariance function as soon as the distance exceeds twice the aperture diameter, as shown below. The variance  $\sigma^2(d)$  of the differential image motion observed over a distance  $d$  is given by :

$$\sigma^2(d) = 2[B(0) - B(d)] \quad (3.12)$$

Putting 3.9 and 3.11 into 3.12 gives an approximate expression for the variance  $\sigma_l^2$  of the differential longitudinal motion for  $d \geq 2D$  :

$$\sigma_l^2 = 2\lambda^2 r_0^{-5/3} [0.179D^{-1/3} - 0.0968d^{-1/3}] \quad (3.13)$$

whereas putting 3.10 and 3.11 into 3.12 gives an approximate expression for the variance  $\sigma_t^2$ , of the differential transverse motion for  $d \geq 2D$  :

$$\sigma_t^2 = 2\lambda^2 r_0^{-5/3} [0.179D^{-1/3} - 0.145d^{-1/3}] \quad (3.14)$$

These variances can be expressed in terms of the total variance for 2-dimensional motion through a single aperture of diameter  $D$  :

$$\sigma^2 = 2B_\alpha(0, 0) = 0.358 \left(\frac{\lambda}{r_0}\right)^{5/3} \left(\frac{\lambda}{D}\right)^{1/3} \quad (3.15)$$

Putting 3.15 into 3.13 and 3.14 with  $S = d/D$  gives :

$$\sigma_l^2 = [1 - 0.541S^{-1/3}] \sigma^2$$

$$\sigma_t^2 = [1 - 0.811S^{-1/3}] \sigma^2$$

The above equations are the basis of the DIMM method.

### 3.1.2 Hartmann-DIMM

The H-DIMM method for measuring the astronomical seeing is a modification of the ESO-DIMM. So all the theory mentioned until now, applies to both methods equally. In the H-DIMM the two images are produced by a simple out of focus hartmann mask, with no prism. So here i will tell only for the influence of the defocusing of the telescope, since for the calculation of the seeing value through the differential image motion, the same equations are used.

Elimination of the image separation prisms is possible because the depth of field of the sub-apertures is much larger than that of the parent optical system. For an aperture diameter  $D$ , wavelength  $\lambda$  and focal length  $f$ , the depth of field is given by :

$$2\Delta Z = 1.22\lambda \left(\frac{f}{D}\right)^2 \quad (3.16)$$

Therefore, if the imaging CCD is displaced from best focus by an amount  $< \Delta Z$  (either inside focus or outside focus), then the point spread function produced by each sub-aperture will be indistinguishable from perfectly focused subaperture images. However, the images produced by sub-apertures separated by a distance  $d$  become well separated when :

$$\Delta z > 1.22\lambda \left(\frac{f}{d}\right)^2 \quad (3.17)$$

When the detector is located at a distance  $Z$  from the focal plane of the imaging telescope, where  $\Delta z < Z < \Delta Z$ , all images of a star produced by subapertures separated by more than  $d$  from each other will be well separated in the image plane, and will be in perfect focus. Under these circumstances, the differential image motion is easy to determine from the fluctuations in the centroids of each image from one exposure to the next.

An optimal ratio of image separation to diameter is achieved by locating the detector at  $Z \approx \Delta Z$  from best focus.

### 3.2 Air Mass And Wavelength Dependence

In a previous paragraph we saw that there is a dependence of air mass with the altitude (zenith angle) is by the equation 1.2. So as the air mass changes so seeing will do. From theoretical consideration one can derive that the seeing  $S$  is proportional to the 0.6th power of the airmass  $a$  :

$$S = S_0 \cdot a^{0.6} \quad (3.18)$$

Where  $S_0$  is the value of seeing at zenith. Equation 3.1 is used to correct DIMM data from different altitudes and is essential so the data to be self-consistent.

The seeing also varies with the wavelength according to the following equation :

$$S = S_0 \cdot \lambda^{-0.2} \quad (3.19)$$

Where  $\lambda$  is the wavelength. Seeing is defined as the image size (FWHM) in arcsec on a long exposure limited by the atmosphere (ie. telescope without optical aberrations nor dome/mirror seeing) as observed at zenith and at wavelength 0.5 micron. So when DIMM data are collected a correction of these two effects must be done. An extapolation to the zenith and to 0.5 micron wavelenqth.

### 3.3 Exposure Time Dependence

Seeing is caused by turbulent cells in the atmosphere as it is analysed in previous paragraphs. According to the Kolmogorov theory, these cells come in various sizes. Thus, the turbulence-induced phase fluctuation occur at various frequencies, mainly depending on the size of the cells and the windspeed. The important question to be addressed is whether differential image motion

measurements probe the complete frequency power spectrum of the seeing: The images have to “freeze” the image motion, i.e. the exposure time of the images has to be sufficiently lower than the time needed for the air cell to move across the line of sight. If this is not the case, then the seeing caused by the high part of the frequency power spectrum is not measured since high-frequency contributions to the differential image motion are averaged out.

It is thought that much of the seeing is caused by phase fluctuations with frequencies less than a  $100\text{Hz}$ . Therefore, an exposure time of  $10\text{ms}$  should suffice to obtain seeing measurements using differential image motion. Since there is a contribution of phase fluctuation with frequencies between  $50\text{Hz}$  and  $100\text{Hz}$ , it is likely that there is also a contribution with frequencies above  $100\text{Hz}$ . the problem is that  $10\text{ms}$  is the smallest possible exposure time (for technical reasons), so we cannot probe this part of the spectrum. However, considering how well-behaved the power spectrum is up to  $100\text{Hz}$ , one can expect that it is easily possible to scale the seeing measurements of the Dimm to the real seeing by using a single scaling factor.

The temporal averaging of the variance of the differential motion with a finite exposure time  $T$  depends both on the average velocity  $V_0$  and on the direction of the displacement of the wavefront corrugations with respect to the DIMM apertures. The exact computation of this effect (Martin et al., 1987) for a typical experimental setup (distance of the apertures equal to twice their diameter  $d$ ) and typical operating conditions ( $1 < V_0T/d < 5$ ) shows that the differential tilt variance  $\sigma^2$  presents in all cases an exponential dependency on the exposure time  $T$  of the type :

$$\sigma^2(T) = \sigma^2(0)e^{-\alpha T} \quad (3.20)$$

where the coefficient  $\alpha$  is of course unknown and depends on atmospheric conditions. However, performing two simultaneous measurements with exposure times  $T_1$  and  $T_2$  such that  $T_2 = 2T_1$ , the coefficient  $\alpha$  can be eliminated and the bias can be removed by computing :

$$\sigma^2(0) = \frac{[\sigma^2(T_1)]^2}{\sigma^2(T_2)} \quad (3.21)$$

In practice the two variances are calculated over two interlaced time series (Sarazin, 1997) or, when possible, on a single time series by rebinning the individual exposures (Ziad et al., 2000). The amount of correction is naturally site-dependent but often not to be neglected. It was noted by Giovanelli et al. (2001) that, at the northern Chile high-altitude sites, the median values of the 0 ms seeing vary between 0.65 and 0.76 arcsec, those of the 10 ms seeing between 0.56 and 0.65 arcsec while those of the 20 ms seeing between 0.48 and 0.56 arcsec.

## Chapter 4

# Development of a New H-DIMM Unit

### 4.1 Why a new H-DIMM Unit?

#### 4.1.1 Required Characteristics.

1. To be integrated from camera and telescope equipment. This will allow us actually to measure seeing everywhere, using standard amateur equipment.
2. Adequacy of Astronomical Equipment: A telescope, both refractor or reflector at least 6 inch wide, with motor drive for the hour angle and a CCD camera (and NOT a Web-Cam, various Digital Cameras, single frames from Video-Cams etc) is to be considered as adequate astronomical equipment. Variations from the above mentioned equipment (especially Web-Cams) are currently being tested to find out if they can be used in this project. Finally, a special mask (cardboard-made or plastic), which anyone can make, and of course a PC are also needed.
3. Because the data reduction requires special software, which has been written in the Observatory for this specific purpose, the data sent by each amateur astronomer should have some consistency, thus limiting the error possibility and enabling the software to run without problems.

#### 4.1.2 The Seeing-GR Project.

The Seeing-GR is an ambitious new project aiming in measuring and calculating a median value of the true astronomical seeing in Greece. The H-DIMM method is used because it is easy to implemented by anyone. Because the collection of data from all over Greece cannot be undertaken from one person alone or even a single group Seeing-GR is mostly addressed to amateur astronomers

inhabiting both remote places and the metropolitan centers (even in Athens and Thessaloniki), as well. This project (measuring the seeing of a whole country) is unique and has never been done before. Greece is one of the privileged countries as clear skies can be found throughout the year in most places, but also (and most importantly) because it has many well-grounded and adequately equipped amateur astronomers. The data for the project will be gathered from amateur astronomers exclusively and will afterwards be reduced. For these reasons participation in Seeing-GR will ONLY be allowed to amateurs who meet some basic requirements:

## 4.2 Aquisition Software Development.

The acquisition software for the project was righten in Visual Basic. This programming language was chosen because a Windows program needed, in order to be used by anyone. It uses the Windows API interface as well as the ASCOM drivers to comunicate with MaximDL. MaximDL is a CCD camera control software and is used to control the camera and to download the data to the computer.

### 4.2.1 The Program's Interface

The program's interface is quite simple, so even a person with no astronomical knowledge can use it. It has three (3) buttons.

- The "Start DIMM Measurements" button  
This is the main button of the program .With this one we can take DIMM measurements by just pressing it!!
- The "Star's Information" button  
With this one we enter the star's information, meaning the star's name and coordinates. You can't take measurements if you don't enter any information about the star you are observing.
- The "Exit" button  
By pressing this one you quit the program!!

The main body of the program also contains a number of boxes. There are two information boxes, used to display varius information, a box with the download rate, a box with the download time and a box that contains the star that you have selected with the "Star Information" button. In figure 4.2 it is shown the Star details interface. Here you must enter at least the name of the star you are going to observe. If no coordinates entered then this name will be used to find the *Ra* and *Dec* from the official catalogs. Of course you are encouraged for you to enter the celestial coordinates since this will greatly simplify the reduction procces.

Apart from the information concerning the star, there is a button called "New Lat/Lon". This button is ment to be used only if you are observing in a location other than your home location. Your home location is the place you specified in the registracion form. So if you are going to observe

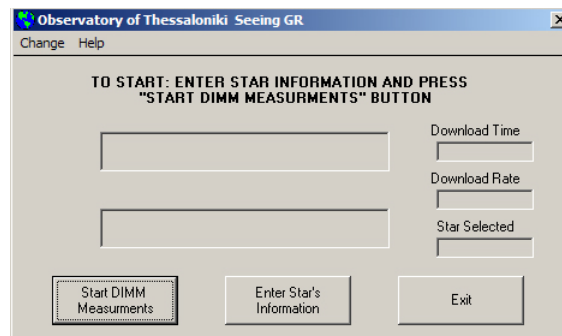


Figure 4.1: The Program's Interface.

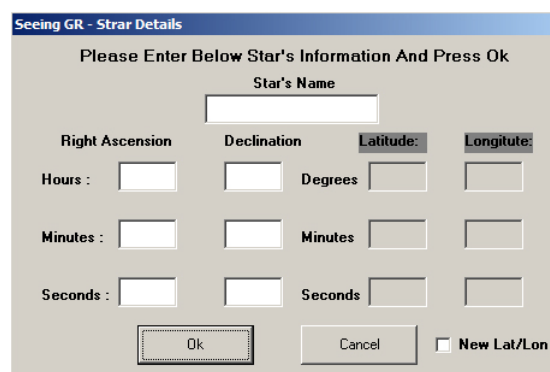


Figure 4.2: The Star Details Interface.

in different place please enter here the coordinates. If you don't know them or you can't find them please enter in all fields "00" and when you will send us the data please attach a file or send us an e-mail giving us detailed information about the place you observed (eg. 20Km south of Lamia, near the village Krania. . . ) so we will be able to find them. In figure 4.3 it is shown the User information dialog. This dialog appears when you run the program for the very first time. Here you must enter the same information as those in the registration form. Please have in mind that a cross-check of these information is run automatically. If information entered in the "User info Dialog" are different from those in the registration form then the data will not be analysed and you will be contacted to sort this out.

The user information dialog can be also accessed from the menu "Change". Please change this information only if it is necessary to do so. Also if you change them please inform us with an e-mail. Remember that such changes must not be frequent!!!

### 4.2.2 Taking Measurements

To take DIMM measurements you must first enter the information of the star that you will be observing, meaning the star's name and its coordinates. If you don't know the exact coordinates,

Figure 4.3: The User Info Dialog.

enter only the star's name, and we will find its coordinates, but it would generally help us if you fill the coordinates yourself. Keep in mind that you **MUST** enter the star's name, before you can start taking measurments. After entering the information needed, it's time to press the "Take DIMM Measurements" button. Only two things are left for you to enter, for the program to run properly. The first thing is the ambient temperature, meaning the temperature of the environment. We need this value for the program to regulate the chip temperature low enough to take measurements. Accepted values are from -20 to +40 Celsius. After you have entered the temperature you must wait until the camera's temperature regulates. A dialog box will appear. If you entered a wrong temperature in the previous step and the camera cannot reach the setpoint, you can correct it here. If you enter nothing, every time you press OK or Cancel you can see how many degrees are left to reach setpoint in the main body of the program. When the setpoint is reached then the next time you press OK you will continue to the next step.

The second thing is the time you want to observe. Here you must enter from 30 min to 10 hours. We have entered this limitation because measurements below 30 min will not be statistically correct. Information boxes will appear, before the actual measurements begin, to tell you what exactly is done with your camera. Nothing else needs to be entered for the program to take DIMM measurements. Trough the whole procedure you can see exactly what the program is doing and how many time is left to complete the run. If you want to run the program again you don't have to close and restart, just press the "Take measurments" button once more.

### 4.2.3 The Output Data

The output data is a series of "FIT" images. You can view these images with programs like MaximDL or CCDOPS, but be careful not to change them in any way! Teasing the contrast or brightness or anything else so that the frame looks nice, will affect the quality of the data!! Apart from the

frames, three other files will be created: one is a statistic of the download time versus time. This file is for us to know if anything went wrong during the download of the frames from the camera to the computer. The second file is the actual log that contains all the information needed to reduce the data and extract the seeing value and the third is information about your equipment and the location you observed. So when you send the data to the Observatory make sure that these three files will be sent as well. The files have extensions “.dat” and “.jbn”. All the “.FIT” frames the “.dat” and the “.jbn” files are stored every time you run the program in a folder like this one :

```
"c:\dimm\data\xx_x_xxxx_x_xx"
```

where the x directory is the date and time you run the script. So every time you run it, a different folder of this type is created. If you run the script five times in a single night then you will have five different folders in your data folder. You will be sending us all these folders for every time you run the program.

#### 4.2.4 Possible Error Messages

There are some errors that you might encounter while running the program. One of those errors is entering a letter when a number is asked. When you make this mistake a dialog will appear informing you of that and telling you that you must start from the beginning. If you have entered the star's information you don't have to re-enter them, just press the "Take Measurements" button again. Some errors occur when you enter a value that it's not within acceptable limits. This type of errors includes observation duration and temperature. The limits for the ambient temperature are from -20 to +40 Celsius. The limits for the observation duration are from 30 minutes to 10 hours. If you enter a value outside these limits a warning will appear, and you must then re-enter a correct value. Other errors include selecting a wrong camera model in the MaximDL list. If that is the case just enter the correct model of your CCD in MaximDL. If your camera does not exist, send an e-mail to the seeing-gr analysis group and tell us about that. We will try to make it work. In case of other errors a dialog box will appear and inform you what to do. In all error cases a fault log is created in the programs folder. If an error persists, please send us an e-mail explaining exactly what you did and came to this difficult position. You should also send us the "fault.log" file mentioned above.

### 4.3 Reduction Software Development.

For the acquired data to be analyzed new code must be written. This was done in Linux using C-Shell programming, Fortran and Starlink routines such as Photom, Figaro and Kappa.

## Chapter 5

# Scintillation Measurements with the H-DIMM

*”Twinkle Twinkle Little Star...”*

Scintillation is an important factor in measurements requiring high precision photometry (extra-solar planet detection), astrometry, and of objects with very fast intensity changes (astroseismology). Below are presented scintillation measurements made in mount Xolomon in Chalkidiki Greece. I present the theory of the method used. As a by-product of the scintillation measurements an estimate of the isoplanatic angle is done for the same observing site.

The “amount” of scintillation can be measured by the variance  $\sigma_i^2$  of the relative fluctuations in intensity  $I$ ,  $\sigma_i$  being the root-mean-square value of  $(I - \langle I \rangle) = \Delta I / \langle I \rangle$  where  $\langle \rangle$  denotes time average. In the literature,  $\sigma_i^2$  is often called the “scintillation index” (although that expression has been used also for the rms modulation of  $I$  itself). To avoid ambiguity, for  $\sigma_i^2$  we will use the term ‘intensity variance.’ The ‘rate’ of scintillation can be measured by the width of the temporal correlation function or, equivalently, by its Fourier transform, the power spectrum. Especially in older literature, the “frequency” of scintillation expresses how often the fluctuating intensity crosses its average value.

The values for intensity variance  $\sigma_i^2$  refer to the variance of the linear quantity. In some publications, the variance is instead given for the logarithm of intensity, the relation being  $\sigma_i^2 = [\exp(\sigma_{\ln(i)}^2) - 1]$ . For small scintillation amplitudes the difference is negligible. A refractive-index undulation in the atmosphere acts as a lens, focusing the starlight. The illumination of a screen (pupil plane) at some distance from such a lens varies from place to place because alternate sections of the lens are converging and diverging. Scintillation involves a geometrical “lever-arm” effect, since the wave front wiggles must be sufficiently distant to produce brightness changes. Scintillation is normally dominated by turbulence at high altitudes (many kilometers), while seeing often has significant components originating close to the telescope.

When the turbulence causing the refractive fluctuations is at a great distance from the telescope, the irradiance becomes variable in both space and time. This intensity modulation can be observed in short-exposure images of a telescope mirror illuminated by a bright star, as a system of rapidly moving “shadows”. With the unaided eye, such “flying shadows” can be glimpsed during the moments before and after a total solar eclipse, when an uneclipsed solar crescent acts as the light source. Then the ‘shadows’ appear as elongated ‘bands’ because of the anisotropic brightness distribution of the solar crescent.

Their motions are determined by wind components at various contributing altitudes. However, in contrast to solar eclipse phenomena, shadow patterns from stars are statistically isotropic. Scintillation may be studied either by measuring the fluctuations in image intensity, or by measuring the shadow pattern directly. The intensity of the telescopic image depends upon the sample of the shadow pattern selected by the telescope at any instant. Temporal variations occur for two main reasons. Firstly, the shadow pattern moves across the detector as the region of atmosphere producing the pattern is carried by the wind.

Most modeling indeed assumes that this pattern can be regarded as frozen in the atmosphere (Taylor’s approximation), merely swept by winds across the telescope aperture. However, fluctuations also occur when the structure of the shadow pattern varies due to changes in the turbulence, or due to the relative motion of different regions of the atmosphere. Detailed studies of the spatio-temporal properties of scintillation for single and binary stars can be used to deduce quite detailed information about the often layered structure in the upper atmosphere. In order to ‘fully’ resolve the atmospheric effects, it is necessary to limit the size of the telescope pupil, the spectral bandwidth of the detector, and the sample time of the processing equipment. Aperture averaging will reduce the variance unless the telescope aperture is significantly smaller than the smallest feature size in the shadow pattern.

Thus a measure of the variance as a function of aperture size gives an estimate of these feature sizes. Different extents of the sampling aperture, and of the temporal integration, preferentially ‘filter’ out differently distant turbulence elements. For example, naked-eye twinkling ( $\sim 5mm$  aperture, a cutoff for frequencies above  $15Hz$ ), arises mostly from turbulence within  $1km$  of the ground.

## 5.1 Measurement Technique

In theory, the fluctuations of the normal logarithm of the light intensity is the quantity to compute. So, if  $x$  and  $y$  are the intensities in two apertures, the normal scintillation index  $s_x$ ,  $s_y$  and the differential index  $s_{xy}$  should be computed as :

$$\begin{aligned} s_x &= \left\langle (\log x - \overline{\log x})^2 \right\rangle \\ s_y &= \left\langle (\log y - \overline{\log y})^2 \right\rangle \end{aligned} \quad (5.1)$$

and

$$s_{xy} = \left\langle (\log(x/y) - \overline{\log(x/y)})^2 \right\rangle \quad (5.2)$$

In fact, the calculations are done by different formulae that replace logarithms with ratios. These "linear" formulae are better suited for the subtraction of photon noise because the latter can be evaluated theoretically. The photon noise can be quite large, so the use of logarithmic formulae for index calculation seems problematic. The linear one are :

$$\begin{aligned} s_x &= \left\langle (x/\bar{x})^2 \right\rangle - 1 \\ s_y &= \left\langle (y/\bar{y})^2 \right\rangle - 1 \end{aligned} \quad (5.3)$$

and

$$s_{xy} = \left\langle (x/\bar{x} - y/\bar{y})^2 \right\rangle \quad (5.4)$$

The above equations are used in the reduction software to calculate the various scintillation indexes. For the measurements of the intensity of light in the two apertures, packages from Starlink are used such as *Photom* and *Extractor*. The reduction code is in the addendum.

### 5.1.1 Correcting for Zenith-Distance

Stars near the horizon scintillate with greater amplitude but more slowly than stars near zenith this causes the low-frequency naked-eye twinkling to become prominent near the horizon. This zenith distance dependence has been measured by Bufton and Genatt (1971), Darchiya (1966), Diamant et al.(1969). Although the scintillation increases away from zenith, the increase does not continue until the very horizon. Typically, the amplitude increases until around  $Z=60^\circ$  or  $70^\circ$ , where it saturates (or even decreases). The saturation angle depends on the airmass traversed, and may differ between low and high altitude sites. Only a few studies at extreme zenith distances seem to exist, e.g. Butler (1952) who recorded scintillation at an elevation of only  $1^\circ$  above the horizon. More subtle effects include the aperture-size dependence for the saturation angle, being closer to zenith for smaller telescope apertures. Further, the validity of a log-normal distribution seems to become weaker with increasing zenith distance.

Theories have been developed in the wave-optical treatment by Tatarski (1961), and in the geometrical optics one by Reiger (1963). Although different in other aspects, these agree on the zenith angle dependence,  $(\sec Z)^3$ , for large apertures. The concepts are discussed by Bufton (1973) and Parry et al. (1979). In the case of wave-optics (small apertures) a dependence  $\sigma_i^2 \propto (\sec Z)^{11/6}$ , and in the geometrical optics case (large apertures)  $\sigma_i^2 \propto (\sec Z)^3$ . To account for saturation at large zenith angles, Young (1969, 1970a, b) showed how effects of seeing and color dispersion cause deviations from this  $(\sec Z)^3$  dependence, light traversing large airmasses is spread out laterally, thus providing spatial averaging. The zenith distance dependence of the scintillation index  $\sigma_i^2$  can be numerically modeled under certain assumptions. The results show how  $\sigma_i^2$  increases until some

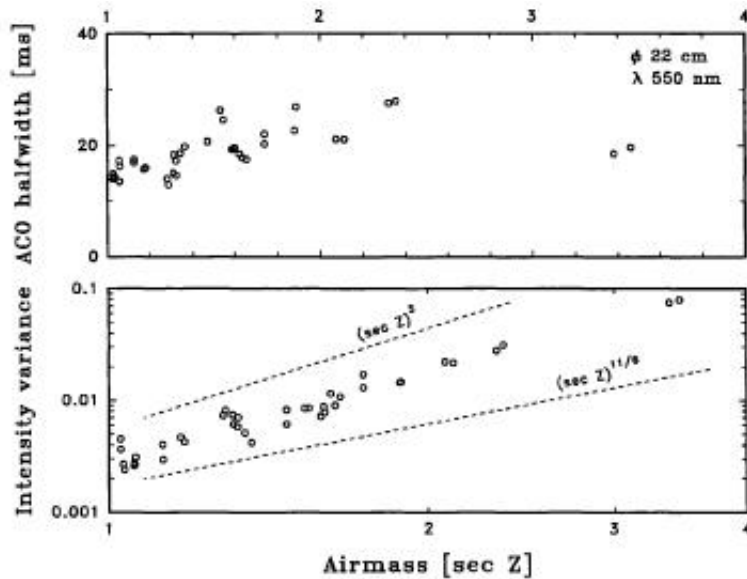


Figure 5.1: Scintillation amplitudes and time scales increase with zenith distance. Upper curve for large aperture and down for small aperture. Measured with a 22cm aperture.

zenith angle, then saturates and finally decreases near the horizon. Here of course because of the small aperture telescopes used the assumption is  $\sigma_i^2 \propto (secZ)^{11/6}$ .

## 5.2 Estimate Of The Isoplanatic Angle Through the Scintillation Index

Almost all modern large telescopes are now being equipped with Adaptive Optics (AO) systems to compensate turbulence and to push the resolution to the diffraction limit at least at near-infrared wavelengths (Roddier, 1999). Good atmospheric seeing is even more critical to the AO operation than it is for classical seeing-limited observing. Moreover, atmospheric time constant  $\tau_0$  and isoplanatic patch size  $\theta_0$  are additional parameters which need to be known. Ideally, the vertical turbulence profile should also be monitored to assist AO operation. The time constant can be calculated with the theory presented in 2.1.2

The isoplanatic angle  $\theta_0$  can be estimated from the fluctuations of stellar flux received by the DIMM subapertures and caused by scintillations. It has been noted already by Loos & Hogge (1979) that the scintillation index in a 10-cm aperture can lead to an approximate estimation of  $\theta_0$ . Again, because of the too long exposure time of current DIMMs, the scintillation index is generally reduced by time averaging. However, this bias can be calculated providing that one has some real-time knowledge of the temporal spectrum of the scintillation.

Scintillation index  $s$  is defined as a variance of the natural logarithm of the light intensity

received by an aperture of the instrument. A theory of light propagation through atmosphere (Rodier, 1981) in the limit of faint perturbations relates the index to the vertical profile of the refractive index structure constant  $C_n^2(h)$  :

$$s = \int_0^{Z_{max}} C_n^2(z)W(z)dz \quad (5.5)$$

where the integration over range  $z = h \cos \gamma$  is performed from the aperture ( $z = 0$ ) to the maximum distance of turbulence,  $Z_{max}$ . The weighting function  $W(z)$  depends on turbulence spectrum, wavelength  $\lambda$ , and aperture shape. For finite exposure time  $\tau$ ,  $W(z)$  is modified, because the "effective" aperture is extended in the wind direction by  $V(h)\tau$ , where  $V(h)$  is the horizontal wind velocity at the altitude  $h$  above the observing site. Thus, a finite exposure time introduces the bias  $R(\tau) = s(\tau) = s(0)$  in the measured scintillation index, which can be computed from the vertical profiles  $C_n^2(h)$  and  $V(h)$  (Tokovinin, 2001). The isoplanatic angle  $\theta_0$  at zenith (Fried, 1982) is defined as :

$$\theta_0^{-5/3} = 2.91(2\pi/\lambda)^2 \int_0^{H_{max}} h^{5/3} C_n^2(h) \quad (5.6)$$

Loos & Hogge (1979) noted the similarity of equation 5.6 with equation 5.5, and suggested that  $\theta_0$  can be derived from the scintillation index if the weighting function is roughly proportional to  $h^{5/3}$ . For an aperture of about 10 cm in diameter and for  $\lambda = 0.5\mu m$  the approximation  $W(z) \propto z^{5/3}$  holds well at altitudes around 10 km, which mostly contribute to scintillation. We calculate the isoplanatic angle (at zenith and at  $0.5\mu m$ ) from the scintillation index  $s$  measured at zenith angle  $\gamma$  by the equation :

$$\theta_0 = As^{-3/5}(\cos \gamma)^{-8/5} \quad (5.7)$$

It is not clear, however, which value of the ratio  $W(z) = z^{5/3}$  should be selected to compute the calibration constant  $A$ , and how this constant depends on  $\lambda$  in an analytical manner. From various observations that M. Sarazin, & A. Tokovinin performed, calculated a value of  $A = 0.182''$  for a wavelength  $\lambda = 0.5\mu m$  and this value is used here.

## Chapter 6

# Observations And Results On Mt.Holomon

*“Observing is Like Christmas ... Most of the Time is Cold and at the Same Time Like Home!!!”*

Below follows all the observations that were contacted by me from 2004 to 2006 concerning Seeing, Scintillation and Isoplanatic Angle measurements. All observations were made with a 8-inch Vixen Visac telescope equipped with a hartmann mask and an SBIG ST4 CCD camera. The Hartmann mask had two holes of 5cm each with a separation of 10cm between them. This System along with the ESO control and reduction software is the first H-DIMM unit of the Aristotle University of Thessloniki. A picture of the complete setup is shown at figure 6.1. Also at table 6.1 the properties of the SBIG ST4 CCD camera is shown.

The reduction of the data was made with new software that developed for this purpose. It is written in C-shell and Fortran. The data was airmass corrected. Also this software made the statistical analysis. The diagrams were then produced with the help of Origin in the Windows

<b>Characteristic</b>	<b>Value</b>
A/D Converter	8 bits
A/D Gain	$150e^-/ADU$
Read Noise	$150e^-/RMS$
Pixel Digitization Rate	100 kHz
Pixel Size	13.75 x 16 microns
Dark Current	$250e^-/pixel/sec$ at $0^{\circ}C$
Pixel Array	192 x 164 pixels, 2.6 x 2.6 mm

Table 6.1: SBIG ST4 CCD Camera Characteristics



Figure 6.1: The Vixen Telescope Along with the ST4 CCD Camera.

operating system. For the scintillation measurements in the data obtained by the SSO DIMM, the values of intensity were computed by the camera control and acquisition software. This of course is not a problem, since i don't use absolute values but only relative.

## 6.1 Seeing, Scintillation and Isoplanatic Angle Curves

Below it is presented all the observations that are made to mount Xolomon by me, for this project, for the period of 2004 to 2006. For every night it is presented three diagrams, one for seeing, one for scintillation and one for isoplanatic angle. Also it is given statistical values for every night, like mean values St. Deviation, median value and the value for weach the 75% of the observations are better from the total sample (P75).

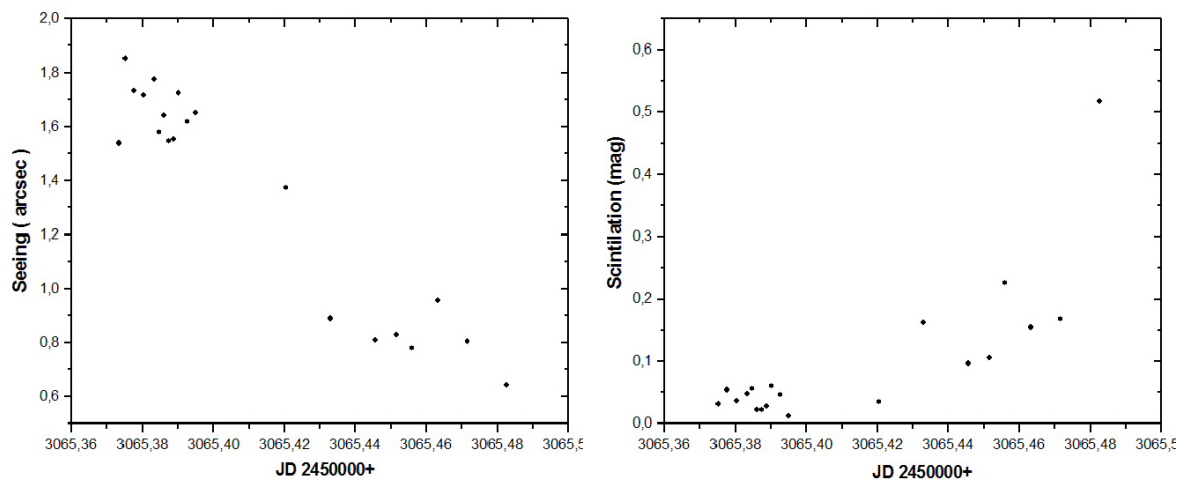


Figure 6.2: Diagrams of Seeing and Scintilation for the night of 29/02/2004

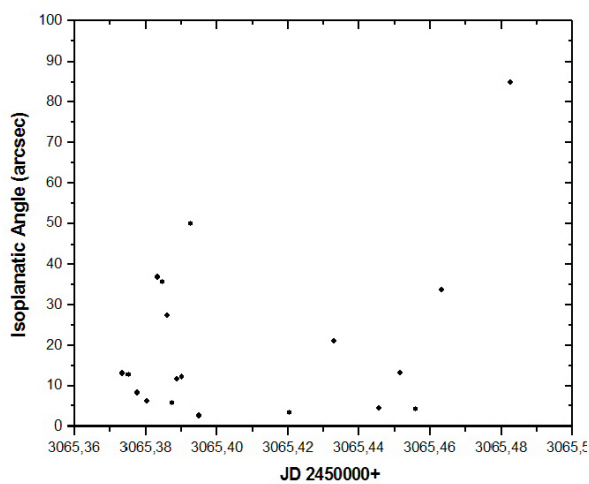


Figure 6.3: Diagram of Isoplanatic Angle for the night of 29/02/2004

Here it is presented the night of 29/02/2004. In figure 6.2 it is shown the diagrams of seeing and scintilation and in figure 6.3 is the diagram of isoplanatic angle. For this night the statistics are :

	Mean	St. Deviation	P75	Median
Seeing (arcsec)	1.35	0.41	1.65	1.54
Scintilation (mag)	0.098	0.11	0.15	0.053
Isoplanatic Angle (arcsec)	27.99	39.64	33.6	12.9

This particular night was not very good for seeing and neither for scintilation.

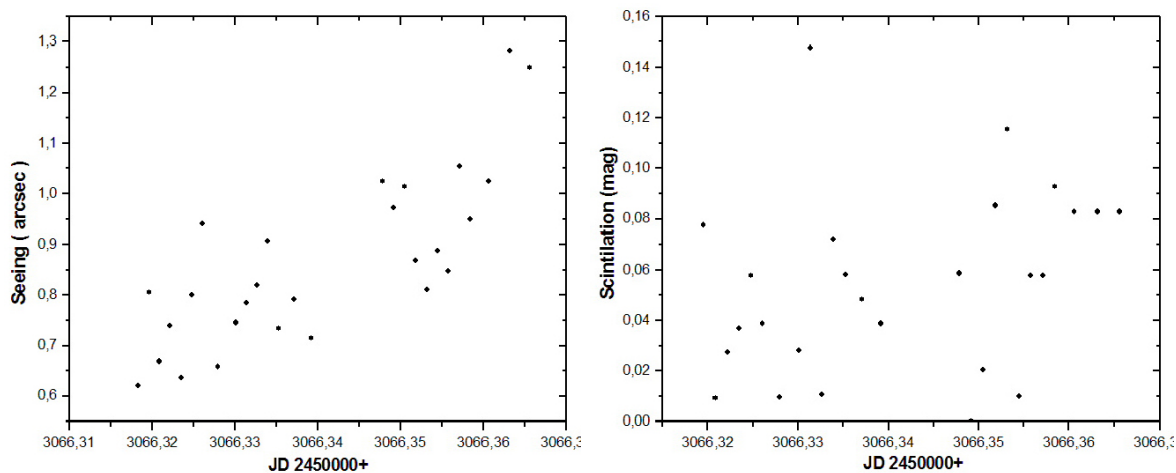


Figure 6.4: Diagrams of Seeing and Scintilation for the night of 01/03/2004

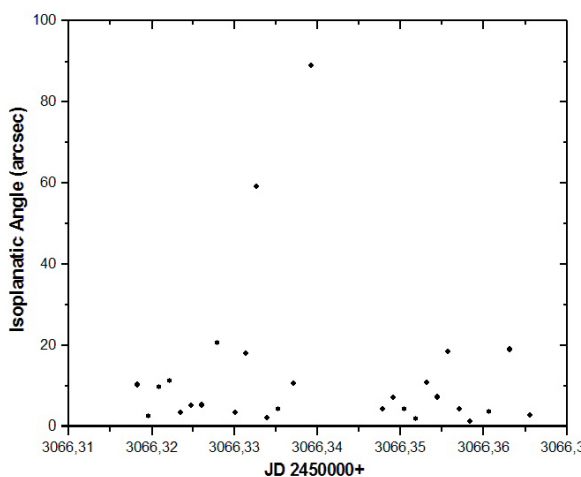


Figure 6.5: Diagram of Isoplanatic Angle for the night of 01/03/2004

Here it is presented the night of 01/03/2004. In figure 6.4 it is shown the diagrams of seeing and scintilation and in figure 6.5 is the diagram of isoplanatic angle. For this night the statistics are :

	Mean	St. Deviation	P75	Median
Seeing (arcsec)	0.86	0.16	0.97	0.81
Scintilation (mag)	0.054	0.036	0.082	0.057
Isoplanatic Angle (arcsec)	12.51	19.09	11.11	5.18

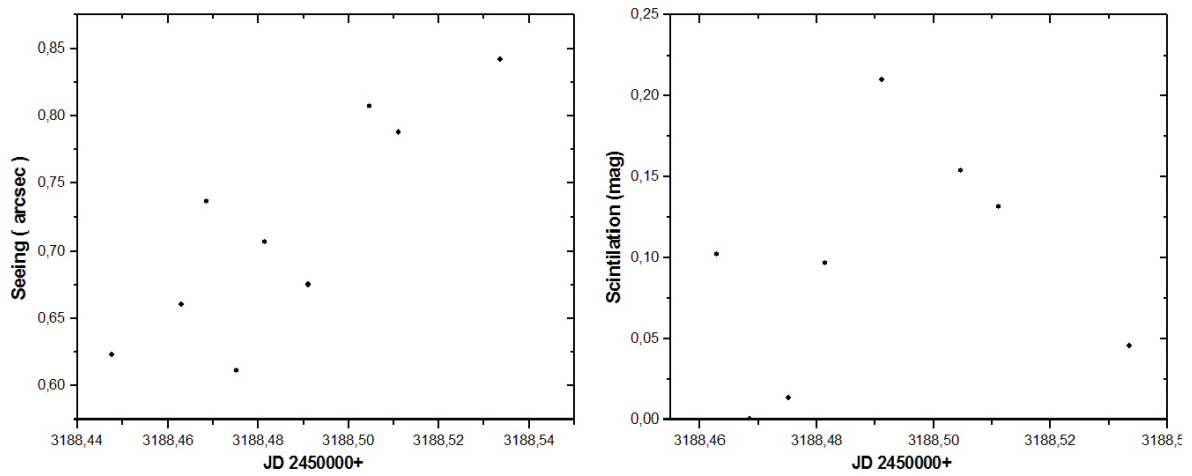


Figure 6.6: Diagrams of Seeing and Scintillation for the night of 01/07/2004

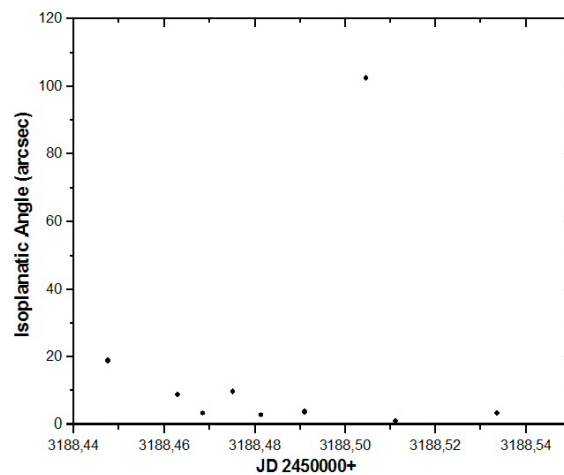


Figure 6.7: Diagram of Isoplanatic Angle for the night of 01/07/2004

Here it is presented the night of 01/07/2004. In figure 6.6 it is shown the diagrams of seeing and scintillation and in figure 6.7 is the diagram of isoplanatic angle. For this night the statistics are :

	Mean	St. Deviation	P75	Median
<b>Seeing (arcsec)</b>	0.71	0.08	0.78	0.7
<b>Scintillation (mag)</b>	0.094	0.071	0.13	0.09
<b>Isoplanatic Angle (arcsec)</b>	17.09	32.5	9.7	3.62

A typical night of good seeing for Xolomon.

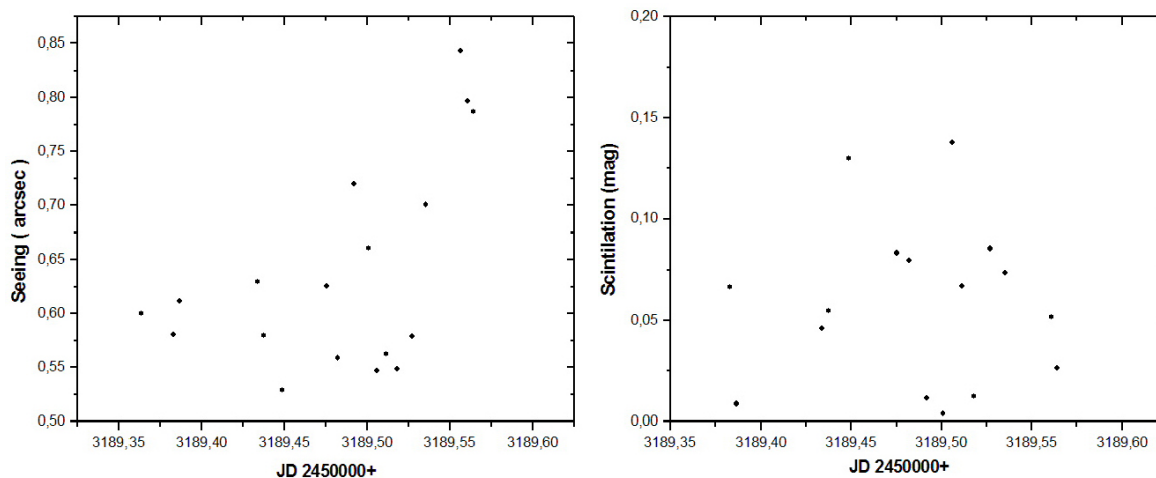


Figure 6.8: Diagrams of Seeing and Scintilation for the night of 02/07/2004

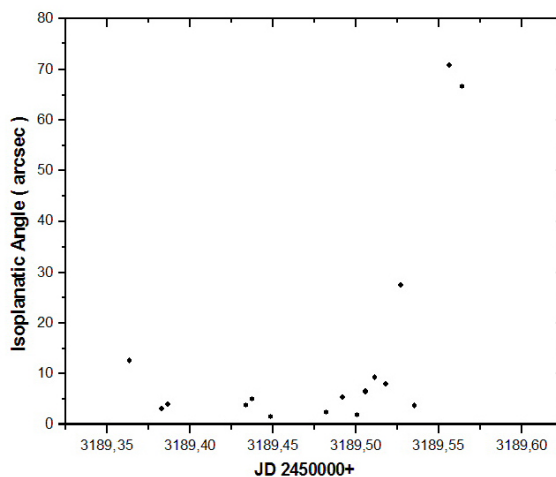


Figure 6.9: Diagram of Isoplanatic Angle for the night of 02/07/2004

Here it is presented the night of 02/07/2004. In figure 6.8 it is shown the diagrams of seeing and scintilation and in figure 6.9 is the diagram of isoplanatic angle. For this night the statistics are :

	Mean	St. Deviation	P75	Median
Seeing (arcsec)	0.63	0.09	0.7	0.6
Scintilation (mag)	0.058	0.04	0.079	0.06
Isoplanatic Angle (arcsec)	14.45	22.13	9.22	5.07

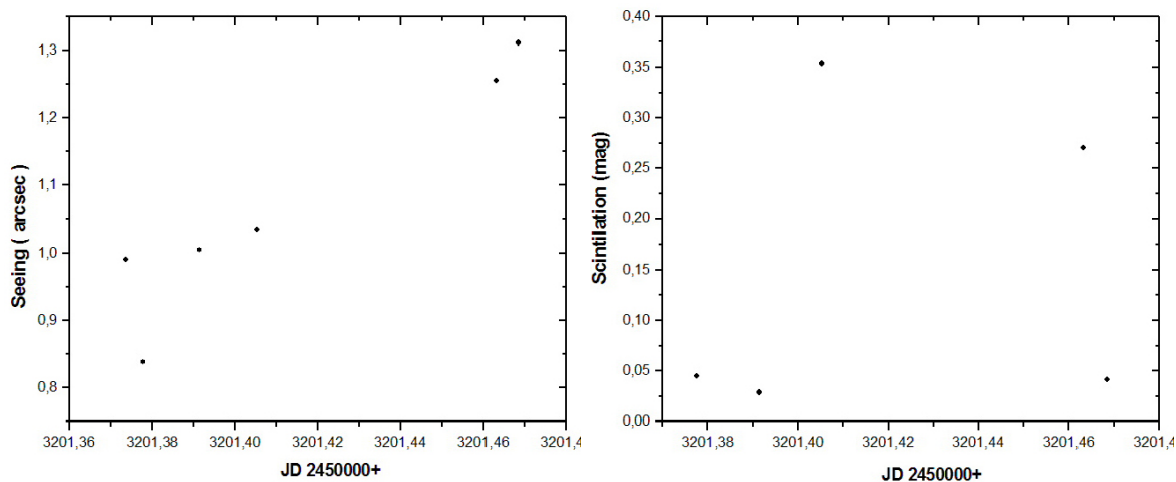


Figure 6.10: Diagrams of Seeing and Scintillation for the night of 14/07/2004

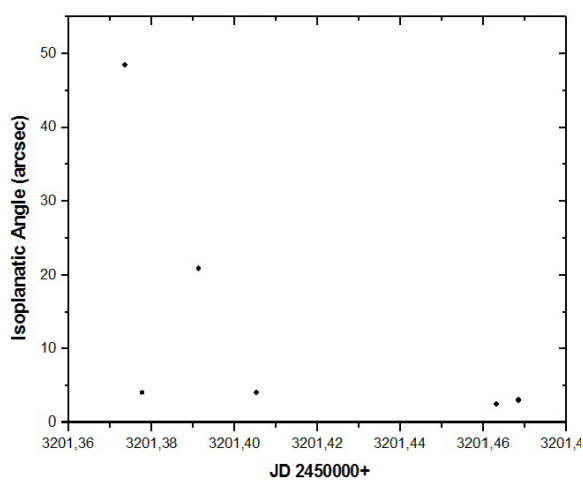


Figure 6.11: Diagram of Isoplanatic Angle for the night of 14/07/2004

Here it is presented the night of 14/07/2004. In figure 6.10 it is shown the diagrams of seeing and scintillation and in figure 6.11 is the diagram of isoplanatic angle. For this night the statistics are :

	Mean	St. Deviation	P75	Median
<b>Seeing (arcsec)</b>	1.07	0.17	1.25	1.01
<b>Scintillation (mag)</b>	0.14	0.15	0.27	0.04
<b>Isoplanatic Angle (arcsec)</b>	13.77	18.39	20.88	3.97

This night had not very good seeing and neither scintillation.

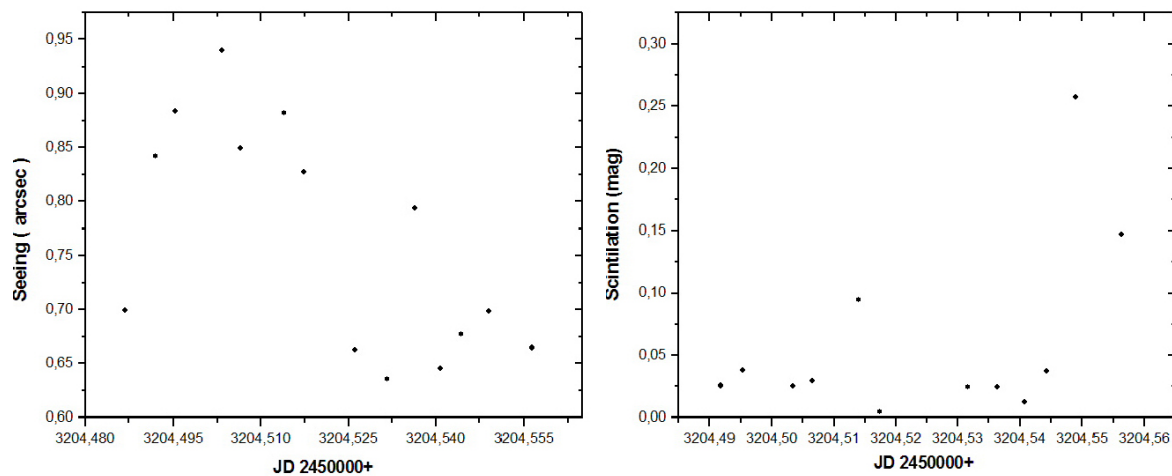


Figure 6.12: Diagrams of Seeing and Scintilation for the night of 17/07/2004

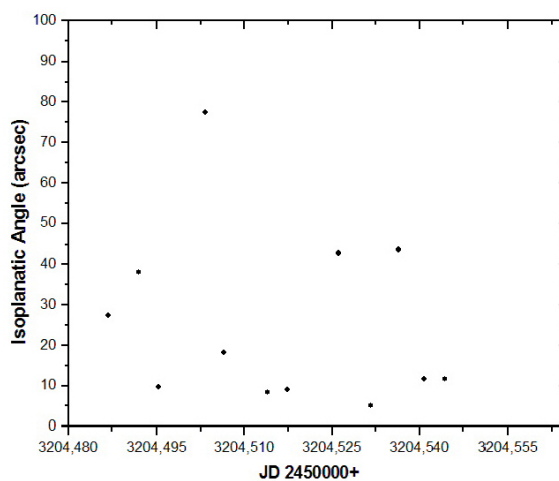


Figure 6.13: Diagram of Isoplanatic Angle for the night of 17/07/2004

Here it is presented the night of 17/07/2004. In figure 6.12 it is shown the diagrams of seeing and scintilation and in figure 6.13 is the diagram of isoplanatic angle. For this night the statistics are :

	Mean	St. Deviation	P75	Median
Seeing (arcsec)	0.76	0.1	0.84	0.74
Scintilation (mag)	0.059	0.073	0.03	0.027
Isoplanatic Angle (arcsec)	77.54	169	43.65	22.78

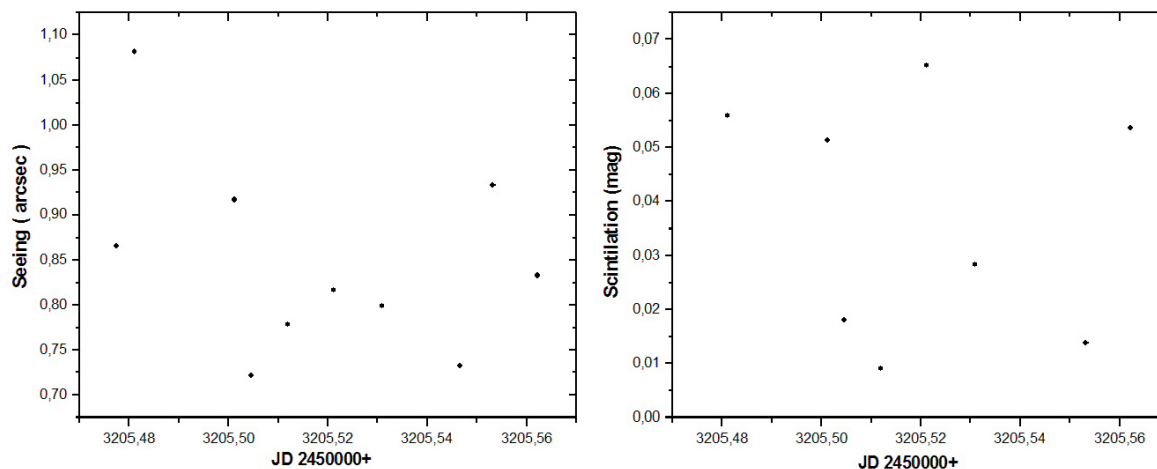


Figure 6.14: Diagrams of Seeing and Scintilation for the night of 18/07/2004

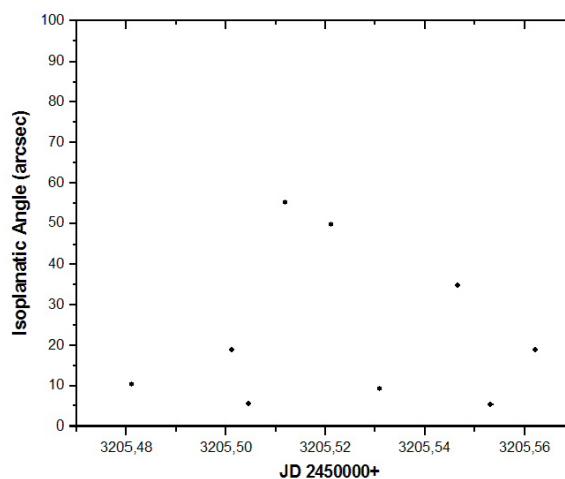


Figure 6.15: Diagram of Isoplanatic Angle for the night of 18/07/2004

Here it is presented the night of 18/07/2004. In figure 6.14 it is shown the diagrams of seeing and scintilation and in figure 6.15 is the diagram of isoplanatic angle. For this night the statistics are :

	Mean	St. Deviation	P75	Median
Seeing (arcsec)	0.84	0.1	0.91	0.82
Scintilation (mag)	0.03	0.02	0.053	0.039
Isoplanatic Angle (arcsec)	83.54	192	49.63	18.86

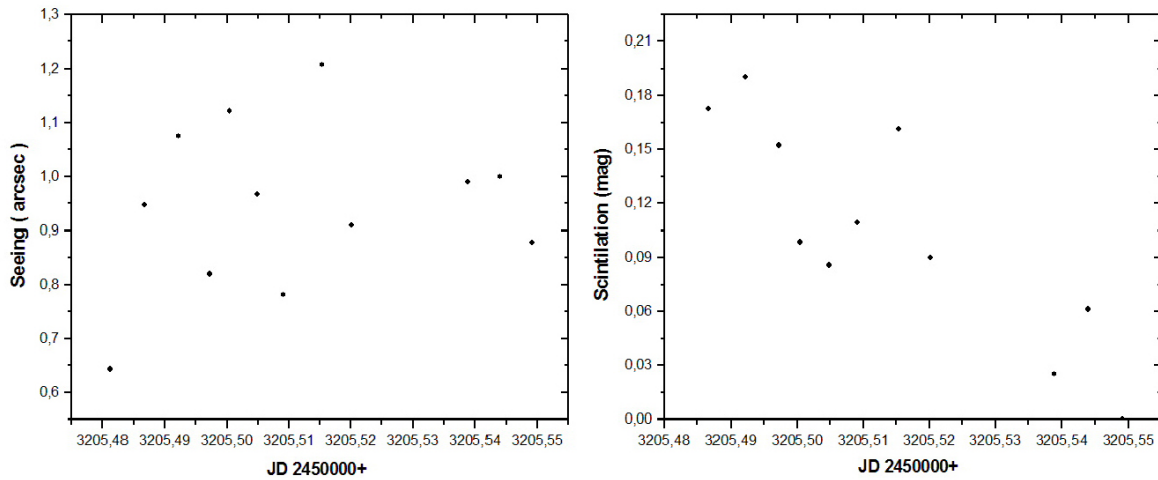


Figure 6.16: Diagrams of Seeing and Scintillation for the night of 19/07/2004

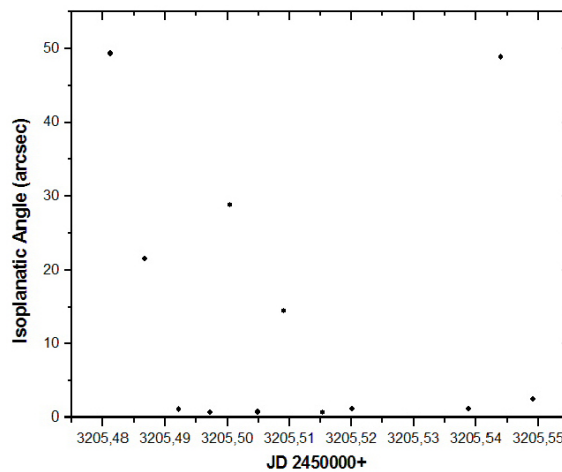


Figure 6.17: Diagram of Isoplanatic Angle for the night of 19/07/2004

Here it is presented the night of 19/07/2004. In figure 6.16 it is shown the diagrams of seeing and scintillation and in figure 6.17 is the diagram of isoplanatic angle. For this night the statistics are :

	Mean	St. Deviation	P75	Median
Seeing (arcsec)	0.94	0.15	0.99	0.95
Scintillation (mag)	0.1	0.06	0.16	0.098
Isoplanatic Angle (arcsec)	14.22	18.86	21.53	1.76

In this too there are too few points to conclude safely about seeing behaviour.

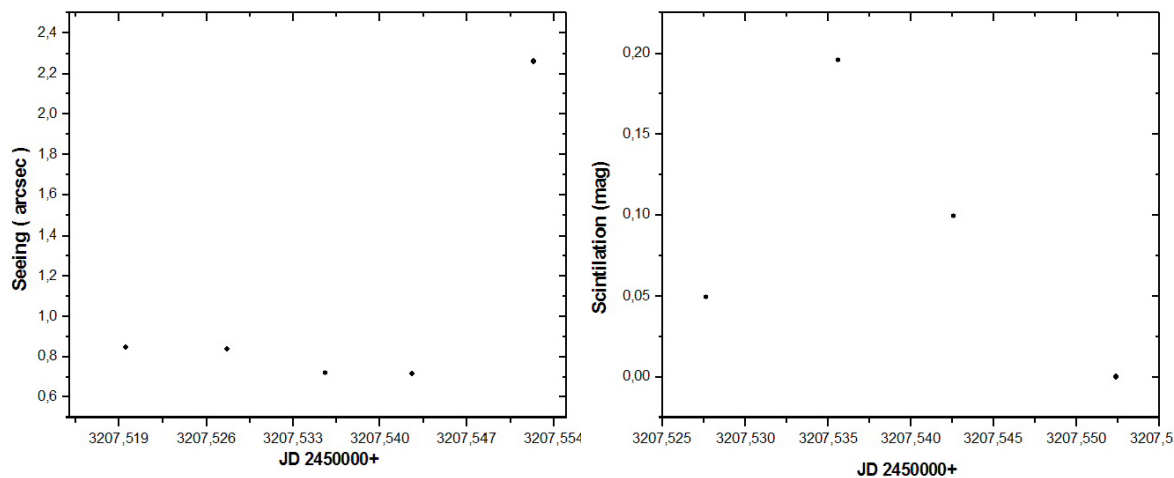


Figure 6.18: Diagrams of Seeing and Scintilation for the night of 20/07/2004

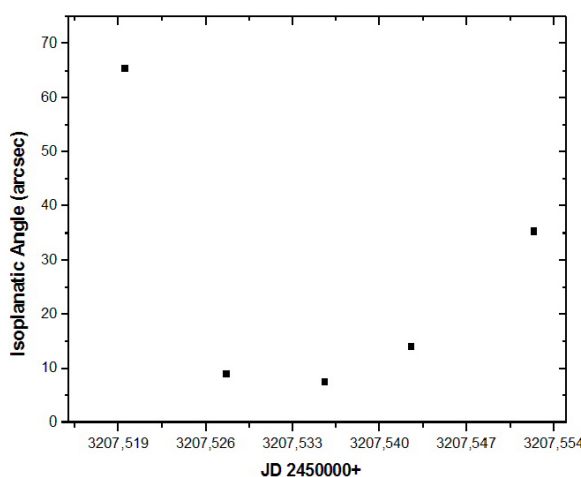


Figure 6.19: Diagram of Isoplanatic Angle for the night of 20/07/2004

Here it is presented the night of 20/07/2004. In figure 6.18 it is shown the diagrams of seeing and scintilation and in figure 6.19 is the diagram of isoplanatic angle. For this night the statistics are :

	Mean	St. Deviation	P75	Median
Seeing (arcsec)	1.07	0.66	0.84	0.83
Scintilation (mag)	0.086	0.083	0.099	0.074
Isoplanatic Angle (arcsec)	26.24	24.66	35.36	14.01

In this night there are too few observations to safely conclude about the behaviour of seeing.

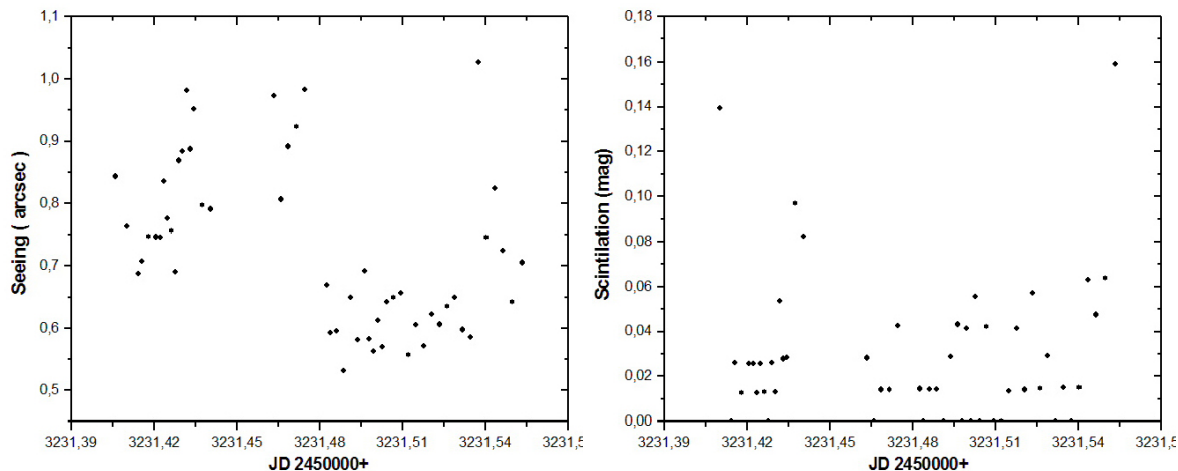


Figure 6.20: Diagrams of Seeing and Scintilation for the night of 12/08/2004

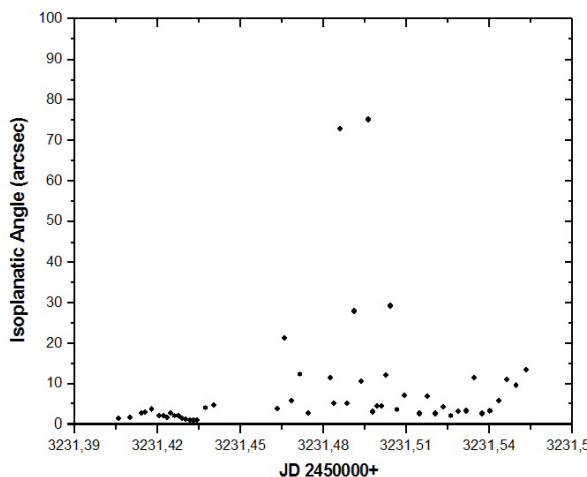


Figure 6.21: Diagram of Isoplanatic Angle for the night of 12/08/2004

Here it is presented the night of 12/08/2004. In figure 6.20 it is shown the diagrams of seeing and scintilation and in figure 6.21 is the diagram of isoplanatic angle. For this night the statistics are :

	Mean	St. Deviation	P75	Median
Seeing (arcsec)	0.75	0.13	0.80	0.69
Scintilation (mag)	0.029	0.033	0.042	0.015
Isoplanatic Angle (arcsec)	11.37	24.91	9.55	3.74

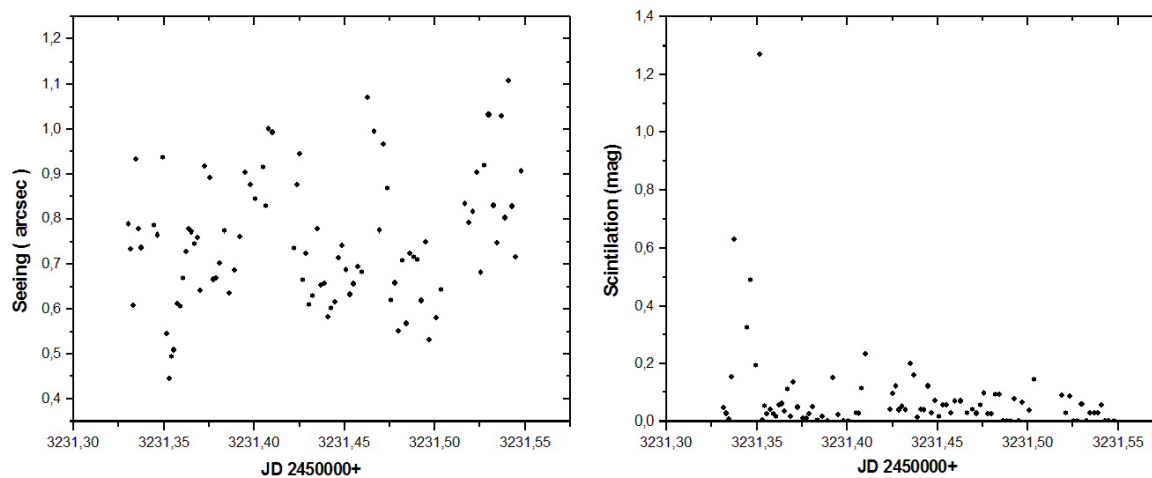


Figure 6.22: Diagrams of Seeing and Scintillation for the night of 13/08/2004

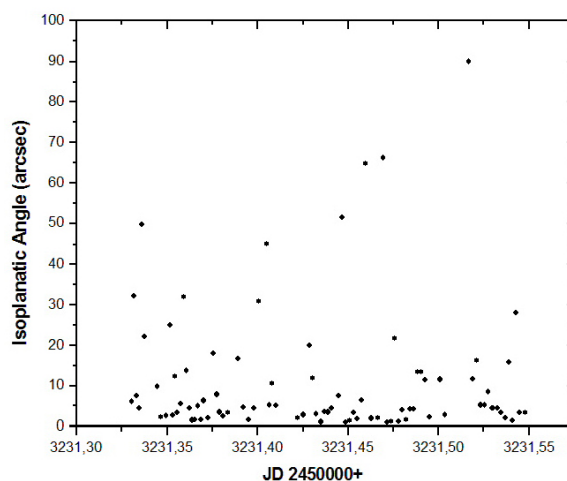


Figure 6.23: Diagram of Isoplanatic Angle for the night of 13/08/2004

Here it is presented the night of 13/08/2004. In figure 6.22 it is shown the diagrams of seeing and scintillation and in figure 6.23 is the diagram of isoplanatic angle. For this night the statistics are :

	Mean	St. Deviation	P75	Median
Seeing (arcsec)	0.75	0.13	0.83	0.73
Scintillation (mag)	0.079	0.16	0.078	0.039
Isoplanatic Angle (arcsec)	23.67	47.16	15.88	4.98

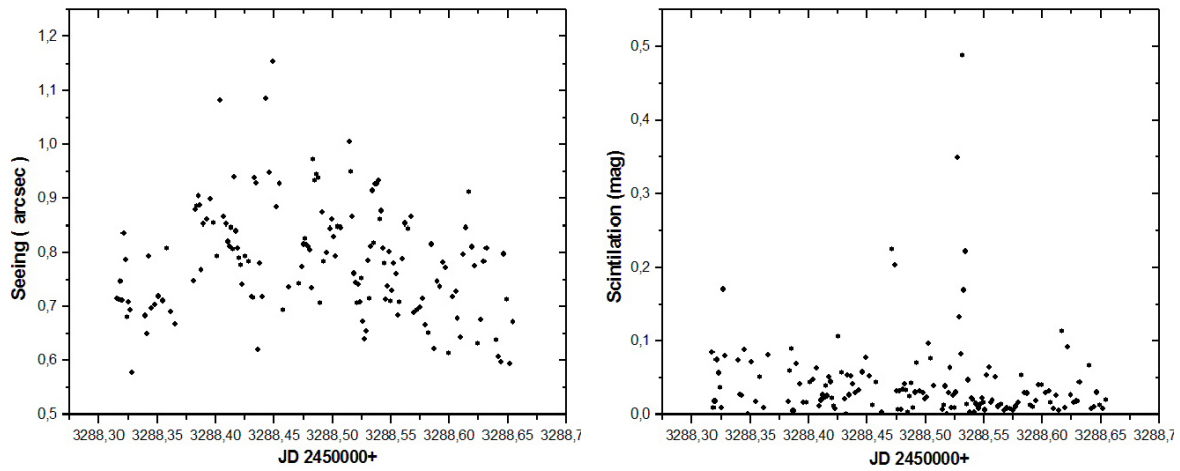


Figure 6.24: Diagrams of Seeing and Scintillation for the night of 09/10/2004

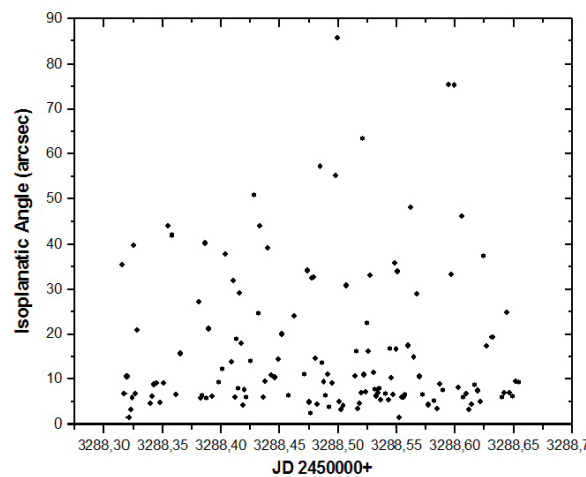


Figure 6.25: Diagram of Isoplanatic Angle for the night of 09/10/2004

Here it is presented the night of 09/10/2004. In figure 6.24 it is shown the diagrams of seeing and scintillation and in figure 6.25 is the diagram of isoplanatic angle. For this night the statistics are :

	Mean	St. Deviation	P75	Median
<b>Seeing (arcsec)</b>	0.78	0.1	0.84	0.78
<b>Scintillation (mag)</b>	0.043	0.05	0.05	0.02
<b>Isoplanatic Angle (arcsec)</b>	41.13	110.3	33.26	10.73

This night was just good and nothing more as far seeing.

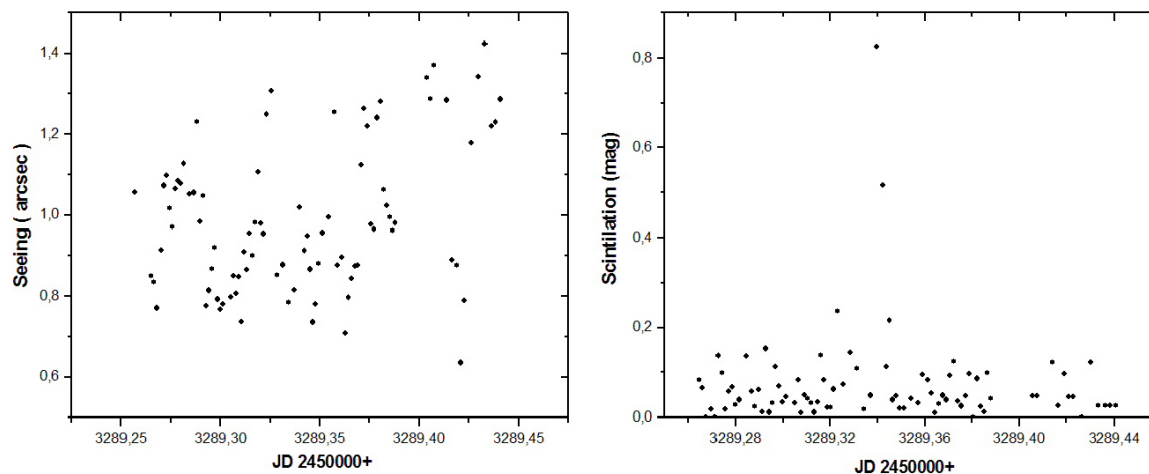


Figure 6.26: Diagrams of Seeing and Scintilation for the night of 10/10/2004

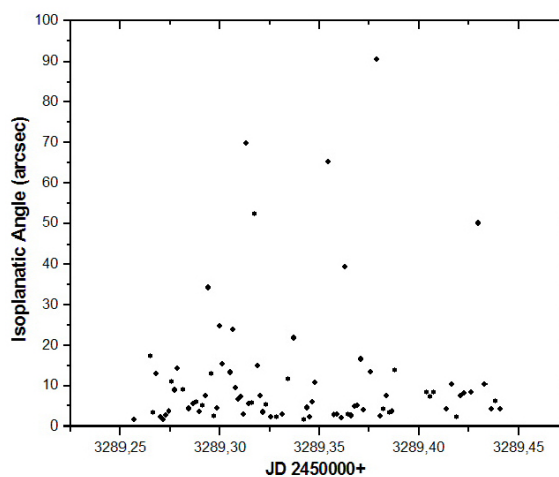


Figure 6.27: Diagram of Isoplanatic Angle for the night of 10/10/2004

Here it is presented the night of 10/10/2004. In figure 6.26 it is shown the diagrams of seeing and scintilation and in figure 6.27 is the diagram of isoplanatic angle. For this night the statistics are :

	Mean	St. Deviation	P75	Median
Seeing (arcsec)	0.98	0.18	1.09	0.96
Scintilation (mag)	0.072	0.1	0.08	0.04
Isoplanatic Angle (arcsec)	30.49	100.21	13.9	7.33

This night was not good for the standards of Xolomon, with an increasing tendency during the night. Even scintilation was not so good.

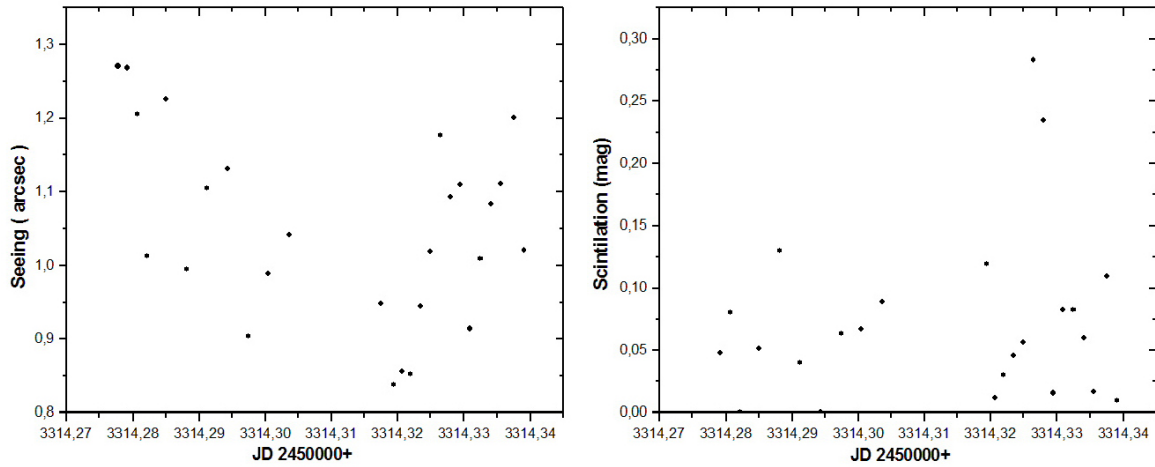


Figure 6.28: Diagrams of Seeing and Scintillation for the night of 04/11/2004

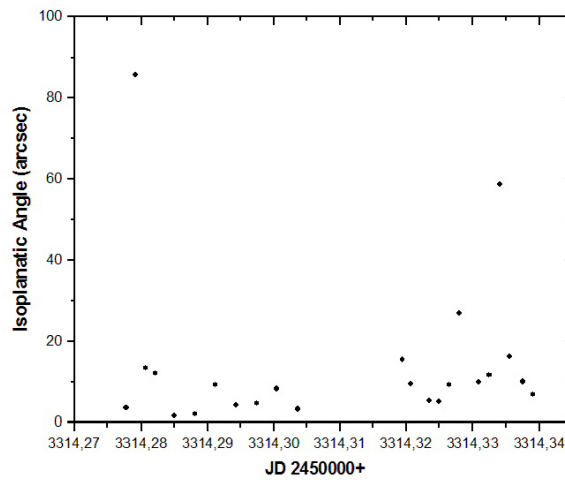


Figure 6.29: Diagram of Isoplanatic Angle for the night of 04/11/2004

Here it is presented the night of 04/11/2004. In figure 6.28 it is shown the diagrams of seeing and scintillation and in figure 6.29 is the diagram of isoplanatic angle. For this night the statistics are :

	Mean	St. Deviation	P75	Median
Seeing (arcsec)	1.05	0.12	1.13	1.03
Scintillation (mag)	0.007	0.068	0.082	0.058
Isoplanatic Angle (arcsec)	14.44	19.5	13.29	9.29

Unfortunately in this night there are not too many observations and that's why we can not have safe statistical conclusions.

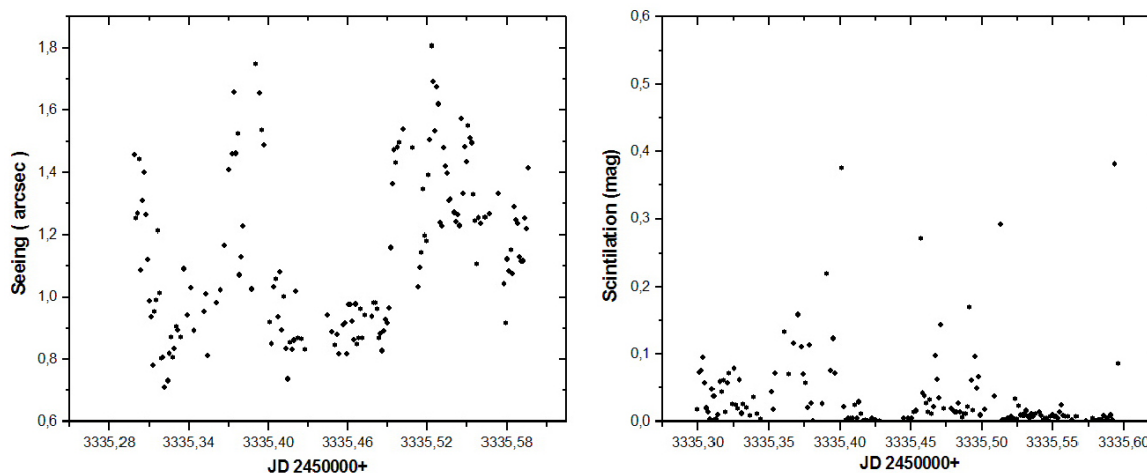


Figure 6.30: Diagrams of Seeing and Scintilation for the night of 25/11/2004

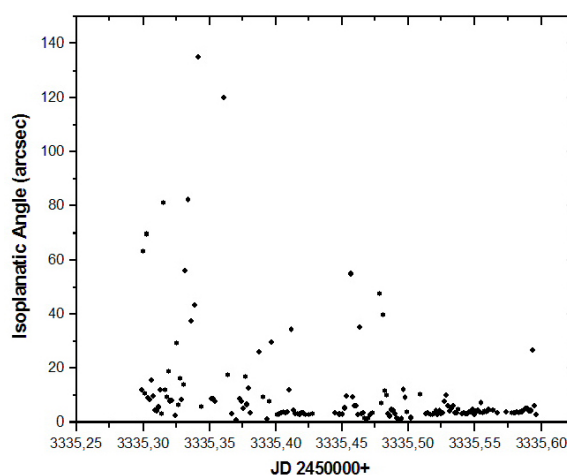


Figure 6.31: Diagram of Isoplanatic Angle for the night of 25/11/2004

Here it is presented the night of 25/11/2004. In figure 6.30 it is shown the diagrams of seeing and scintilation and in figure 6.31 is the diagram of isoplanatic angle. For this night the statistics are :

	Mean	St. Deviation	P75	Median
<b>Seeing (arcsec)</b>	1.13	0.25	1.32	1.08
<b>Scintilation (mag)</b>	0.04	0.083	0.043	0.013
<b>Isoplanatic Angle (arcsec)</b>	11.14	19.53	9.26	4.17

This night had nothing good to offer to us, with various changes. Scintilations remains in it's usual values.

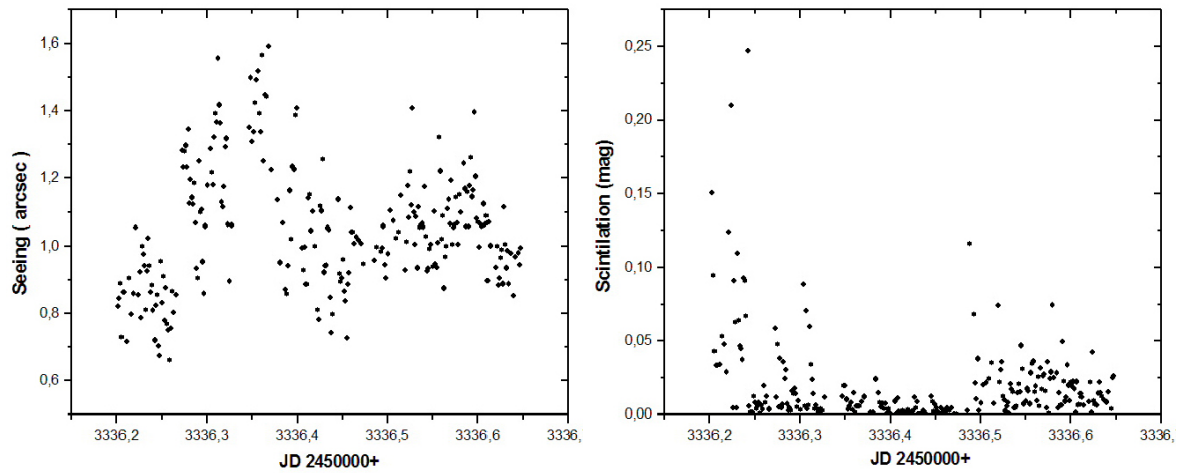


Figure 6.32: Diagrams of Seeing and Scintilation for the night of 26/11/2004

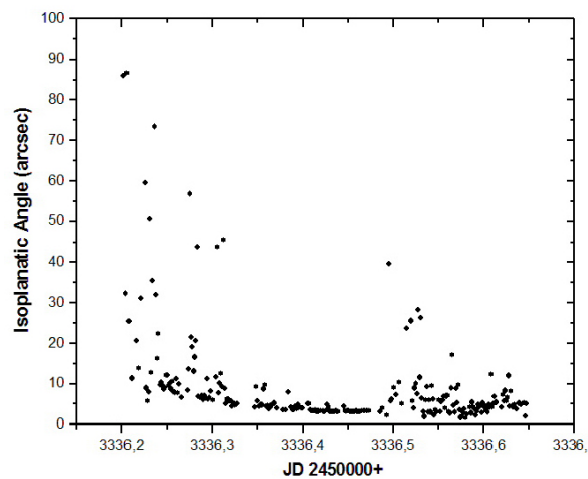


Figure 6.33: Diagram of Isoplanatic Angle for the night of 26/11/2004

Here it is presented the night of 26/11/2004. In figure 6.32 it is shown the diagrams of seeing and scintilation and in figure 6.33 is the diagram of isoplanatic angle. For this night the statistics are :

	Mean	St. Deviation	P75	Median
Seeing (arcsec)	1.04	0.18	1.14	1.02
Scintilation (mag)	0.019	0.03	0.022	0.008
Isoplanatic Angle (arcsec)	25.11	186.0	9.31	5.25

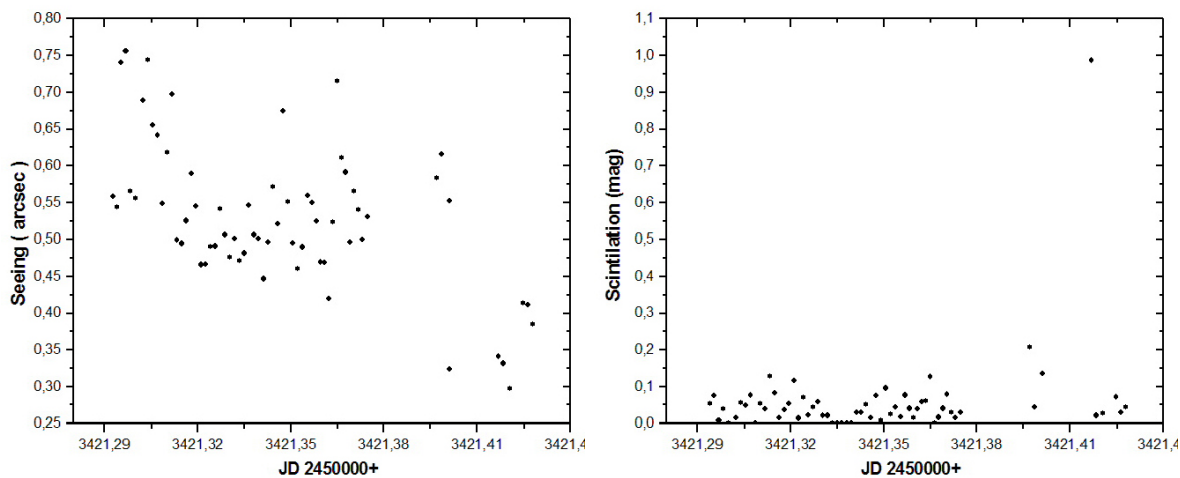


Figure 6.34: Diagrams of Seeing and Scintilation for the night of 19/02/2005

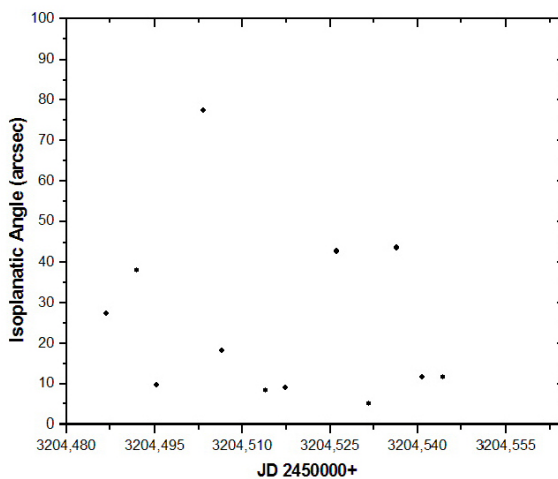


Figure 6.35: Diagram of Isoplanatic Angle for the night of 19/02/2005

Here it is presented the night of 19/02/2005. In figure 6.34 it is shown the diagrams of seeing and scintilation and in figure 6.35 is the diagram of isoplanatic angle. For this night the statistics are :

	Mean	St. Deviation	P75	Median
Seeing (arcsec)	0.52	0.096	0.56	0.52
Scintilation (mag)	0.059	0.12	0.061	0.039
Isoplanatic Angle (arcsec)	23.95	46.2	19.22	7.29

This night was excellent with very small St. Deviation of seeing and also good scintilation.

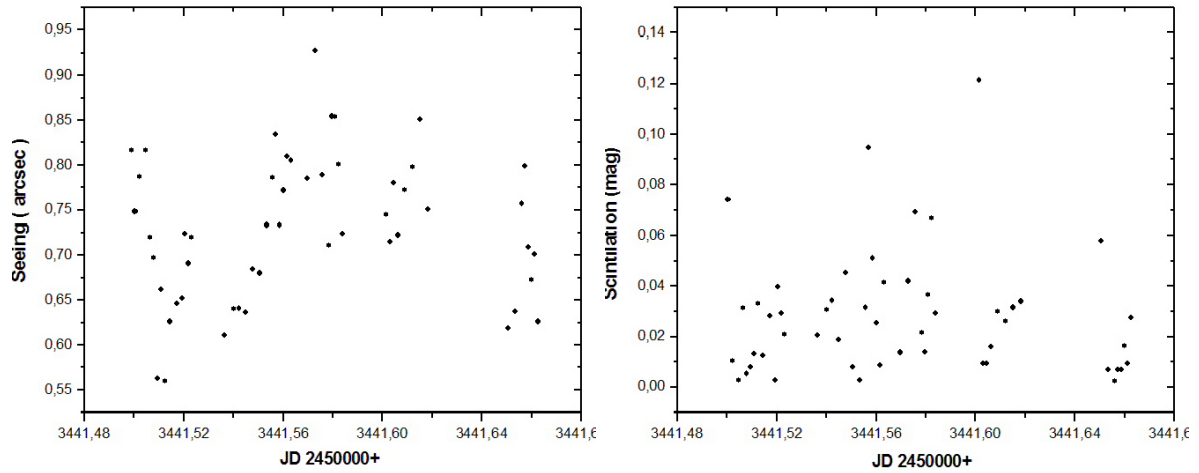


Figure 6.36: Diagrams of Seeing and Scintilation for the night of 11/03/2005

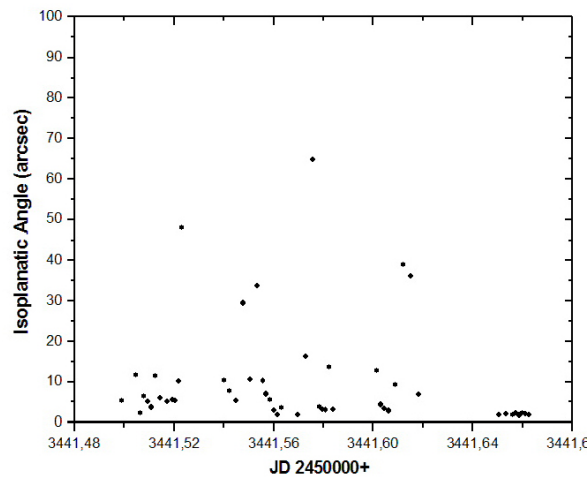


Figure 6.37: Diagram of Isoplanatic Angle for the night of 11/03/2005

Here it is presented the night of 11/03/2005. In figure 6.36 it is shown the diagrams of seeing and scintilation and in figure 6.37 is the diagram of isoplanatic angle. For this night the statistics are :

	Mean	St. Deviation	P75	Median
Seeing (arcsec)	0.72	0.079	0.78	0.72
Scintilation (mag)	0.027	0.024	0.034	0.025
Isoplanatic Angle (arcsec)	22.33	57.35	11.37	5.4

The night of 11/03/2005 was very good, since seeing was under the average, also St.Deviation was small. This means that seeing was quite stable during the night.

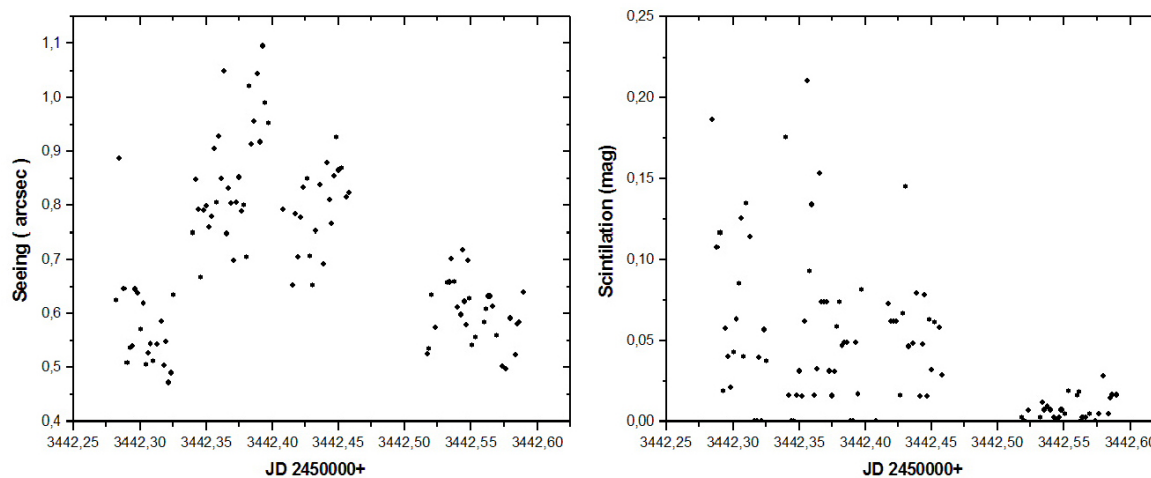


Figure 6.38: Diagrams of Seeing and Scintillation for the night of 12/03/2005

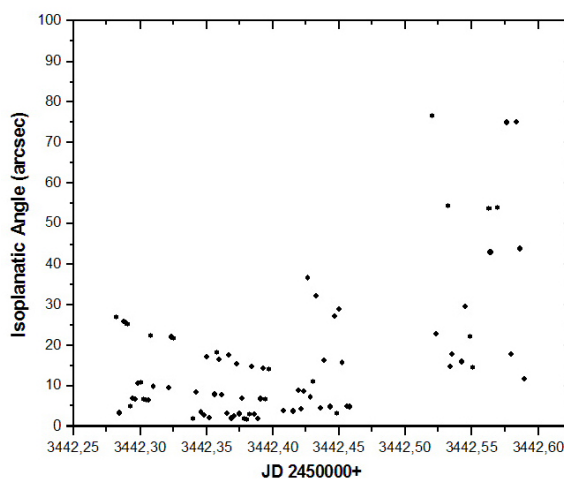


Figure 6.39: Diagram of Isoplanatic Angle for the night of 12/03/2005

Here it is presented the night of 12/03/2005. In figure 6.38 it is shown the diagrams of seeing and scintillation and in figure 6.39 is the diagram of isoplanatic angle. For this night the statistics are :

	Mean	St. Deviation	P75	Median
Seeing (arcsec)	0.71	0.14	0.81	0.69
Scintillation (mag)	0.042	0.045	0.062	0.03
Isoplanatic Angle (arcsec)	158.8	323.8	74.9	16.03

A typical night for observation in Xolomon.

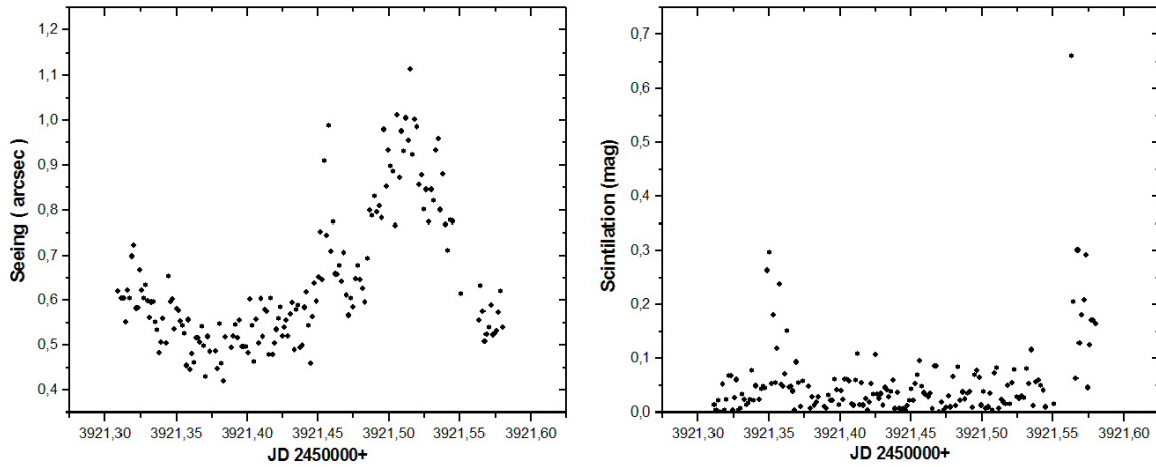


Figure 6.40: Diagrams of Seeing and Scintillation for the night of 04/07/2006

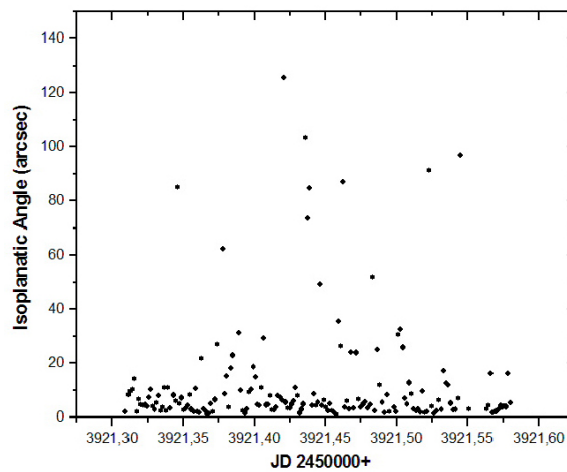


Figure 6.41: Diagram of Isoplanatic Angle for the night of 04/07/2006

Here it is presented the night of 04/07/2006. In figure 6.40 it is shown the diagrams of seeing and scintillation and in figure 6.41 is the diagram of isoplanatic angle. For this night the statistics are :

	Mean	St. Deviation	P75	Median
Seeing (arcsec)	0.63	0.15	0.71	0.59
Scintillation (mag)	0.055	0.074	0.059	0.035
Isoplanatic Angle (arcsec)	12.29	20.71	10.22	4.84

Here we have a strange and rare shape of the seeing curve. This variations it appears only in seeing and not in scintillation.

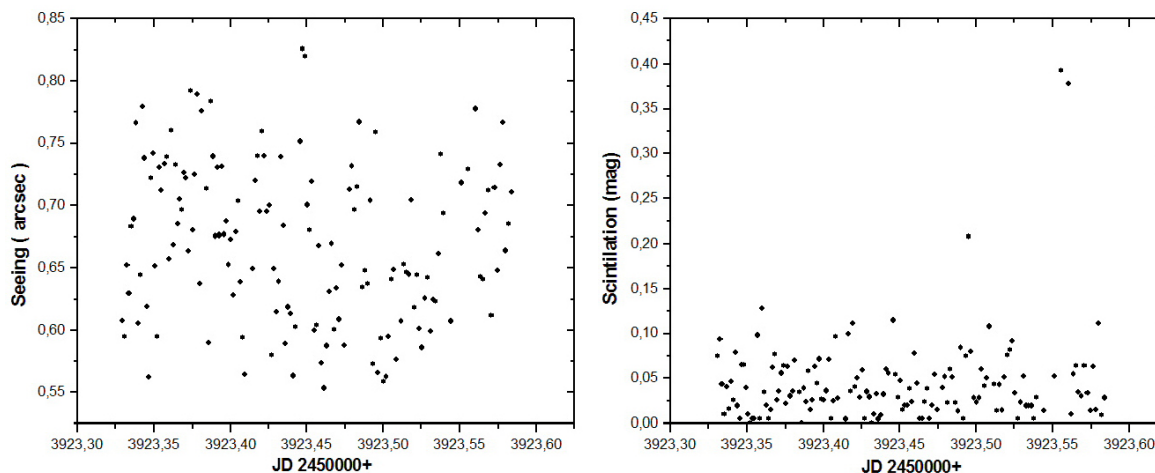


Figure 6.42: Diagrams of Seeing and Scintilation for the night of 06/07/2006

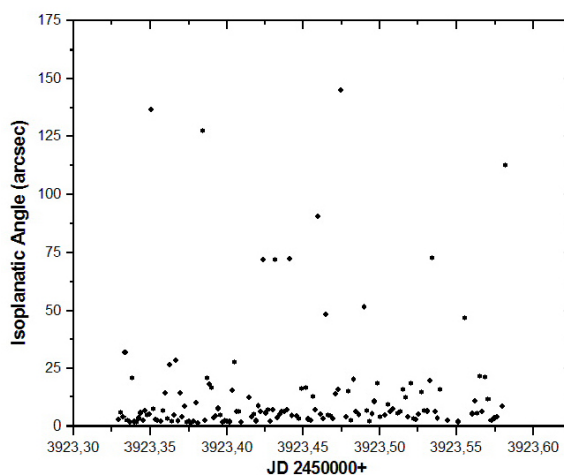


Figure 6.43: Diagram of Isoplanatic Angle for the night of 06/07/2006

Here it is presented the night of 06/07/2006. In figure 6.42 it is shown the diagrams of seeing and scintilation and in figure 6.43 is the diagram of isoplanatic angle. For this night the statistics are :

	Mean	St. Deviation	P75	Median
Seeing (arcsec)	0.66	0.06	0.71	0.66
Scintilation (mag)	0.045	0.051	0.06	0.034
Isoplanatic Angle (arcsec)	14.34	25.17	14.23	5.92

In this particular night seeing was stable and with small St. Deviation of it's values. The same thing applies for scintilation also.

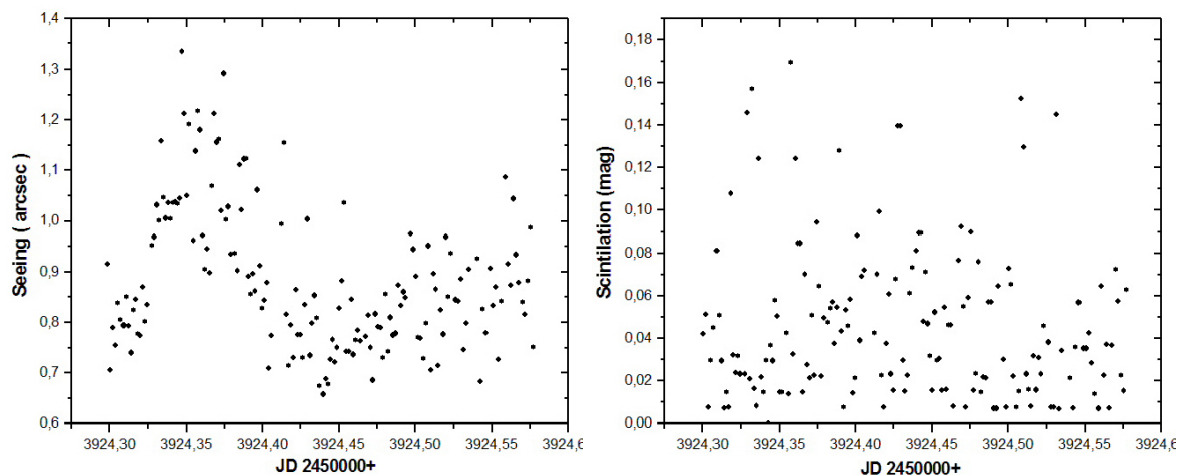


Figure 6.44: Diagrams of Seeing and Scintillation for the night of 07/07/2006

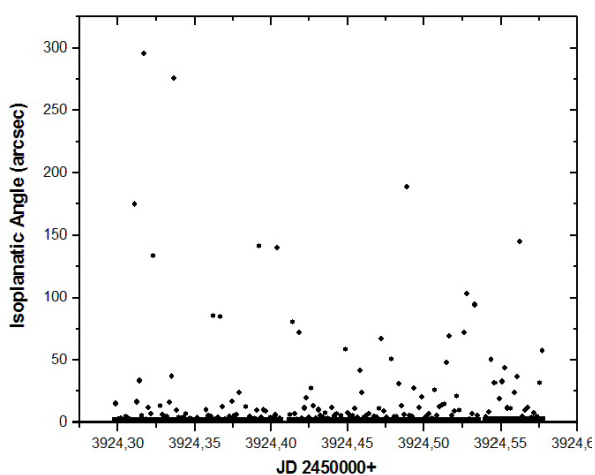


Figure 6.45: Diagram of Isoplanatic Angle for the night of 07/07/2006

Here it is presented the night of 07/07/2006. In figure 6.44 it is shown the diagrams of seeing and scintillation and in figure 6.45 is the diagram of isoplanatic angle. For this night the statistics are :

	Mean	St. Deviation	P75	Median
Seeing (arcsec)	0.88	0.13	0.96	0.85
Scintillation (mag)	0.045	0.035	0.06	0.035
Isoplanatic Angle (arcsec)	50.5	200.41	38.1	12.28

Seeing was changing is this night too. Scintillation is typical again.

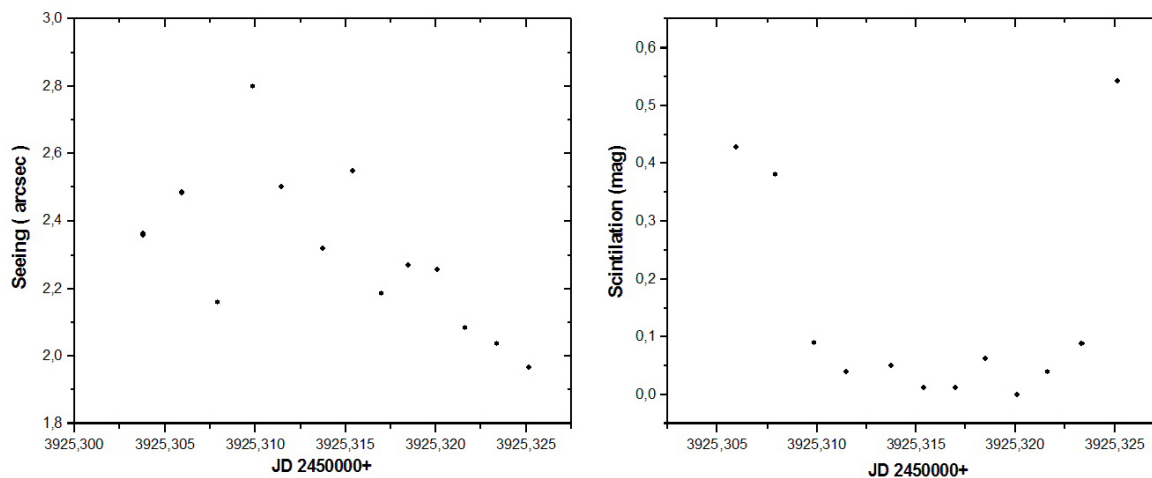


Figure 6.46: Diagrams of Seeing and Scintilation for the night of 08/07/2006

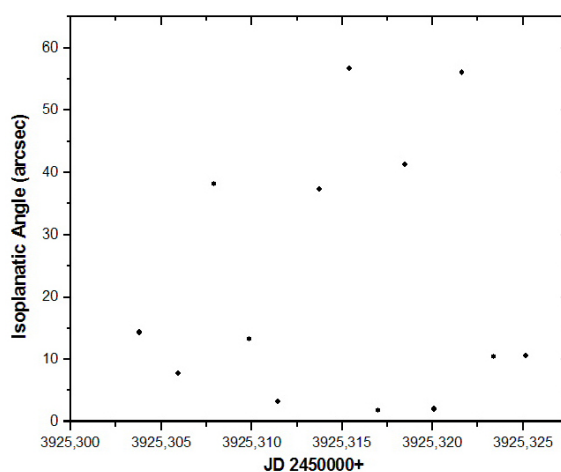


Figure 6.47: Diagram of Isoplanatic Angle for the night of 08/07/2006

Here it is presented the night of 08/07/2006. In figure 6.46 it is shown the diagrams of seeing and scintilation and in figure 6.47 is the diagram of isoplanatic angle. For this night the statistics are :

	Mean	St. Deviation	P75	Median
<b>Seeing (arcsec)</b>	2.3	0.23	2.48	2.27
<b>Scintilation (mag)</b>	0.14	0.18	0.089	0.056
<b>Isoplanatic Angle (arcsec)</b>	22.5	20.41	38.14	13.28

This unfortunately there aren't many data. But we can see that this is one of the worst nights ever recorded at Xolomon. Even scintilation is worser than usual, this means that the atmosphere was turbulent in most of her layers.

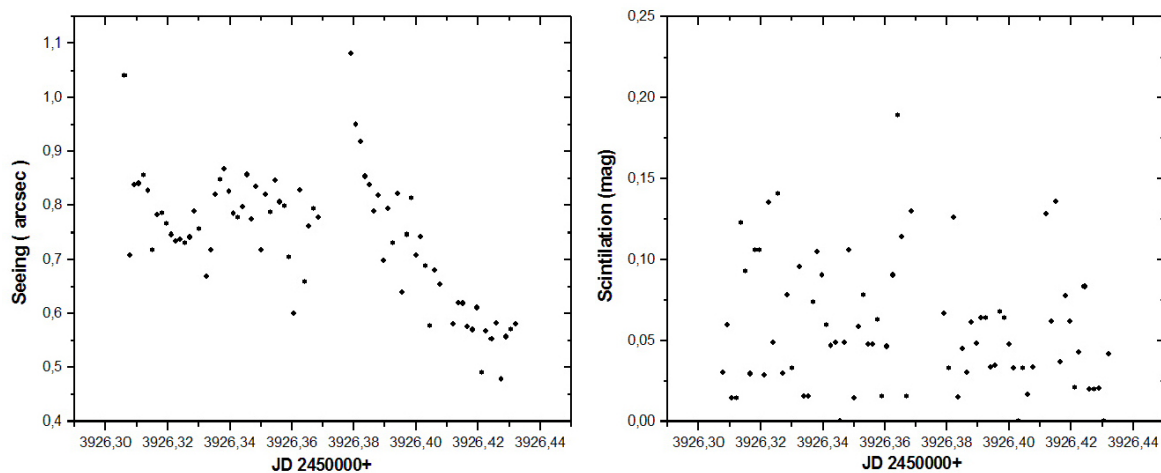


Figure 6.48: Diagrams of Seeing and Scintilation for the night of 09/07/2006.

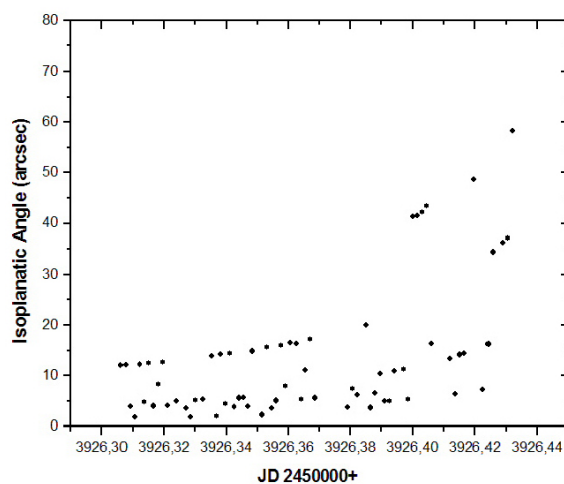


Figure 6.49: Diagram of Isoplanatic Angle for the night of 09/07/2006

Here it is presented the night of 09/07/2006. In figure 6.48 it is shown the diagrams of seeing and scintilation and in figure 6.49 is the diagram of isoplanatic angle. For this night the statistics are :

	Mean	St. Deviation	P75	Median
Seeing (arcsec)	0.74	0.11	0.81	0.75
Scintilation (mag)	0.058	0.039	0.078	0.048
Isoplanatic Angle (arcsec)	36.07	68.9	20.05	12.06

This night also is typical without something to notice about.

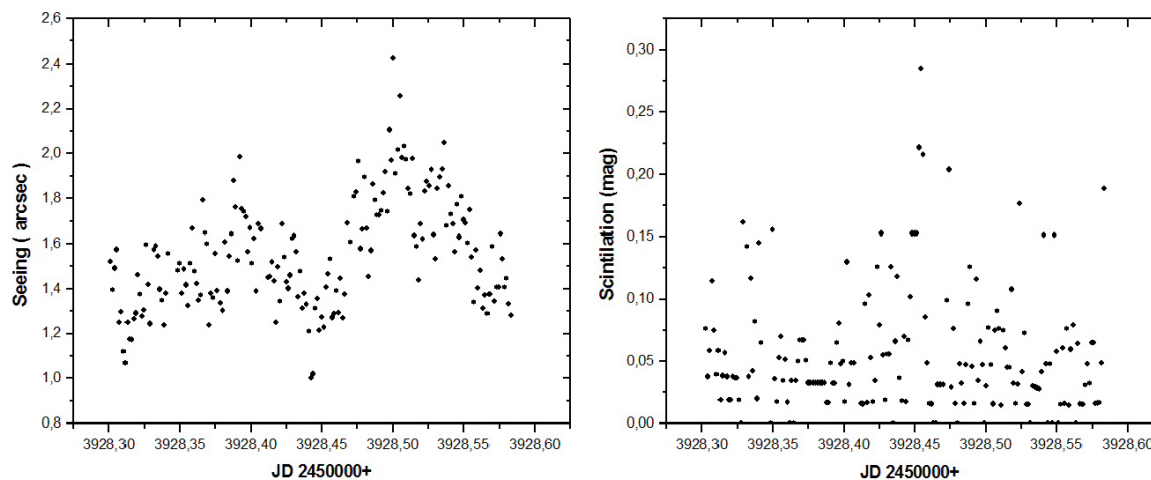


Figure 6.50: Diagrams of Seeing and Scintillation for the night of 11/07/2006

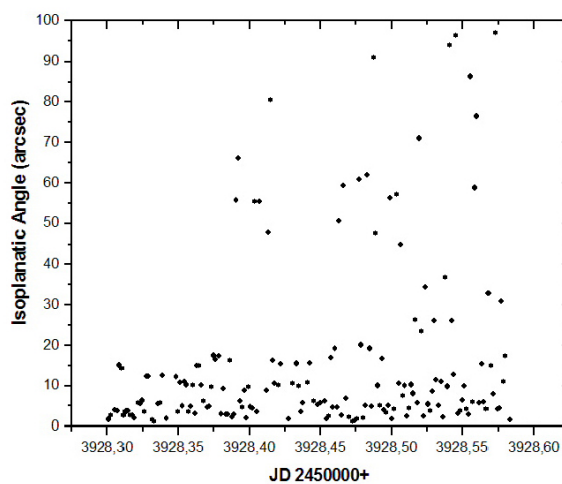


Figure 6.51: Diagram of Isoplanatic Angle for the night of 11/07/2006

Here it is presented the night of 11/07/2006. In figure 6.50 it is shown the diagrams of seeing and scintillation and in figure 6.51 is the diagram of isoplanatic angle. For this night the statistics are :

	Mean	St. Deviation	P75	Median
Seeing (arcsec)	1.54	0.24	1.68	1.53
Scintillation (mag)	0.055	0.048	0.07	0.041
Isoplanatic Angle (arcsec)	56.9	201.68	23.43	9.56

This particular night the conditions were not very good. Seeing was big and constatly changing. Worth mentioning is that scintillation is typical and intepented from seeing.

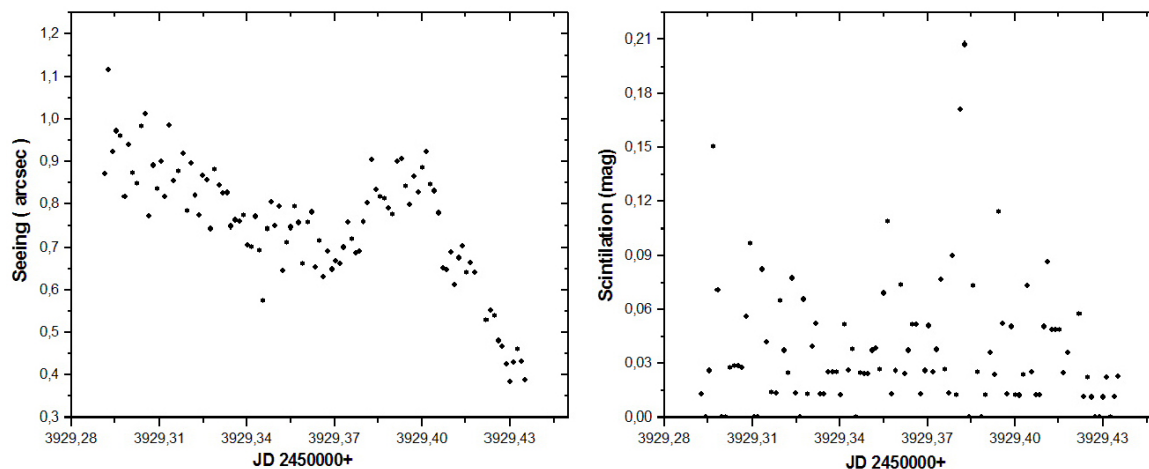


Figure 6.52: Diagrams of Seeing and Scintillation for the night of 12/07/2006

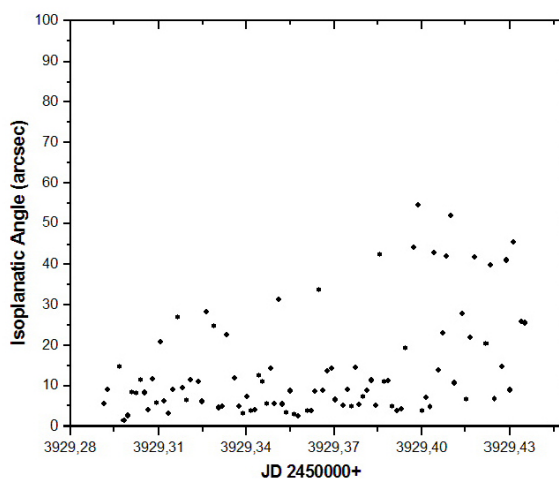


Figure 6.53: Diagram of Isoplanatic Angle for the night of 12/07/2006

Here it is presented the night of 12/07/2006. In figure 6.52 it is shown the diagrams of seeing and scintillation and in figure 6.53 is the diagram of isoplanatic angle. For this night the statistics are :

	Mean	St. Deviation	P75	Median
Seeing (arcsec)	0.75	0.14	0.84	0.77
Scintillation (mag)	0.036	0.035	0.051	0.025
Isoplanatic Angle (arcsec)	106.9	327.33	26.91	10.9

We can see that in this night seeing was not so stable, in fact towards the end of the observations it's value dropped. Scintillation was stable and it's value was typical.

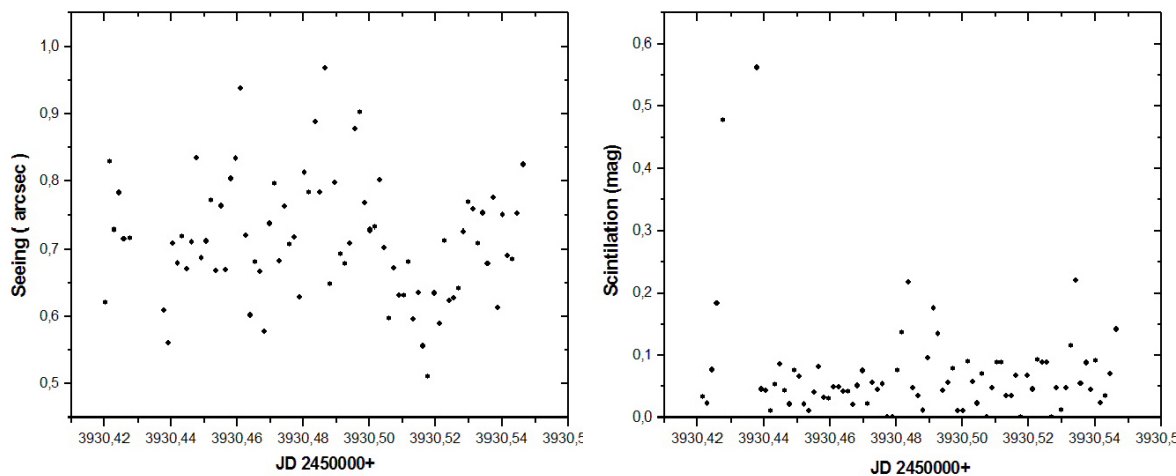


Figure 6.54: Diagrams of Seeing and Scintillation for the night of 13/07/2006

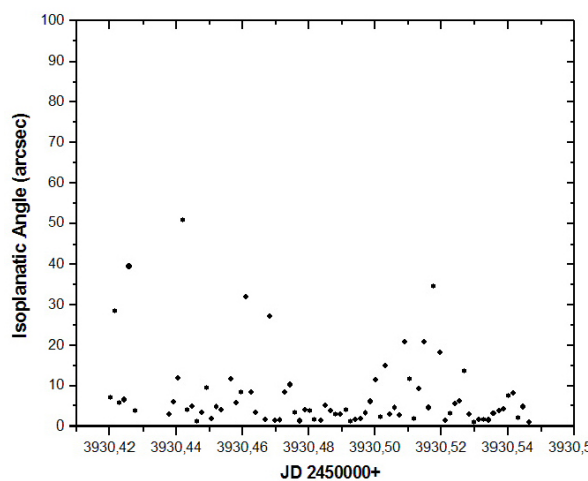


Figure 6.55: Diagram of Isoplanatic Angle for the night of 13/07/2006

Here it is presented the night of 13/07/2006. In figure 6.54 it is shown the diagrams of seeing and scintillation and in figure 6.55 is the diagram of isoplanatic angle. For this night the statistics are :

	Mean	St. Deviation	P75	Median
Seeing (arcsec)	0.71	0.087	0.76	0.7
Scintillation (mag)	0.071	0.085	0.085	0.049
Isoplanatic Angle (arcsec)	29.04	165.85	8.3	4.09

It is obvious that this particular night was stable with small values of scintillation, making it photometric.

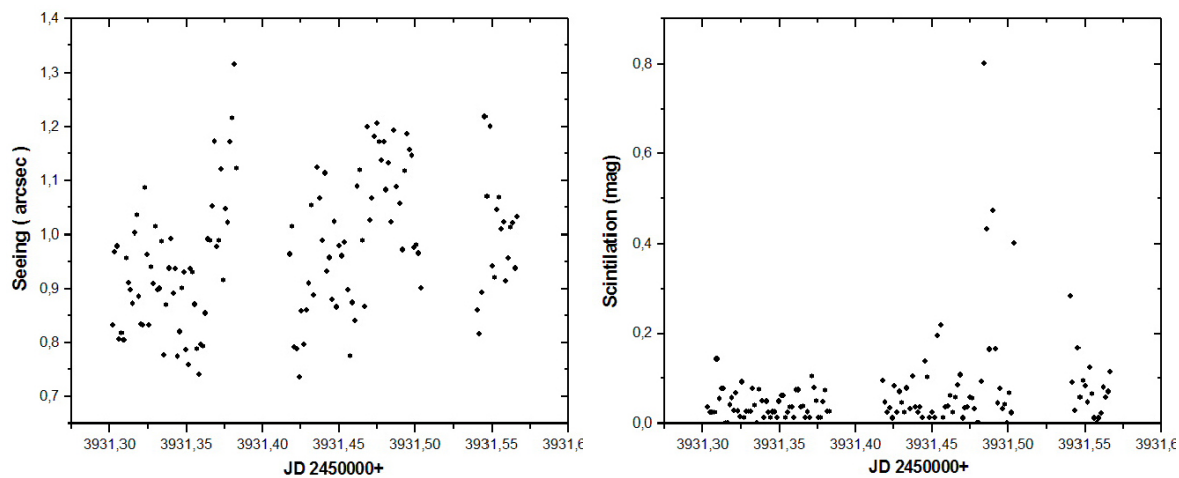


Figure 6.56: Diagrams of Seeing and Scintilation for the night of 14/07/2006

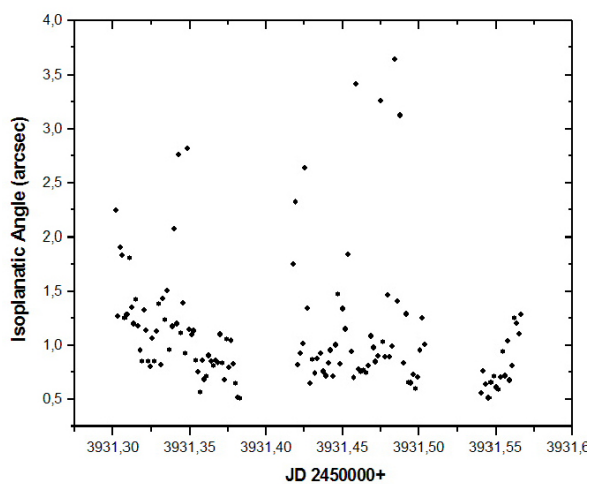


Figure 6.57: Diagram of Isoplanatic Angle for the night of 14/07/2006

Here it is presented the night of 14/07/2006. In figure 6.56 it is shown the diagrams of seeing and scintilation and in figure 6.57 is the diagram of isoplanatic angle. For this night the statistics are :

	Mean	St. Deviation	P75	Median
Seeing (arcsec)	0.97	0.12	1.05	0.96
Scintilation (mag)	0.066	0.098	0.076	0.037
Isoplanatic Angle (arcsec)	1.12	0.59	1.25	0.93

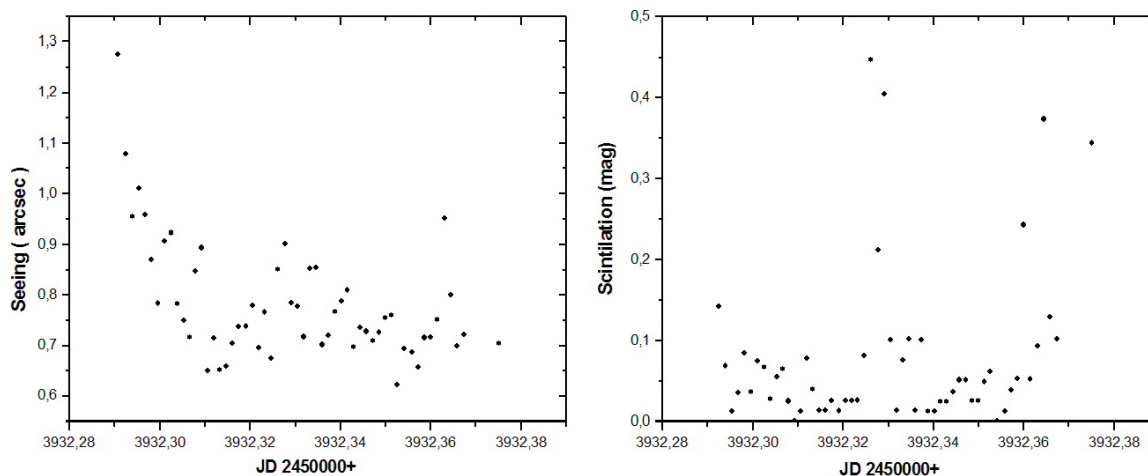


Figure 6.58: Diagrams of Seeing and Scintillation for the night of 15/07/2006

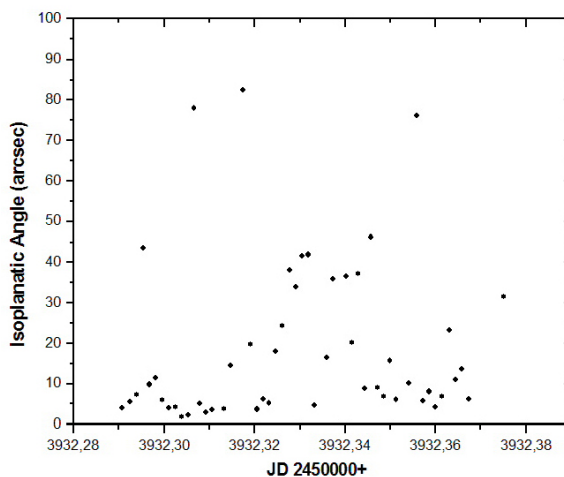


Figure 6.59: Diagram of Isoplanatic Angle for the night of 15/07/2006

Here it is presented the night of 15/07/2006. In figure 6.58 it is shown the diagrams of seeing and scintillation and in figure 6.59 is the diagram of isoplanatic angle. For this night the statistics are :

	Mean	St. Deviation	P75	Median
<b>Seeing (arcsec)</b>	0.78	0.11	0.84	0.75
<b>Scintillation (mag)</b>	0.078	0.1	0.084	0.048
<b>Isoplanatic Angle (arcsec)</b>	54.54	179.24	36.51	11.24

This night did not begin with the best values but later on got better, seeing dropped and stayed stable trough the end of the night.

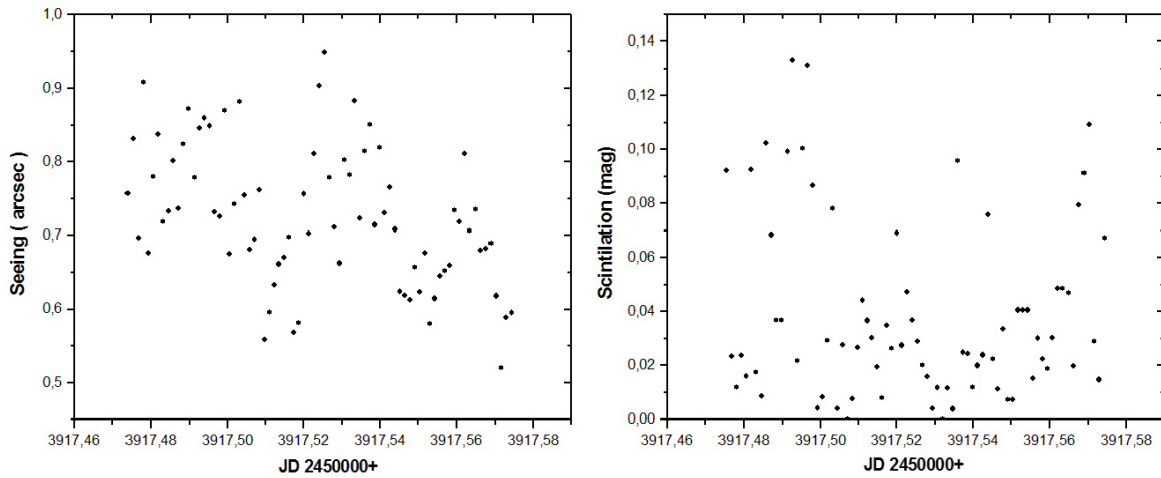


Figure 6.60: Diagrams of Seeing and Scintillation for the night of 30/06/2006

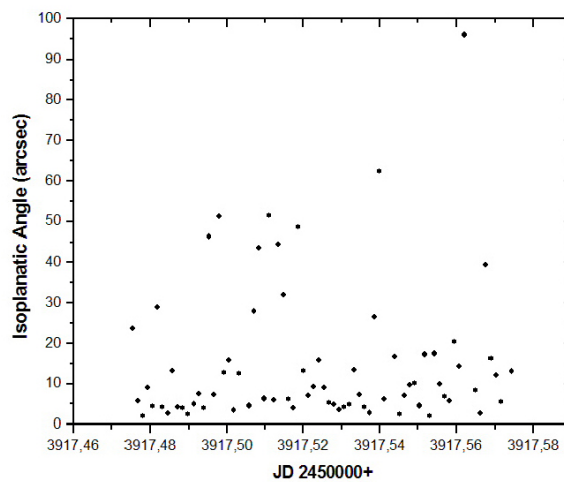


Figure 6.61: Diagram of Isoplanatic Angle for the night of 30/06/2006

Here it is presented the night of 30/06/2006. In figure 6.60 it is shown the diagrams of seeing and scintillation and in figure 6.61 is the diagram of isoplanatic angle. For this night the statistics are :

	Mean	St. Deviation	P75	Median
Seeing (arcsec)	0.72	0.09	0.8	0.71
Scintillation (mag)	0.038	0.032	0.047	0.027
Isoplanatic Angle (arcsec)	85.52	496.8	20.34	9.04

This night is typical concerning seeing, but scintillation is much better, confirming the theory that wants seeing and scintillations caused by different layers in the atmosphere.

### 6.1.1 Confirmation of the No-Correlation of Seeing and Scintillation

In this section a confirmation of the theory was done concerning the no correlation of seeing and scintillation. As it is already been said seeing and scintillation are caused by different layers in the atmosphere, with seeing produced by cells in the lower and scintillation by cells in the upper atmosphere.

Here simultaneous observations of seeing and scintillation were made with the H-DIMM unit in mount Xolomon. The observations are the same with the ones that are already presented, so here only a simple comparison is made. The night of 04/07/2006 was taken for this comparison. In this particular night it is very evident the non correlation of seeing and scintillation. Of course the conclusion is universal despite the example of only one night. The same characteristics are evident in most of the nights, but for artistic reasons and available space only one night is chosen.

For a certain correlation, a combined diagrams technic is used. This technic is working by fitting with least squares of seeing and scintillation as it is shown at figure 6.62. Then we take these two diagrams and combined them to one. If the angle that is formed is small or zero then it means that the values are correlated. If the angle is  $90^\circ$  or even bigger then it means that they are un-correlated. The result is shown in figure 6.63. The angle here is larger than  $90^\circ$ . So it is obvious that Seeing

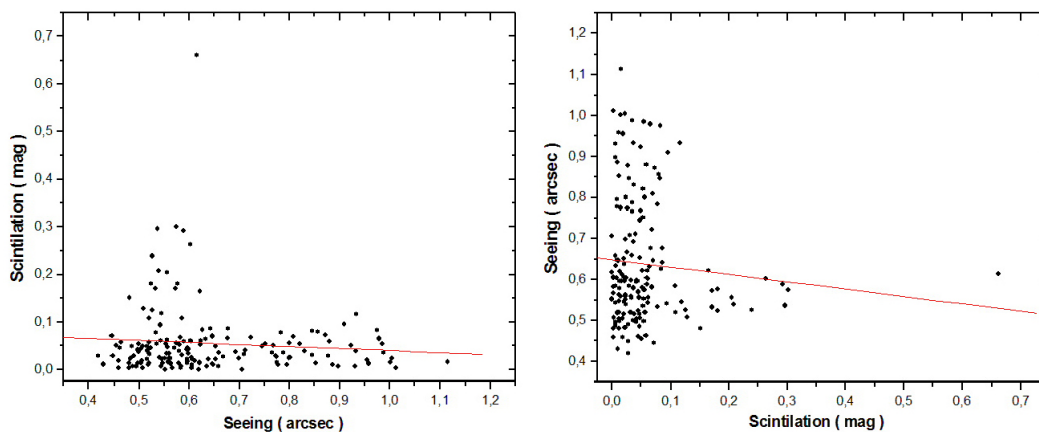


Figure 6.62: Diagram of Seeing - Scintillation and Scintillation - Seeing.

and Scintillation do not correlate in any way and thus they are independent. This is a way to prove that seeing and scintillation are actually caused by different layers in the atmosphere.

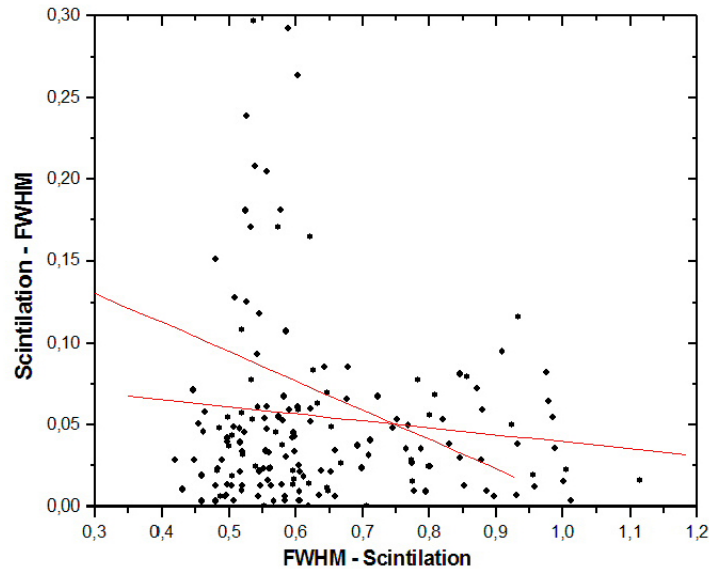


Figure 6.63: Correlation Diagram of Seeing and Scintillation.

## 6.2 Conclusions

For the necessary explanation of the results, various histograms were made, also a statistical analysis was done. The left histogram of figure 6.64 is seeing and at the right is scintillation. It is clear that the seeing has a distribution that looks like a gaussian with a maximum at the value of 0,86 arcsec<sup>1</sup>. Also it is obvious that the distribution is slightly moved to the left. This is caused by the dependence of the observed seeing value by the exposure time we use during the observations. As the exposure time increases, the relative displacement of the two idols produced by the two subapertures is smoothed out, the result is that the value of seeing gets smaller. The correction for this phenomenon was not done here and that's why there is a small underestimation of seeing in the order of  $\approx 0.1$  arcsec.

The St. Deviation of seeing is 0,31 arcsec. This particular value is not bad but it can not show us how stable the nights really was. To conclude some safe conclusions about this parameter we must have a look at all the individual St. deviation of the observed nights, or else we must find the mean value of St. Deviation of all nights. In the present work this was not done and is left for future analysis.

A quick conclusion I can make is that by watching the St. Deviation of many nights, the typical value is 0.1 arcsec and not 0,31 arcsec. Some nights even have values of  $\approx 0,05$  arcsec. This means that Xolomon is an exceptional place for astronomical observations, that can be one of the best worldwide with the help of an Adaptive Optics unit. This unit will have great results because of the stability of the nights Xolomon has. This is reinforced by the values of the isoplanatic angle, which

<sup>1</sup>Full statistics for all the observations are in tables 6.2 and 6.3

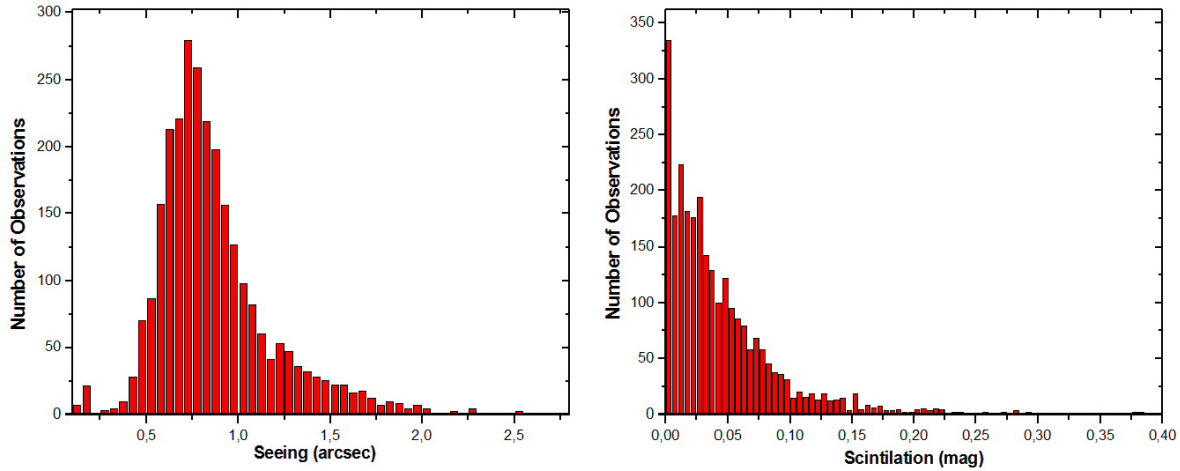


Figure 6.64: Histograms of Seeing and Scintilation for all the Observations that are Made in Xolomon until now.

	Mean	St. Deviation	Median
Seeing (arcsec)	0.86	0.31	0.79
Scintilation (mag)	0.049	0.074	0.031
Isoplanatic Angle (arcsec)	45.32	193.26	6.86

Table 6.2: Total Statistics of the Observations

they are big enough so to help AO systems very much. From table 6.3 it is clear that the 80% of the observations are better than 1 arcsec. This fact is an incredible result if we think the low altitude the observations were made.

In the left of figure 6.64, it is the histogram of scintilation. From this figure and table 6.3 we conclude that the values of scintilation are low, with the 90% of the observations to be better than 0.1 mag. This fact is great if we think the potential for accurate and fast photometry.

In figure 6.65 it is the pie-diagram for seeing. Also in figure 6.66 is the histogram of the isoplanatic angle for all the observations that have been done in Xolomon. At tables 6.2 and 6.3 are the results of the statistical analysis for the data. As it is shown in figure 6.66 and in table 6.3, the 50% of the observations for the isoplanatic angle are better than  $\approx 18$  arcsec. This fact is great and it can help the effectiveness of AO systems.

This fact in combination with the very low values of scintilation, can help in the discovery of new supernova but also in projects that involve high speed photometry with instruments as Ultra-Cam. The high mean value of the isoplanatic angle should not be worry as because no filter was applied for the rejection of noise, and as a result very high and unnatural values are taken in mind to the calculations of mean value. Of course St. Deviation is also affected.

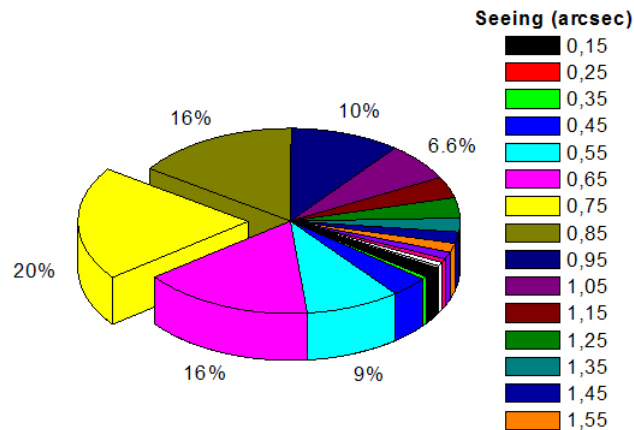


Figure 6.65: Percentage of Observations in a Pie-Diagram

	Seeing (arcsec)	Scintillation (mag)	Isoplanatic Angle (arcsec)
P100	2.79	1.27	4319
P90	1.28	0.1	70.12
P80	1.04	0.071	27.25
P75	0.98	0.061	18.7
P50	0.79	0.031	6.86
P25	0.66	0.013	3.55
P10	0.56	0.003	1.95

Table 6.3: Percentage of Observations

As a final result i must say that the place that the observations took place was not ideal from an astronomical point of view. The altitude was about 800 m, very low. Also the observations were made in the facilities of the agricultural division near a tavern that usually a fire place was operational. This of course affected the observations and probably is responsible for some unnaturally big values, and in result affected the mean value observed. So probably the real behaviour of the place is even better from the observed. This is very important if we think of the very nice behaviour already.

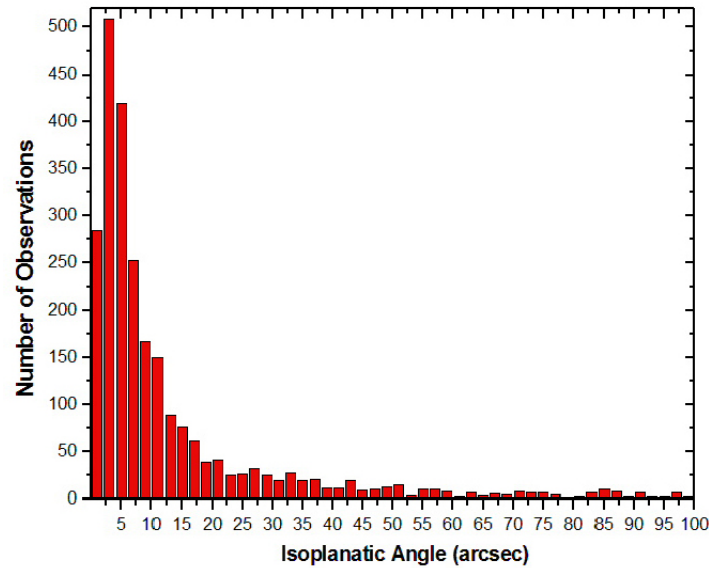


Figure 6.66: Histogram of Isoplanatic Angle for all the Observations until now.

### 6.2.1 Possible Future Work

As a possible future development of the presented work about the astronomical properties of the atmosphere in Xolomon could be:

- Re-analyse the data for better accuracy, from correcting the exposure time bias. This will permit us for even safer conclusion concerning the absolute value of seeing in Xolomon.
- A better statistical analysis of the results. The mean value of St. Deviation of every night should be computed, for all the parameters of course, and not just the St. Deviation of the observations. This must be done so we can safely have our conclusions, about the stability of the parameters during the duration of a night.
- Also in the future a comparison at the same time of the atmospheric parameters that interests astronomy, with meteorological data, so we can see if their is any correlation between them. This will help the posible prediction of seeing just from the meteorological data. Of course for a more better study of this possibility the Seeing-GR project will help very much. It will add the neccessary statistical security over many different conditions, both meteorological and geographical.

[13][20][6][10][2][11][4][21][5][14][15][22][23][12][24][17][27][3][7][8][9][16][1][26][25][18][19]

# Index

- 44i Boo, 5
- Air Mass, 88, 102
- Apparent Orbit, 15
- Apparent Period Changes, 11, 13
- Apparent Zenith Angle, 89
- Atmospheric Dispersion, 92
- Atmospheric Layers, 95
- Autoregressive Moving Model, 20
  
- Center of Mass, 24
- Chaotic Behaviour, 85
- Classical Model, 16
  - Mathematical Failure, 17
  - Physical Failure, 19
- Coherence Angle, 95
- Cubic Spline Connection, 21
  
- Density Gradient, 90
- Deterministic, 46
- Differential Refraction, 92
- DIMM, 99
  - ESO DIMM, 99
  - Hartmann DIMM, 101
- Dynamical Phenomena, 13
  
- Eclipses, 2
  - Ephemeris, 2
  - Times of Minima, 2
- ER-ORI, 3
- Extinction Coefficient, 88
- Extinction Theorem, 89
  
- Flat-Earth Approximation, 91
  
- Fourier Algorithm, 43
- Free Atmosphere, 94
- Frozen Turbulence, 95
- Full Width Half Maximum (FWHM), 98
  
- Harmonics, 45
  
- Isoplanatic Angle, 95, 112
- Isoplanatic Patch, 95
  
- Kalimeris Model, 20, 22
- Kinematic Model, 35
- Kolmogorov, 100
- Kolmogorov Model, 93
  
- Least Square Fitting, 20
- Light Curves, 48
- Light Equation, 14
- Light-Time Effect, 13, 23
- Longitudinal Covariance, 100
  
- Mass Transfer, 19
- Mean Anomaly, 14
- Mean Square Error, 21
- Microquasar, 33
- Modulation Transfer Function (MTF), 97
  
- Noise, 10
  - Noise Handling, 23
  - Observational, 10
  - Photometric, 11, 23
- Non-Linear Modulation, 9
- Nutation, 13
  
- O-C Diagrams, 3

- Noise Floor, 21
- O-C Differences, 3
- Orbital Period Changes, 5
- Parabolic Arc, 10
- Times of Minima, 5
- W Uma, 4
- P(E) Function, 17, 18, 22
- Piecewise Approximation, 21
- Point Spread Function (PSF), 97
- Polynomials
  - Chebyshev, 20, 23
  - Legendre, 20
- QPO, 85
- Quasars, 33
  - List of Quasars, 33
- Refraction, 91
- Relative Orbit, 13
- Residuals, 23
- SBIG, 114
- Scintillation, 109
- Scintillation Indexes, 110
- Seeing, 93, 94
  - Theory, 93
- Seeing-GR, 104
- SNR W50, 34
- SS433, 34
  - Data Analysis, 41
  - Flares, 39
  - Jets, 38
  - Nutational, 34
  - Observations, 41
  - Orbital, 34
  - Precessional, 34
- Stable Rate Changes, 9
- Starlink, 111
- Stellar Spots, 12
- Step Variations Model, 16
- Stochastic, 46
- Strehl Ratio, 97
- Temporal Averaging, 103
- Temporal Behaviour, 95
- Temporal Phase Structure Function, 95
- Third Body, 14, 23
- Transverse Covariance, 100
- True Zenith Angle, 89
- True Zenith Distance, 91
- Turbulent Field, 94
- Vixen Visac, 114
- Wavelet Algorithm, 45
- Xolomon, 25

# Bibliography

- [1] M. C. B. Ashley, J. S. Lawrence, J. W. V. Storey, and A. Tokovinin. Mass seeing measurements from Dome C. In M. Giard, F. Casoli, and F. Paletou, editors, *EAS Publications Series*, pages 19–24, 2005.
- [2] A. A. Aslanov, A. M. Cherepashchuk, V. P. Goranskij, V. Y. Rakhimov, and R. C. Vermeulen. Multicolour photometry of SS 433 during the monitoring campaign in May/June 1987. *A&A*, 270:200–203, March 1993.
- [3] J. Bally, D. Theil, Y. Billawalla, D. Potter, R. F. Loewenstein, F. Mrozek, and J. P. Lloyd. A Hartmann differential image motion monitor (H-DIMM) for atmospheric turbulence characterisation. *Publications of the Astronomical Society of Australia*, 13:22–27, January 1996.
- [4] K. M. Blundell and M. G. Bowler. Symmetry in the Changing Jets of SS 433 and Its True Distance from Us. *apjl*, 616:L159–L162, December 2004.
- [5] S. K. Chakrabarti, A. Nandi, S. Pal, B. G. Anandarao, and S. Mondal. Photometric evidence of bullets in SS433 jets. In M. Novello, S. Perez Bergliaffa, and R. Ruffini, editors, *The Tenth Marcel Grossmann Meeting. On recent developments in theoretical and experimental general relativity, gravitation and relativistic field theories*, pages 1324–1327, 2005.
- [6] A. M. Cherepashchuk, R. A. Sunyaev, S. N. Fabrika, S. V. Molkov, E. A. Barsukova, E. A. Antokhina, T. R. Irmambetova, I. E. Panchenko, K. A. Postnov, E. V. Seifina, N. I. Shakura, A. N. Timokhin, I. F. Bikmaev, N. A. Sakhbullin, Y. N. Gnedin, A. Arkharov, and M. M. Larionov. Coordinated INTEGRAL and Optical Observations of SS433. In V. Schoenfelder, G. Lichti, and C. Winkler, editors, *ESA SP-552: 5th INTEGRAL Workshop on the INTEGRAL Universe*, pages 207–+, October 2004.
- [7] D. Dravins, L. Lindegren, E. Mezey, and A. T. Young. Atmospheric Intensity Scintillation of Stars. I. Statistical Distributions and Temporal Properties. *pasp*, 109:173–207, February 1997.
- [8] D. Dravins, L. Lindegren, E. Mezey, and A. T. Young. Atmospheric Intensity Scintillation of Stars. II. Dependence on Optical Wavelength. *pasp*, 109:725–737, June 1997.

- [9] D. Dravins, L. Lindegren, E. Mezey, and A. T. Young. Atmospheric Intensity Scintillation of Stars. III. Effects for Different Telescope Apertures. *pasp*, 110:610–633, May 1998.
- [10] S. Fabrika and T. Irmambetova. The central region in SS 433 supercritical disk and origin of flares. In P. Durouchoux, Y. Fuchs, and J. Rodriguez, editors, *New Views on MICRO-QUASARS, the Fourth Microquasars Workshop, Institut d’Etudes Scientifiques de Cargèse, Corsica, France, May 27 - June 1, 2002. Edited by Ph. Durouchoux, Y. Fuchs, and J. Rodriguez. Published by the Center for Space Physics: Kolkata (India), p. 268.*, pages 268–+, 2003.
- [11] D. R. Gies, M. V. McSwain, R. L. Riddle, Z. Wang, P. J. Wiita, and D. W. Wingert. The Spectral Components of SS 433. *apj*, 566:1069–1083, February 2002.
- [12] V. P. Goranskii, V. F. Esipov, and A. M. Cherepashchuk. Optical variability of SS 433 in 1978-1996. *Astronomy Reports*, 42:209–228, March 1998.
- [13] V. P. Goranskij. Analysis of Twenty-Year Multicolor Photometry of SS 433 (V1343 Aql) an Unique Eclipsing System with Relativistic Jets. In J. Dusek and M. Zejda, editors, *29th Conference on Variable Star Research*, pages 103–+, 1998.
- [14] A. Kalimeris, H. Rovithis-Livaniou, and P. Rovithis. Starspots and photometric noise on observed minus calculated (O-C) diagrams. *A&A*, 387:969–976, June 2002.
- [15] A. Kalimeris, H. Rovithis-Livaniou, P. Rovithis, G. Oprescu, A. Dumitrescu, and M. D. Suran. An orbital period study of the contact system AB Andromedae. *A&A*, 291:765–774, November 1994.
- [16] S. Kenyon, J. Lawrence, M. C. B. Ashley, J. W. V. Storey, A. Tokovinin, and E. Fossat. Atmospheric scintillation at Dome C, Antarctica: implications for photometry and astrometry. *Astronomy in Antarctica, 26th meeting of the IAU, Special Session 7, 22-23 August, 2006 in Prague, Czech Republic, SPS7, #30*, 7, August 2006.
- [17] B. Lopez and M. Sarazin. The ESO atmospheric temporal coherence monitor dedicated to high angular resolution imaging. *A&A*, 276:320–+, September 1993.
- [18] J. S. Nestoras, D. Mislis, S. Pyrzas, E. Tremou, J. H. Seiradakis, and S. I. Avgoloupis. Seeing Measurements from Mt. Holomon. In N. Solomos, editor, *AIP Conf. Proc. 848: Recent Advances in Astronomy and Astrophysics*, pages 906–909, August 2006.
- [19] J. S. Nestoras, J. H. Seiradakis, E. Harlaftis, O. Giannakis, and S. Kitsionas. Fourier Analysis of SS433 - High Speed Photometry. In N. Solomos, editor, *AIP Conf. Proc. 848: Recent Advances in Astronomy and Astrophysics*, pages 427–431, August 2006.

- [20] M. Revnivtsev, R. Burenin, S. Fabrika, K. Postnov, I. Bikmaev, M. Pavlinsky, R. Sunyaev, I. Khamitov, and Z. Aslan. First simultaneous X-ray and optical observations of rapid variability of supercritical accretor SS433. *A&A*, 424:L5–L8, September 2004.
- [21] M. Revnivtsev, S. Fabrika, P. Abolmasov, K. Postnov, I. Bikmaev, R. Burenin, M. Pavlinsky, R. Sunyaev, I. Khamitov, and N. Sakhbullin. Broad band variability of SS433: accretion disk at work? *A&A*, 447:545–551, February 2006.
- [22] H. Rovithis-Livaniou, A. Kalimeris, and P. Rovithis. Influence of spots on O-C diagrams of close eclipsing binary stars. In C. Sterken, editor, *ASP Conf. Ser. 292: Interplay of Periodic, Cyclic and Stochastic Variability in Selected Areas of the H-R Diagram*, pages 163–+, March 2003.
- [23] H. Rovithis-Livaniou, S. Tsantilas, and A. Kalimeris. On the origin of the orbital period changes of V523 Cas. In C. Sterken, editor, *ASP Conf. Ser. 292: Interplay of Periodic, Cyclic and Stochastic Variability in Selected Areas of the H-R Diagram*, pages 215–+, March 2003.
- [24] M. Sarazin and F. Roddier. The ESO differential image motion monitor. *A&A*, 227:294–300, January 1990.
- [25] M. Sarazin and A. Tokovinin. The Statistics of Isoplanatic Angle and Adaptive Optics Time Constant derived from DIMM Data. In E. Vernet, R. Ragazzoni, S. Esposito, and N. Hubin, editors, *Beyond conventional adaptive optics : a conference devoted to the development of adaptive optics for extremely large telescopes. Proceedings of the Topical Meeting held May 7-10, 2001, Venice, Italy. Edited by E. Vernet, R. Ragazzoni, S. Esposito, and N. Hubin. Garching, Germany: European Southern Observatory, 2002 ESO Conference and Workshop Proceedings, Vol. 58, ISBN 3923524617, p. 321*, pages 321–+, 2002.
- [26] A. Tokovinin. From Differential Image Motion to Seeing. *pasp*, 114:1156–1166, October 2002.
- [27] J. Vernin and C. Munoz-Tunon. Measuring astronomical seeing: The DA/IAC DIMM. *pasp*, 107:265–272, March 1995.